12-2019

INTRINSIC STRENGTH, PRECIPITATION HARDENING AND TRIBOLOGICAL BEHAVIOR OF HIGH-ENTROPY ALLOYS

Yangyang Zhao
University of Tennessee, yzhao56@vols.utk.edu

INTRINSIC STRENGTH, PRECIPITATION HARDENING AND TRIBOLOGICAL BEHAVIOR OF HIGH-ENTROPY ALLOYS

A Dissertation Presented for the
Doctor of Philosophy
Degree
The University of Tennessee, Knoxville

Yangyang Zhao
December 2019

Acknowledgments

First of all, I would like to express my deepest gratitude to my advisor Dr. T.G. Nieh for his excellent guidance, caring, and patience at all stages of my Ph.D. program, helping me grow from an inexperienced fresh graduate student to an independent researcher. Dr. Nieh is a great person who has always helped steer my Ph.D. research in the right direction and inspired me to work energetically. Under his supervision, I continue improving my skills in thinking, writing, presentation, and communication along the path toward this Ph.D.

I appreciate Dr. Yanfei Gao, Dr. Hahn Choo, and Dr. Guoxun Chen for their serving on my dissertation committee. Many thanks for their valuable comments and suggestions which have led to significant improvement on the presentation and quality of this dissertation. Thank the staff members in the Department of Materials Science and Engineering, particularly Carla Lawrence, Ashely Cole, Doug Fielden, Frank Holiway, and Randy Stooksbury, for their numerous help. I also thank Dr. John Dunlap in the Joint Institute for Advanced Materials for providing a comprehensive training in both the theory and practice of electron microscopes.

It has been a great experience to pursue my Ph.D. in Dr. Nieh's group. I would like to thank our former group members, Dr. Shuangxi Song, Dr. Chao Zhu, Dr. Dong Wu, Dr. Xiaoyun Li, and Josh Arnold, and our current group member, Youxiong Ye, for their technical interchange and discussions. They are great colleagues to work with, and I have learned a lot from their wealth of experience. I am also thankful to my friends, Rui Feng, Yuan Li, Peijun Hou, Zongyang Lyu, Liubin Xu, Wei Zhang, Chenze Liu, Xue Wang, and Di Xie for their support and friendship, which helped me get through tough times during my Ph.D.

Many thanks to our collaborators who supported my research. I would like to thank Dr. Zhaoping Lu and Dr. Junyang He from the University of Science and Technology Beijing for the

preparation of high-entropy alloy samples. Thank Dr. Houwen Chen from Chongqing University for the high quality TEM characterization. I also thank Dr. Kefu Yao from Tsinghua University for the preparation of amorphous high-entropy alloy samples. Without their help, I cannot complete my research work for the Ph.D. degree.

Financial support for this research from the National Science Foundation under contract DMR-1408722 is gratefully acknowledged. The Tennessee Agricultural Experiment Station and UT College of Engineering that jointly funded the Instrumentation for the nanoindentation work are also appreciated.

Last, but not least, I would like to express my gratitude to my parents for their endless love and unreserved support from when I was born. They were always there cheering me up, and stood by me through the good times and the bad. With their encouragements, I finally reached the destination of my Ph.D. journey.

Abstract

Recently, concentrated multicomponent alloys, or high-entropy alloys (HEAs) consisting of several principal components in approximately equiatomic proportions, have increasingly attracted research interest because of their unusual intrinsic characteristics, such as severe lattice distortion and sluggish diffusion. These features confer HEAs promising mechanical properties, making HEAs potential for structural applications. However, limited knowledge on intrinsic strength, precipitate stability and tribological behavior of HEAs is available.

In Chapters 2 and 3, we systematically analyzed yield strengths of a series of fcc Ni-based and bcc Nb-based equiatomic alloys. By subtracting all possible strengthening contributions, the intrinsic strength (or lattice friction stress) of each alloy was extracted. It was found that lattice friction stress scaled linearly with the lattice distortion in these equiatomic alloys. A simplified model was developed to interpret this result. It was demonstrated that the enhanced strength in HEAs was mainly attributed to the lattice distortion.

In Chapter 4, I reported the study of the coarsening of $L1_2$ precipitates in an fcc $(NiCoFeCr)_{94}Ti_2Al_4$ HEA. Temporal evolutions of the morphology, size, and volume fraction of these coherent precipitates were examined and evaluated using electron microscopes. Treating the fcc-$(NiCoFeCr)_{94}Ti_2Al_4$ alloy as a pseudo ternary Ni-Ti-Al alloy, I analyzed the coarsening kinetics of the precipitates. One of the major findings was that, owing to the relatively slow atomic diffusion in HEAs, coarsening of $L1_2$ precipitates in the current HEA was found to be slower than that in the conventional Ni-based alloys. This result demonstrated good thermal stability of the $L1_2$ precipitates.

In Chapter 5, I investigated the tribological behavior of an amorphous $Zr_{20}Ti_{20}Cu_{20}Ni_{20}Be_{20}$ HEA (a-HEA). Nanoscratch tests were carried out to measure the

coefficient of friction (COF) and wear resistance of the amorphous alloy. The morphology of scratched surface and subsurface was further examined using electron microscopes. Due to high hardness and large elastic recovery, the current a-HEA exhibited good wear resistance and low COF, suggesting that *a*-HEAs are probably good candidate materials for tribological applications.

Finally, a conclusion of all my studies was given. In addition, a future perspective based on my research results were presented in Chapter 6.

Table of Contents

List of Figures

List of Tables

Chapter 1. Introduction

1.1 Intrinsic strength of high-entropy alloys

Since the first report of multi-principal elements alloys (MPEAs) or high-entropy alloys (HEAs) in 2004 [1, 2], significant efforts have been made to develop this new class of solid-solution alloys because of their attractive properties, such as high strength/hardness [3-5], good oxidation/corrosion resistance [6, 7], slow diffusion [8], and excellent thermal stability [9]. These HEAs make use of the vast unexplored compositional space near/in the central region of multicomponent phase diagrams, where a high configurational entropy favors the formation of solid-solution phases, instead of brittle complex intermetallics.

Four ‘core effects’ have been proposed in HEAs [3]: the high entropy effect, the lattice distortion effect, sluggish diffusion, and the ‘cocktail’ effect. In the case of lattice distortion, a HEA consists of a number of constituent elements with different atomic sizes and electronic structures, so that its crystal lattice is expected to be distorted. In fact, several studies using x-ray and neutron have already demonstrated a decrease in diffraction peak intensity and broadening of peak width (Figure 1.1) and were attributed to distorted lattice in HEAs [10, 11]. Lattice distortion in HEAs was also observed using high-resolution TEM (transmission electron microscope) shown in Figure 1.2. However, it is difficult to physically visualize and quantitatively define lattice distortion at the atomic level. Some efforts have been made [12, 13] to evaluate the distortion, but with only limited success. The usual approach is to statistically calculate the atomic size difference, but a clear physical picture how the lattice is distorted is still lacking [13]. Despite of the fact that lattice distortion is quantitatively ill defined, it is generally recognized [10] that lattice distortion is responsible for the observed unusual physical and

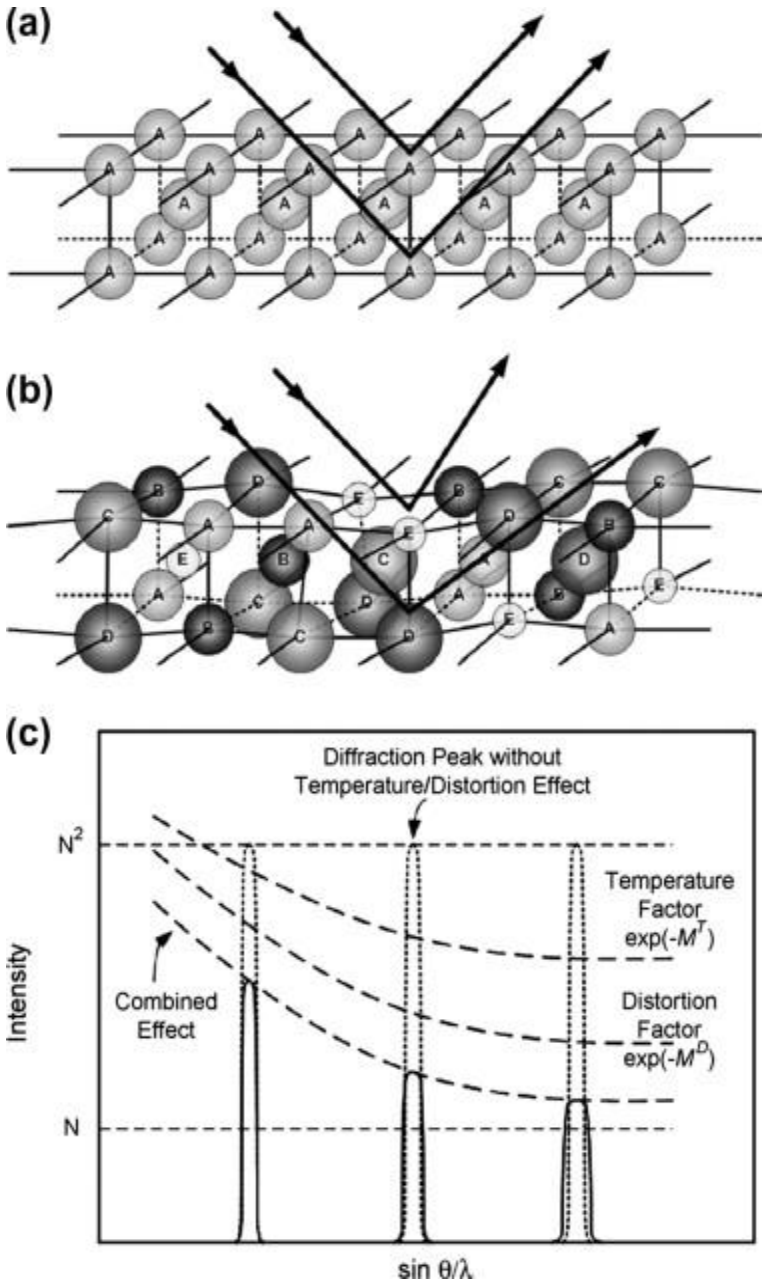

Figure 1.1 Schematic illustration of lattice distortion effects on Bragg diffraction [10]: (a) perfect lattice with the same atoms; (b) distorted lattice consisting of different-sized atoms; (c) temperature and distortion effects on the XRD intensity.

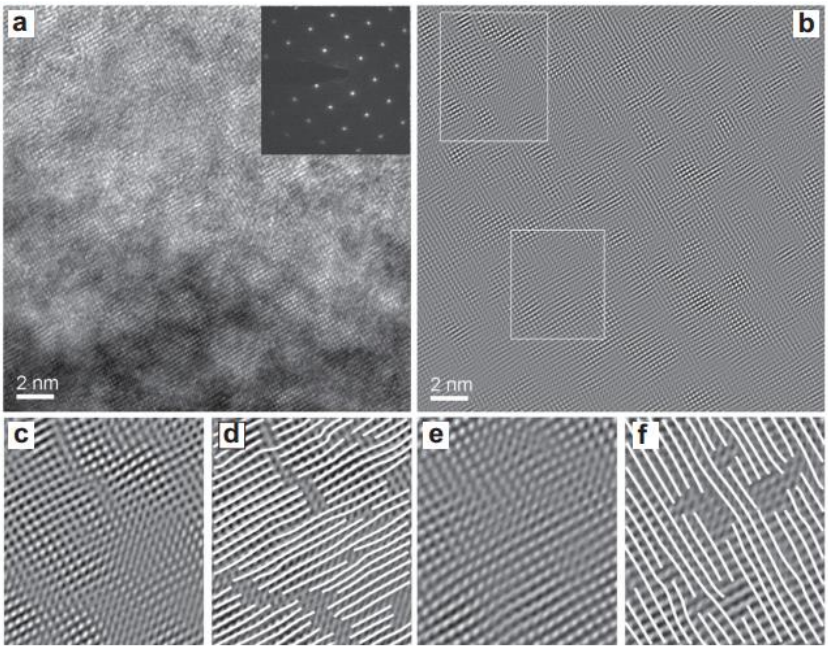

Figure 1.2 (a) High-resolution TEM and (b-f) inverse fast Fourier transform images of Nb-Mo-Ta-W HEA homogenized at 1800 °C for 7 days [13].

mechanical properties of HEAs, such as strength enhancement.

For example, yield strength of the fully annealed pure Ni is only about 59 MPa [14], which is much lower than that of the homogenized [15, 16] or fully recrystallized [17, 18], single-phase fcc (face-centered cubic) NiCoCrFeMn (~ 200 MPa), as shown in Figure 1.3. The large strength difference triggered several research studies. These efforts primarily extended Fleischer's [19] solid-solution strengthening model for dilute alloys to concentrated alloys [20-22] with the attempt to reconcile the observed strength enhancement. However, an inevitable difficulty was encountered during the modeling because the impossibility to separate the solute from solvent atoms in equiatomic concentrated alloys. Consequently, the applicability of the traditional solid-solution strengthening theory to these alloys becomes highly skeptical.

An alternative picture for the strengthening in HEAs is to imagine dislocations moving in a solution matrix that is uniformly (or globally) distorted by completely intermixed constituent

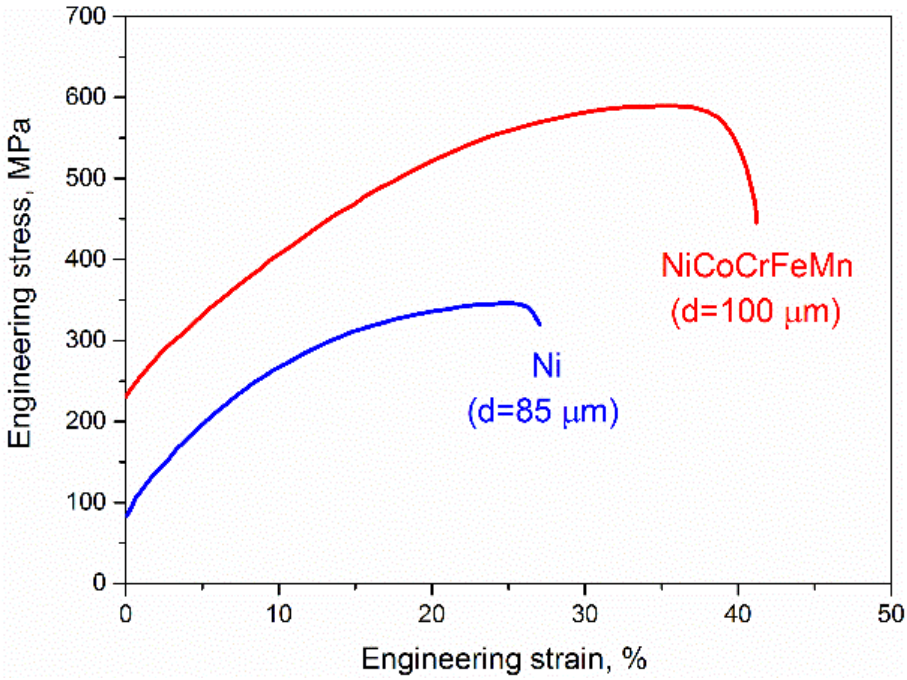

Figure 1.3 Engineering stress versus engineering plastic strain obtained in tension for fully recrystallized NiCoCrFeMn and pure Ni (*d* = grain size) [23, 24].

atoms. In other words, one can envision the enhanced strength is simply a result of increased "intrinsic" or "friction" stress in the distorted lattice. In fact, Wu *et al.* [23] estimated the friction stress by calculating the Peierls stress, and concluded that the dislocation core should extend to about (1.0-1.5)*b*, where *b* is the Burgers vector. It is also worthy of mentioning that several years ago, Yeh *et al.* [10] reported that the hardness as well as the lattice strain (or distortion) of equiatomic Ni-Al-Co-Cr-Cu-Fe-Si alloy systems was enhanced with increasing number of constituent elements, as shown in Figure 1.4. However, hardness value represents the overall strength of a polycrystal, which actually consists of several possible strengthening mechanisms, in addition to the lattice friction stress.

Overall, HEAs always exhibit a higher strength than their conventional (dilute) alloys counterparts due to the engineered configuration disorder. Explanations are, so far, based on the traditional solid-solution theory or a modified version. Physically, it does not make much sense,

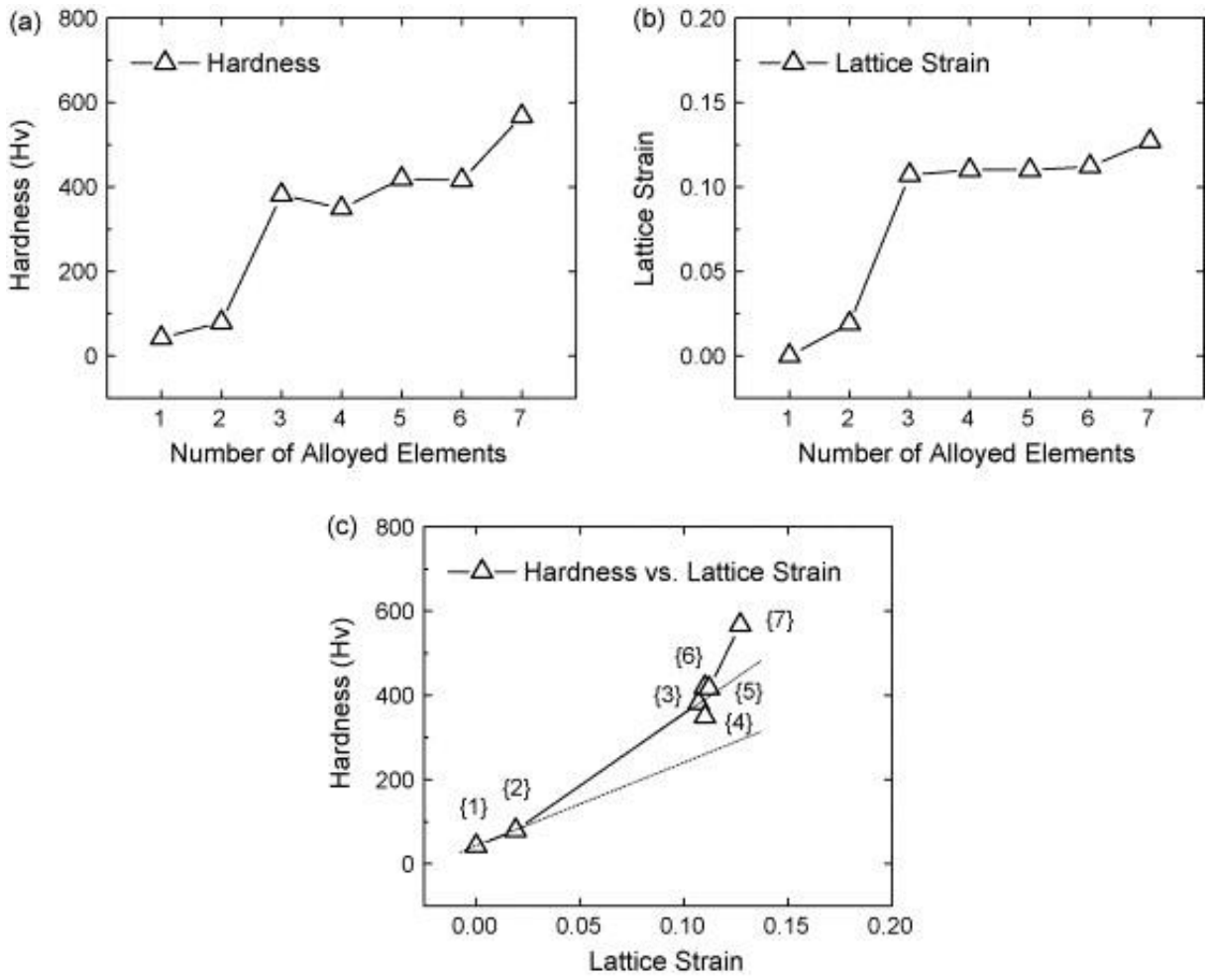

Figure 1.4 (a) Experimentally measured hardness and (b) theoretically predicted overall lattice strain of Cu-Ni-Al-Co-Cr-Fe-Si HEA series with increasing number of constituent elements; (c) correlation of hardness versus overall lattice strain of the alloy series (the quoted number {n} denotes the number of incorporated elements) [10].

since solute and solvent atoms are not differentiable in equimolar alloys. Several groups are currently working on the lattice distortion in HEAs using XRD or neutron diffraction, trying to get a quantitative assessment of the distortion [21, 22]. However, the intrinsically higher strength in HEAs and its quantitative correlation with lattice distortion still remain a puzzle. Systematic attempts to quantify the lattice distortion effect and to separate it from other strengthening contributions are still missing [25, 26].

1.2 Precipitate coarsening in high-entropy alloys

Yeh *et al* [8] pointed out that one of the key features of HEAs is the sluggish diffusion. Figure 1.5 shows the self-diffusivities of the constituent elements in a CoCrFeMnNi alloy and, for comparison, the corresponding values for the same element in various conventional alloy systems are also included. It is readily observed that self-diffusivities of the constituent elements in the CoCrFeMnNi HEA are slower than those for the same element in various conventional alloy systems, as shown in Figure 1.5. The slower diffusion is an important contributor to the outstanding properties of HEAs, especially at elevated temperatures, as it leads to good high-temperature structural stability [27] and excellent high-temperature strength [28]. Consequently, in applications requiring slow diffusion kinetics, the sluggish diffusion effect makes HEAs very competitive.

Based on the above-mentioned reasons, precipitation hardening has recently been successfully applied to strengthen HEAs [29-32]. For example, He *et al*. [29] reported nano-sized $L1_2$ coherent precipitates (Figures 1.6a-c) in an fcc NiCoFeCr alloy with minor additions of Al and Ti, specifically $(NiCoFeCr)_{94}Ti_2Al_4$. Wang *et al*. [30] also observed the presence of cuboidal B2 coherent precipitates (Figure 1.6d) in a body-centered-cubic (bcc) $Al_{0.7}CoCrFe_2Ni$ alloy. For

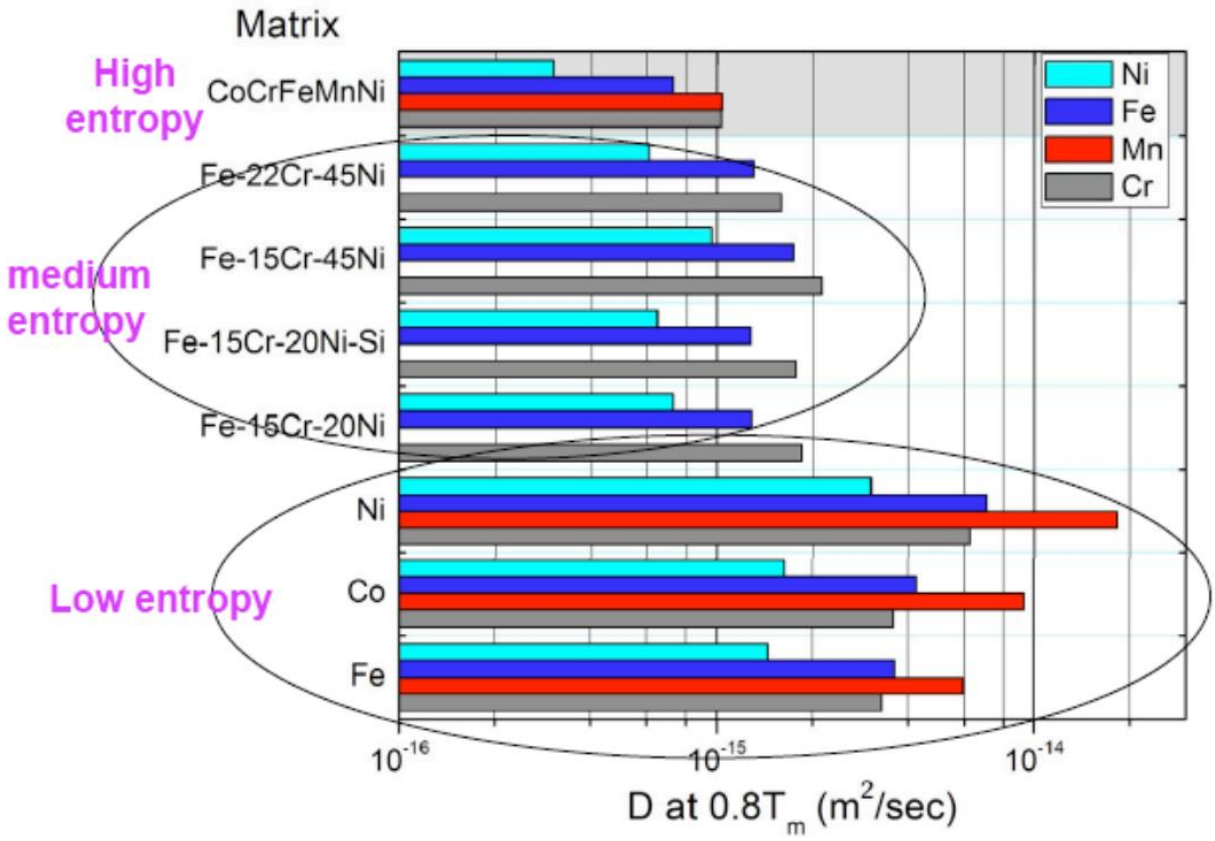

Figure 1.5 Comparison of self-diffusivities of several major constituent elements in high-entropy alloys and conventional alloys [8].

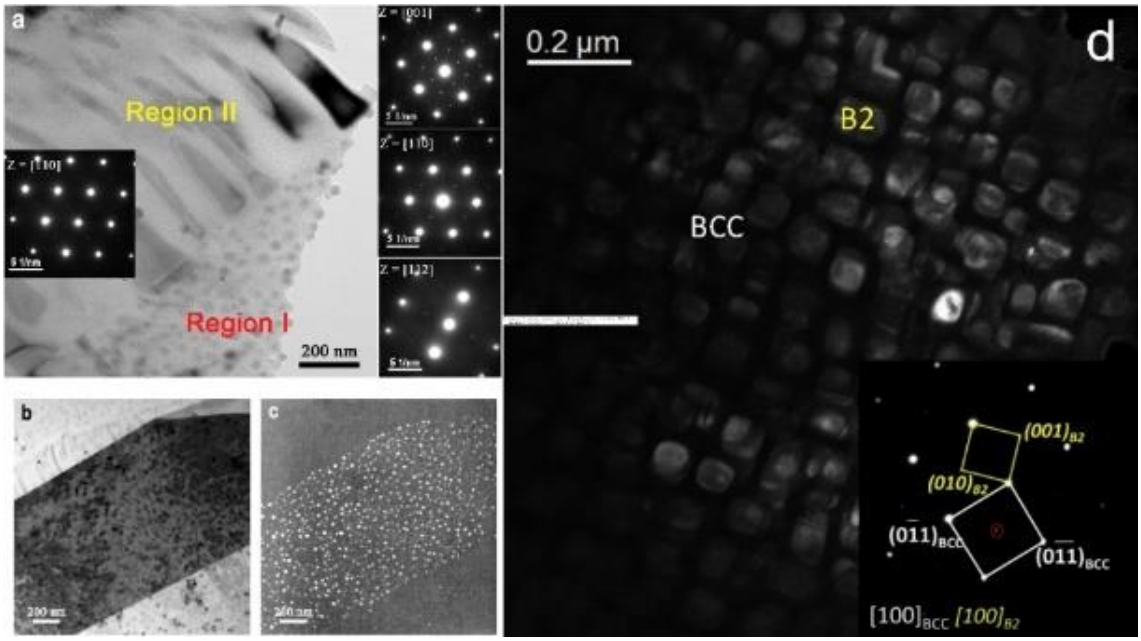

Figure 1.6 TEM images of $L1_2$ coherent precipitates (a-c) in the $(NiCoFeCr)_{94}Ti_2Al_4$ alloy [29] and B2 coherent particles (d) in the $Al_{0.7}CoCrFe_2Ni$ alloy [30].

precipitation-hardening, strengthening effect strongly depends on the thermal stability of the coherent precipitates, especially at elevated temperatures. For instance, in the Ni-based superalloys, the coarsening of coherent $L1_2$-Ni_3(Al, Ti) particles predominantly determines the temperature range for the service of the alloys [33]. Consequently, extensive efforts were made to the study of particle coarsening behavior in precipitation-hardened alloys in the past [34-38].

In the study of precipitation-hardened HEAs, the majority of published works focused on mechanical properties and the morphology of precipitates in the alloys. For example, thermomechanically treated $(NiCoFeCr)_{94}Ti_2Al_4$ alloy produced a microstructure with uniform dispersion of fine coherent precipitates and resulted in a yield strength of over 1 GPa with good tensile elongation of 17% [29], as shown in Figure 1.7. These $L1_2$ coherent precipitates dominated in the temperature range of 650-850 °C, but became overwhelmed by $L2_1$ Heusler phase (Ni_2TiAl) at temperatures above 850 °C [39]. Therefore, it is necessary to understand the

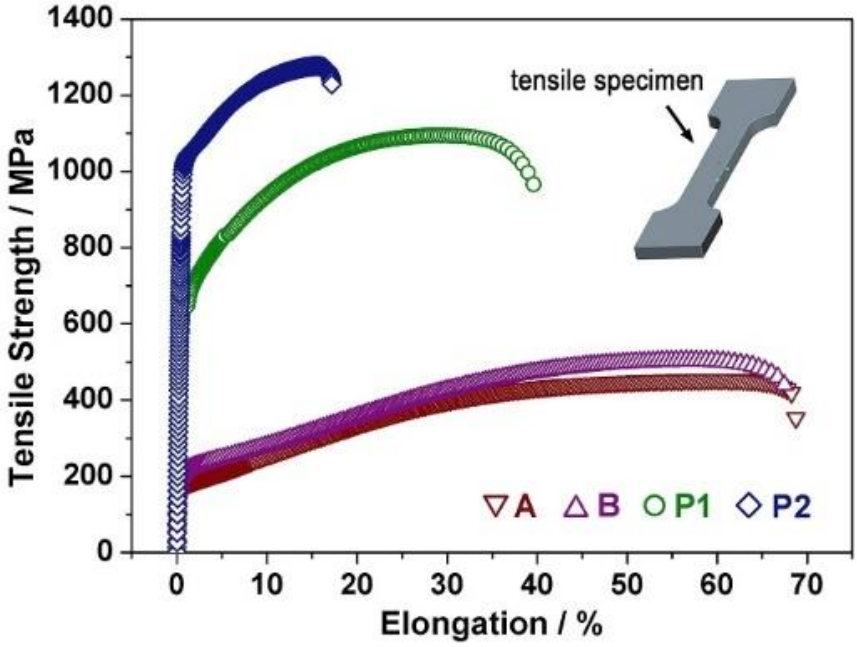

Figure 1.7 Room-temperature tensile properties of as-homogenized NiCoFeCr (A), as-homogenized $(NiCoFeCr)_{94}Ti_2Al_4$ (B), and as-aged $(NiCoFeCr)_{94}Ti_2Al_4$ (P1: aged at 800 °C for 18 h; P2: aged at 650 °C for 4 h) [29].

thermal stability and coarsening of these coherent precipitates in order to keep them stable and useful at elevated temperatures [40].

The coarsening of precipitates in dilute alloy systems has been proposed by the Lifshitz-Slyozov-Wagner (LSW) theory [41, 42], which predicts $d \propto t^{1/3}$, where d is the average precipitate size and t is the annealing time. The LSW theory has been successfully applied to describe the coarsening behavior of coherent precipitates in binary Ni-Al [34], Al-Sc [37], and Al-Li [38] alloys. In the case of concentrated multicomponent alloys, however, the interplay and diffusion of individual constituent elements are unclear. Moreover, long-range diffusion is expected to be sluggish because of the necessity for cooperative diffusion of constituent atoms to keep a proper compositional partitioning. From a scientific point of view, it is also of great interest to study the coarsening kinetics of coherent precipitates in concentrated multicomponent alloys [40].

1.3 Precipitation strengthening mechanism

The effectiveness of precipitation strengthening depends on the nature of interactions between dislocation and precipitate. According to conventional theory, precipitation strengthening, in principle, is governed by either precipitate shearing or Orowan dislocation bypass mechanism. Shearing occurs when precipitates are relatively small and coherent, while Orowan bypass of dislocations dominates when precipitates are sufficiently large.

Strengthening by ordered coherent precipitates occurs when a matrix dislocation shears an ordered particle and creates an antiphase boundary on the slip plane of the precipitate phase [43]. This strengthening effect is shown schematically in Figure 1.8. The model is based on the fact that dislocations pair up to cut through precipitates, where the trailing dislocation glides in the same plane to remove the antiphase boundary formed by the leading dislocation. For small particles, dislocation pairs cutting through precipitates are usually weakly coupled (Figure 1.8a), and the shear stress increment required for dislocation movement is given by [44]

$$\Delta\tau_{weak} = \left(\frac{\gamma_{APB}}{2b}\right)\left[\left(\frac{2\gamma_{APB}d\phi}{\pi\Gamma}\right)^{1/2} - \phi\right] \tag{1.1}$$

where γ_{APB} is the anti-phase boundary energy of the precipitates, b is the Burgers vector, d is the average precipitate size, ϕ is the precipitate volume fraction, and Γ is the dislocation line tension which can be estimated by $\Gamma = Gb^2/2$ [44]. For large particles, on the other hand, shearing of precipitates occurs by strongly coupled dislocation pairs (Figure 1.8b), and the cutting stress or shear stress increment is [45]

$$\Delta\tau_{strong} = \frac{1}{2}\left(\frac{Gb}{d}\right)\phi^{1/2}0.72w\left(\frac{\pi d\gamma_{APB}}{wGb^2} - 1\right)^{1/2} \tag{1.2}$$

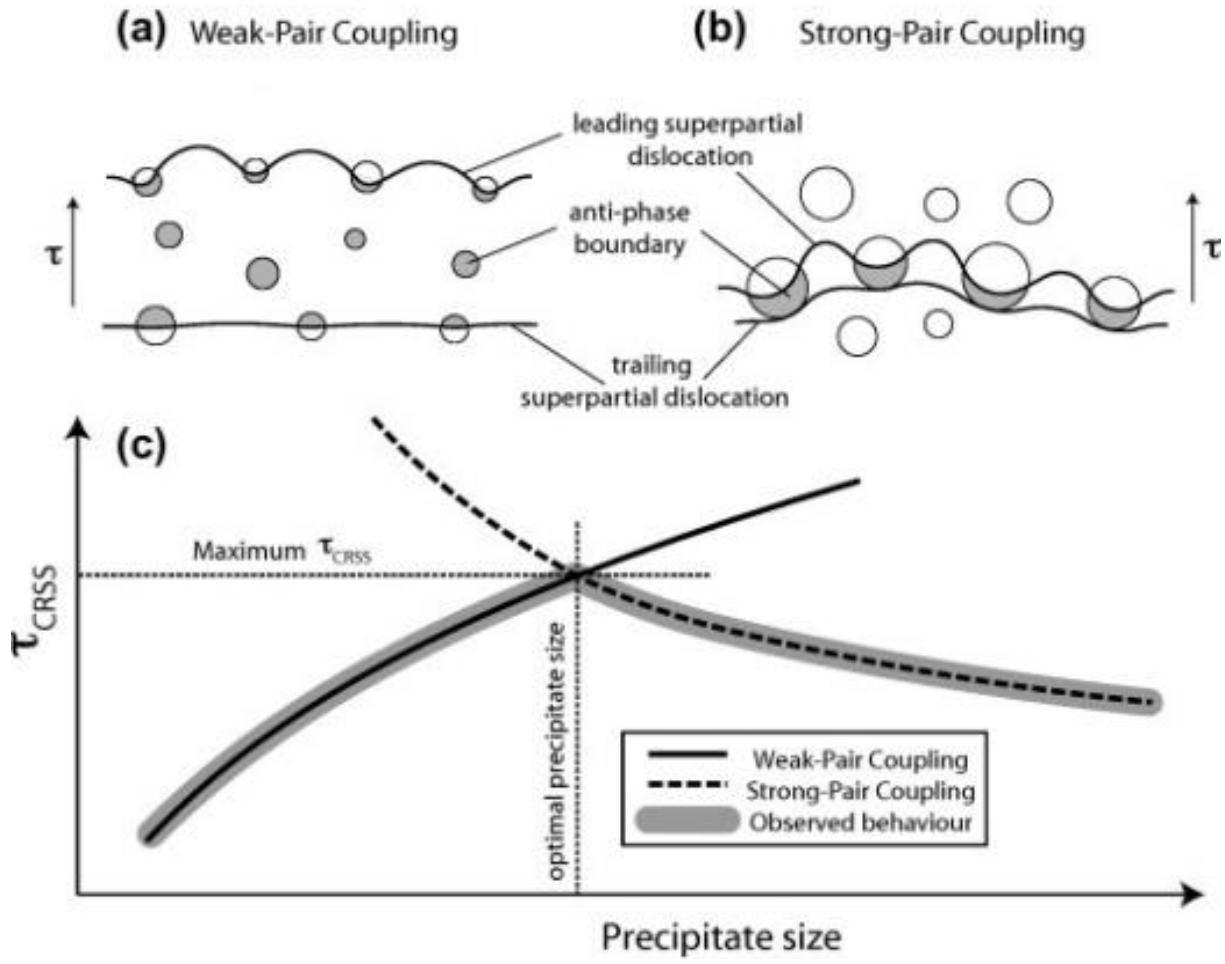

Figure 1.8 (a) Weakly and (b) strongly coupled dislocation pairs cutting ordered precipitates; (c) the corresponding critical resolved shear stress relationship with respect to precipitate size [46].

where G is the shear modulus of the matrix, and w is a constant describing the elastic repulsion between the strongly coupled dislocation pairs, which is approximately equal to 1. The increase in shear stress due to precipitation as a function of the average precipitate size is then plotted in Figure 1.8c. It is noted that the shear stress initially increases, as described by the weak-coupling mechanism ($\Delta\tau_{weak} \propto d^{1/2}$ in Eq. 1.1), reaches a peak and, then, decreases with growing precipitate size according to the strong-coupling mechanism ($\Delta\tau_{strong} \propto d^{-1/2}$ in Eq. 1.2). Optimal strengthening takes place at the crossover of the two mechanisms, which is determined by the morphology as well as the nature of precipitates. Increasing the precipitate size further, the stress required for the dislocations to bypass the precipitates is lower than the stress required for the dislocations to cut the particles, and the Orowan bypassing mechanism operates. For Orowan bypass mechanism, the increase in the critical resolved shear stress can be expressed as [44]:

$$\Delta\tau = \frac{0.4Gb}{\pi\sqrt{1-\nu}} \frac{\ln(\bar{d}/b)}{\lambda} \tag{1.3}$$

where ν is the Poisson's ratio [1], $\bar{d} = \sqrt{2/3} \cdot d$ is the average precipitate diameter on the slip planes, and $\lambda = \bar{d}(\sqrt{(\pi/4\phi)} - 1)$ is the average edge-to-edge interparticle spacing.

Although precipitation hardening has been successfully introduced into HEAs, as mentioned before, the strengthening mechanism are yet to be explored and modelled. Therefore, it is necessary and of great interest to model and experimentally validate precipitation hardening in HEAs [40].

1.4 Tribological behavior of high-entropy alloys

The concept and strategy of designing HEAs has also been extended to nanocrystalline [47-49] and even amorphous alloys (denoted as *a*-HEAs herein) [50-56]. In the study of *a*-HEAs,

the majority of published works focused on the aspects of thermodynamics, kinetics and simple mechanical properties (such as tension and compression). For example, Yang *et al.* [57] demonstrated that amorphous $Zr_{20}Ti_{20}Cu_{20}Ni_{20}Be_{20}$ exhibited higher thermal stability and slower crystallization kinetics as compared to its conventional amorphous alloy counterparts containing the same constituent elements (e.g., $Zr_{41.2}Ti_{13.8}Cu_{12.5}Ni_{10}Be_{22.5}$ commercially known as Vit 1). Additionally, some *a*-HEAs were shown to have exceptionally high strength and hardness [52, 58], making them possible candidates for wear applications. However, a systematic evaluation of friction and wear properties of *a*-HEAs is yet to be conducted [59].

Nanoscratching is a viable technique for the study of the tribological behavior of materials. This technique enables precise measurements of load and displacement, thus a quantitative evaluation of mechanical and tribological performance at the micro/nano-scale. Unlike a macroscopic wear test (such as a pin-on-disc test) in which two macroscopic surfaces each consists of large number of small surface asperities are making contact (i.e., multi-asperities contact), a nanoscratch test can be treated as a single-asperity contact between the fine tip (with tip radius ~ tens to hundreds of nanometers) and sample. Although a single-asperity contact may be insufficient to describe the general macroscopic wear, it explores the interaction and response between two contacting materials. In addition, it provides the insight and progression of contact allowing the study of underlying mechanisms, and helps to bridge the gap between single-asperity contact and macroscopic tribology.

Previous nanoscratch studies [60, 61] indicated that, resulting from a high hardness, amorphous alloys usually showed good wear resistance but brittle fracture morphology. Recently, Ye *et al.* [62] investigated friction and wear behavior of a bcc (body-centered cubic) NbTiZrHf HEA by applying nanoscratch technique (as shown in Figure 1.9) and found that the alloy

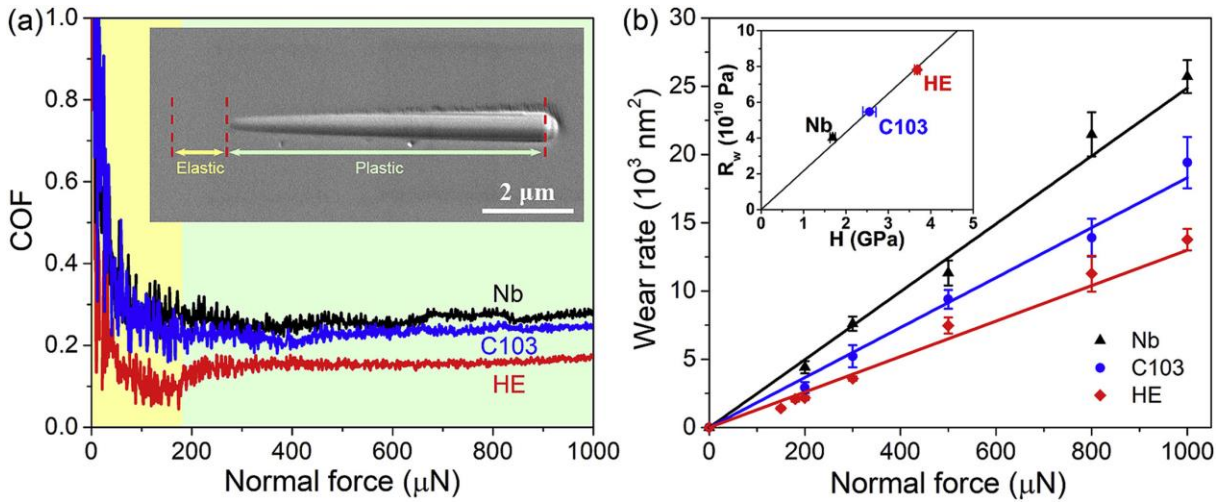

Figure 1.9 (a) COF and (b) wear rate as a function of normal force for Nb, C103 and bcc NbTiZrHf high-entropy alloy (denoted as HE in the figure). The inset in (a) illustrates a SEM image of scratched morphology under ramping load mode. The inset in (b) shows wear resistance vs. hardness for pure Nb, C103 and NbTiZrHf HEA.

exhibited ductile plowing and improved wear resistance over its traditional alloy counterparts. Since amorphous alloys are generally harder than their crystalline alloy counterparts, amorphous HEAs are also expected to have a better wear performance than crystalline HEAs. From a scientific point of view, it will be also intriguing to study the wear mechanism of these *a*-HEAs using the nanoscratch technique, since *a*-HEAs have a brittle/ductile material combination, in particular, on plasticity.

In summary, from the literature results, it is readily concluded that: (1) intrinsically higher strength in HEAs may stem from severe lattice distortion, and the lattice distortion is possibly correlated with lattice friction stress of the alloys; (2) coarsening of coherent particles in precipitation-hardened HEAs is expected to be slower than that in conventional alloys due to the sluggish diffusion in HEAs; (3) these particles are expected to produce significant strengthening in HEAs at both room temperature and elevated temperatures, as they are effective barriers for dislocation motion; (4) high strength/hardness makes HEAs potential for tribological

applications.

1.5 Research objectives and tasks

In order to fill the knowledge gaps on intrinsic strength, precipitation hardening and tribological behavior of HEAs, the following objectives and tasks are specified:

1. Explore an approach to quantitatively describe the lattice distortions in fcc-HEAs, establish relationships between lattice distortion and intrinsic strength of the alloys. Compare the lattice distortion effect in bcc Nb-based and fcc Ni-based equiatomic alloys

2. Explore an approach to quantitatively describe the lattice distortions in bcc-HEAs, establish relationships between lattice distortion and intrinsic strength of the alloys. Compare the lattice distortion effect in bcc and fcc HEAs.

3. Investigate coarsening of coherent particles and microstructural evolution in precipitation-hardened HEAs (specifically an fcc $(NiCoFeCr)_{94}Ti_2Al_4$ alloy); this includes examining the nature and morphology of precipitates, evaluating the activation energy and growth rate for precipitate coarsening.

4. Evaluate and model precipitation strengthening effect in HEAs (i.e. the $(NiCoFeCr)_{94}Ti_2Al_4$ alloy. Estimate the optimal precipitate size to confer the alloy best mechanical properties.

5. Study tribological behavior of an amorphous high-entropy alloy (a-HEA) using a nanoscratch method. Evaluate the coefficient of friction and wear resistance of the a-HEA and compare with those of other conventional amorphous alloys and high-entropy alloys.

Chapter 2. Correlation between lattice distortion and friction stress in Ni-based equiatomic alloys

In this chapter, we evaluate the intrinsic strength of pure Ni and a series of Ni-based fcc equiatomic binary, ternary, quaternary, and quinary solid-solution alloys from available data in literature. Meanwhile, lattice distortion in these equiatomic alloys are quantified using the lattice mismatch strain defined as the change of lattice parameter with respect to that of pure Ni. We will present a semi-quantitative correlation to link the lattice friction stress with the lattice distortion and shed lights on the cause for the apparent high strength in equiatomic alloys.

2.1 Lattice distortion-yield strength correlation

Now, let us begin with the Cantor alloy, the equiatomic NiCoCrFeMn. This alloy has a single-phase fcc structure. Since Ni is the only constituent element in this alloy that has an fcc-structure, the Cantor alloy can be regarded as a Ni-based alloy, especially considering the lattice constant of NiCoCrFeMn ($a = 0.3590$ nm [1]) is very close to that of Ni ($a = 0.3517$ nm [14]). Lattice distortion existing in the Cantor alloy can be envisioned in the following way. Pure fcc-Ni is considered to be the baseline reference state with every lattice site being occupied by the Ni atoms in the unit cell. Subsequently, Ni sites are gradually replaced by other constituent atoms according to the alloy stoichiometry and eventually the pure Ni evolves into the HEA. Upon atomic substitution, the bond length alters due to the atomic size mismatch and the difference in chemical specificity (e.g., electronegativity and charge transfer) between Ni and the substituted atom [63]. During the substitution procedure, the initial fcc structure always remains and no

second phase is formed. In this fashion, each substitution is anticipated to distort the fcc lattice and, after completion, the final lattice would be either dilated or contracted depending on the combined (average) effect of all substituted atoms. While the effect of chemical specificity is difficult to evaluate, let us assume it is minor in comparison to the atomic size effect. This is a reasonable assumption since, for the Cantor alloy NiCoCrFeMn, the five constituent elements are immediately adjacent to each other in the Periodic Table.

The lattice distortion, to the first approximation, can be quantified using the volumetric distortion, Δ, which is defined as $\Delta = (\Omega_{HEA} - \Omega_{Ni})/\Omega_{Ni}$, where Ω_{HEA} and Ω_{Ni} are the volume of unit cell of the HEA and Ni, respectively. The linear distortion, i.e., the lattice mismatch strain, δ, is defined as $\delta = (a_{HEA} - a_{Ni})/a_{Ni} \approx \Delta/3$ [33], where a_{HEA} and a_{Ni} are the lattice constant of the HEA and Ni, respectively. For simple discussion, we will use the lattice mismatch strain δ to describe the lattice distortion herein. Lattice constants and the δ values for pure Ni and a series of Ni-based fcc-equiatomic alloys, including those of two-components extending up to five-components, are listed in Table 2.1.

A graph directly comparing lattice distortion of these Ni-based equiatomic alloys is displayed in Figure 2.1. For convenience, the x-axis is plotted in the order of increasing number of elements in alloys. It appears that more constituent elements can distort the lattice more. As mentioned before, Yeh *et al.* [10] also reported that lattice strain (or distortion) increased with the number of constituent elements. However, according to Figure 2.1, it is not necessarily true *per se*. For instance, the Cantor alloy NiCoCrFeMn has the highest number of constituent elements in the equiatomic alloy series, but it is the 3-component NiFeMn that has the largest lattice distortion. In theory, adding another alloying element can cause either lattice expansion or contraction, depending on its relative atomic size and chemical bond with respect to its neighbors.

Table 2.1 Lattice constant (a), lattice distortion (δ), shear modulus (G), grain size (d), Poisson's ratio (ν), 0.2% offset yield strength (σ_y), the lattice friction stress (σ_f), corresponding σ_f/G, and the normalized dislocation core width (w/b) of the equiatomic alloys investigated in this study.

Alloys	a (Å)	δ	G (GPa)	d (μm)	ν	σ_y (MPa)	σ_f (MPa)	σ_f/G (10^{-3})	w/b	Ref.
Ni	3.517	0	76	–	0.31	59	10	0.1	1.77	[14]
NiCo[a]	3.535	0.0051	84	35	0.29	110	59	0.7	1.50	[23, 64]
NiFe[a]	3.583	0.0188	62	35	0.34	187	139	2.2	1.33	[23, 64]
NiCoMn[a]	3.598	0.0230	77	32	0.23	230	178	2.3	1.30	[23, 64]
NiFeMn[a]	3.616	0.0281	73	30	0.24	229	176	2.4	1.29	[23, 64]
NiCoCr[a]	3.559	0.0119	–	–	–	–	–	–	–	[23, 64]
NiCoFe[a]	3.569	0.0148	60	28	0.35	213	161	2.7	1.30	[23, 64]
NiCoFe[b]	3.580	0.0179	–	–	–	–	–	–	–	[65]
NiCoFe[b]	3.577	0.0171	–	–	–	–	–	–	–	[66]
NiCoCrMn[a]	3.589	0.0205	–	–	–	–	–	–	–	[23, 64]
NiCoFeMn[a]	3.592	0.0213	77	48	0.22	176	131	1.7	1.34	[23, 64]
NiCoFeCr[a]	3.572	0.0156	–	–	–	–	–	–	–	[23, 64]
NiCoFeCr[b]	3.577	0.0171	–	–	–	140	–	–	–	[67]
NiCoFeCr[c]	3.568	0.0145	84[17]	200	0.28[17]	130	101	1.2	1.41	[67]
NiCoFeCr[b]	3.581	0.0182	–	–	–	147	–	–	–	[68]
NiCoFeCr[c]	3.578	0.0173	84[17]	290	0.28[17]	165	139	1.7	1.36	[29]
NiCoCrFeMn[a]	3.599	0.0233	80	35	0.26	215	164	2.1	1.32	[23, 64]
NiCoCrFeMn[b]	3.602	0.0242	–	–	–	215	–	–	–	[67]
NiCoCrFeMn[c]	3.595	0.0222	80[17]	130	0.26[17]	162	130	1.6	1.36	[67]
NiCoCrFeMn[b]	3.594	0.0219	–	–	–	209	–	–	–	[15]
$(NiCoCrFeMn)_{98}Al_2$[b]	3.615	0.0279	–	–	–	–	–	–	–	[15]
$(NiCoCrFeMn)_{96}Al_4$[b]	3.619	0.0290	–	–	–	220	–	–	–	[15]
$(NiCoCrFeMn)_{93}Al_7$[b]	3.631	0.0324	–	–	–	242	–	–	–	[15]

[a] Samples prepared by arc melting, drop casting, homogenization, cold rolling and annealing.

[b] Samples prepared by arc melting and, then, drop casting.

[c] Samples prepared by arc melting, drop casting, and homogenization.

0.2% offset yield strength (σ_y) was determined at a strain rate of 1×10^{-3} s^{-1} at room temperature.

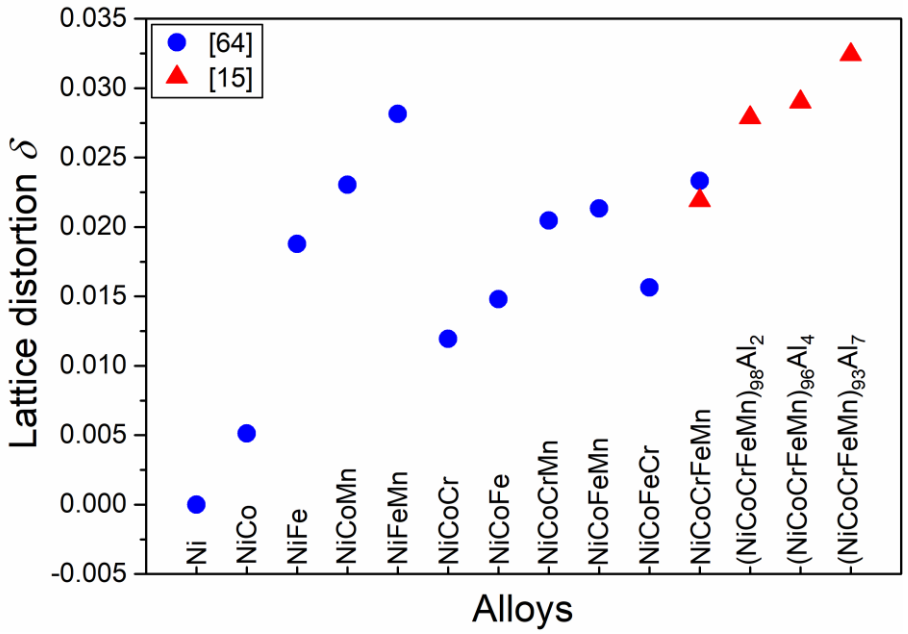

Figure 2.1 Comparison of lattice distortion (δ) in the Ni-based fcc equiatomic alloys listed in Table 2.1.

It is pointed out that, among the five constituent elements of the Cantor alloy (NiCoCrFeMn), nickel atom is the smallest (r_{Ni} ~0.124 nm, r_{Co} ~0.125 nm, r_{Fe} ~0.126 nm, r_{Cr} ~0.128 nm and r_{Mn} ~0.127 nm [69]). It is therefore a natural expectation that a higher-component alloy in this Ni-based HEA series would have a larger lattice constant. In fact, this concept extends even to higher alloying addition, for example, the largest distortion is found in the $(NiCoCrFeMn)_{100-x}Al_x$ ($x = 0 - 7$) alloy system [15]. It is apparently caused by the substitution of larger Al atom (r_{Al} ~0.143 nm [69]).

Also included in Table 2.1 is the yield strength of the Ni-based equiatomic alloy series (from 2 to 5-components) in their fully annealed (or homogenized) states. Let us define strength enhancement ($\Delta\sigma_y$) as the increase in yield strength with respective to pure nickel, that is, $\Delta\sigma_y = \sigma_{y,HEA} - \sigma_{y,Ni}$, where $\sigma_{y,HEA}$ and $\sigma_{y,Ni}$ are the yield strength of the HEA and pure Ni, respectively. The correlation between $\Delta\sigma_y$ and δ is shown in Figure 2.2. The graph clearly

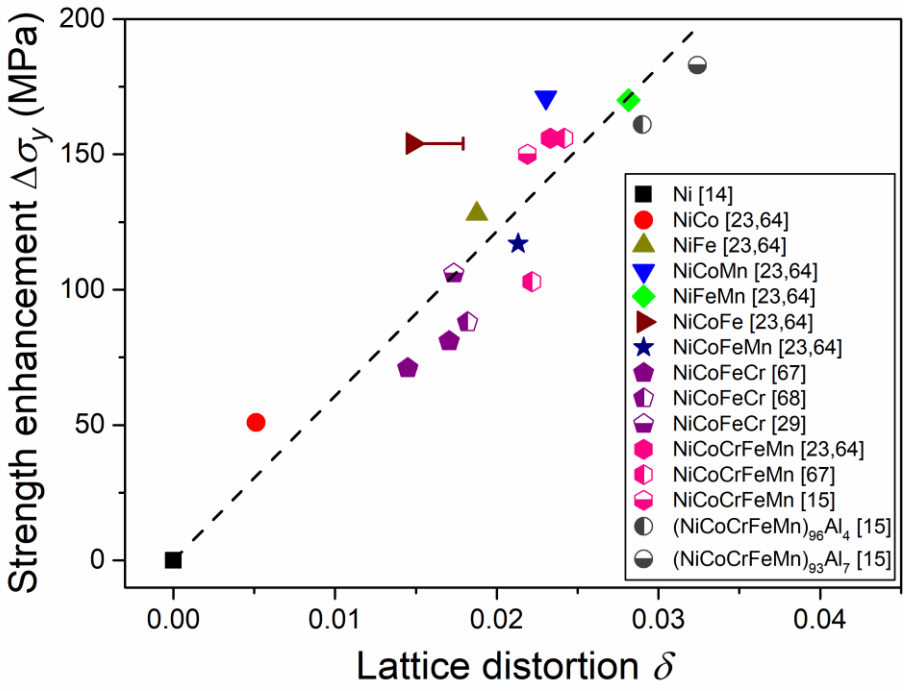

Figure 2.2 Correlation between the strength enhancement ($\Delta\sigma_y$) and lattice distortion (δ). The error bar of lattice distortion for NiCoFe is from Refs. [64-66].

exhibits a general trend, namely, $\Delta\sigma_y$ monotonically increases with increasing δ in these Ni-based equiatomic alloys. The result appears to be similar to that reported in the equiatomic Ni-Al-Co-Cr-Cu-Fe-Si alloy system by Yeh *et al.* [10], but it needs to point out that Yeh's alloys are actually multi-phase (fcc+bcc, body-centered cubic) and, since the bcc phase is generally harder than fcc phase [70] and the amount of bcc phase increases with the number of constituent elements, their results can also be rationalized by the conventional composite theory.

2.2 Lattice distortion-friction stress correlation

Plastic yielding is caused by dislocation motion in crystals. When dislocations move through a crystal lattice under stresses, they interact with various crystalline defects. In dilute solid-solution alloys, moving dislocations interact with surrounding point defects (solute atoms);

this has been well described before [19]. In a HEA, on the other hand, even in the absence of crystalline defects, as long as all constituent atoms are equally partitioned, the interaction between a moving dislocation and distorted lattice is expected to be uniform throughout the entire lattice. In other words, the moving dislocation would experience a constant resistance (friction) and travel in a viscous manner through the distorted lattice. This is in an analogy to the lattice friction stress in a conventional alloy. To estimate this frictional stress, let us first evaluate the yield strength. The yield strength of a crystal σ_y can be expressed as:

$$\sigma_y = \sigma_f + \Delta\sigma_s \tag{2.1}$$

where σ_f is the lattice friction stress of the crystal and $\Delta\sigma_s$ includes contributions from all possible strengthening mechanisms, such as solid-solution hardening, dislocation hardening (or strain hardening), grain-boundary hardening, and precipitation hardening.

In the current work, precipitate is practically absent in the pure Ni or fully annealed Ni-based equiatomic alloys. Based on X-ray diffraction and scanning electron microscope analyses [23, 71], these alloys are all single-phase fcc-alloys. Otto *et al.* [18] also confirmed that fully annealed equiatomic NiCoCrFeMn alloy is truly fcc single-phase without any precipitate. It is therefore reasonable to neglect precipitation hardening.

In terms of dislocation hardening (or Taylor hardening), the strength increase $\Delta\sigma_d$ can be estimated via equation [72]:

$$\Delta\sigma_d = M\alpha Gb\rho^{1/2} \tag{2.2}$$

where $M = 3.06$ is the Taylor factor for polycrystalline fcc-metals, $\alpha = 0.2$ is an empirical constant [73], G is the shear modulus, b is the Burgers vector, and ρ is the dislocation density. Since ρ in the fully annealed pure Ni is on the order of 10^{12} m^{-2} [74, 75], it is conceivable that

ρ in the fully annealed equiatomic alloys is also about 10^{12} m^{-2}. Insert appropriate variables into Eq. 2.2, the strength increment $\Delta\sigma_d$ is estimated to be only about 12 MPa, which is relatively small compared to the yield strength of any of the equiatomic alloys listed in Table 2.1. Therefore, a possible contribution from dislocation hardening can be ignored.

Another possible contribution is from grain-boundary hardening, $\Delta\sigma_{gb}$, which can be evaluated using the classical Hall-Petch relationship:

$$\Delta\sigma_{gb} = k_{HP} d^{-1/2} \tag{2.3}$$

where d is the average grain size, and k_{HP} is the Hall-Petch coefficient, which is $226\ \text{MPa}\cdot\mu\text{m}^{1/2}$ for the fully annealed fcc-NiCoCrFeMn [76], slightly higher than the upper bound value for conventional fcc-alloys [70]. The value of k_{HP} is not available for the majority of the multicomponent alloys listed in Table 2.1. However, it seems reasonable to apply $k_{HP} = 226\ \text{MPa}\cdot\mu\text{m}^{1/2}$ for the Ni-based equiatomic alloys in this study. Apply this k_{HP} value, the strengthening from a grain size of 35 μm is estimated to be about 38 MPa, which is not considered negligible but is still relatively small compared to the yield strength (>>100 MPa) of the listed Ni-based equiatomic alloys.

Traditional solid-solution strengthening theory describes the elastic interaction between solute atoms and moving dislocations as they move through the solvent lattice. As pointed out before, there is essentially no excess solute atom in an equiatomic "solid-solution" alloy, as long as the constituent atoms are completely intermixed. Therefore, there is, in principle, no contribution of solid-solution strengthening in any of the equiatomic alloys listed in Table 2.1, unless the alloy indeed contains dilute alloying addition. For instance, He *et al.* [15] studied single-phase fcc-NiCoCrFeMn alloyed with minor amounts of Al, specifically

$(NiCoCrFeMn)_{100-x}Al_x$ (x=0-7) , and observed solid-solution strengthening (substitutional). However, even in this study, the strengthening effect is still relatively weak (~4 MPa per at.% Al).

In essence, $\Delta\sigma_s$ in Eq. 2.1, consists of, at the most, two terms: dislocation hardening and grain boundary hardening, with dislocation strengthening taking place within grain interior and grain-boundary strengthening occurring at/in the vicinity of the boundaries (i.e. dislocation pile-ups). In other words, if the two mechanisms work collectively, the yield strength would be

$$\sigma_y = \sigma_f + M\alpha Gb\rho^{1/2} + k_{HP}d^{-1/2} \tag{2.4}$$

or,

$$\sigma_f = \sigma_y - M\alpha Gb\rho^{1/2} - k_{HP}d^{-1/2} \tag{2.5}$$

For the yield strength of fully annealed pure Ni, we adopt data from the literature [77]:

$$\sigma_{y,Ni} = 21.8[\text{MPa}] + 158[\text{MPa}\cdot\mu\text{m}^{1/2}]d^{-1/2}[\mu\text{m}^{-1/2}] \tag{2.6}$$

Insert it into Eq. 2.5, we obtain $\sigma_{f,Ni} = 10$ MPa , where $\sigma_{f,Ni}$ is the lattice friction stress of pure Ni. Using Eq. 2.5 we can further deduce the lattice friction stresses of the fully annealed (or homogenized) Ni-based equiatomic alloys and their values along with the corresponding σ_f/G are summarized in Table 2.1. For clarity, we omit data from the $(NiCoCrFeMn)_{100-x}Al_x$ (x= 0 - 7) alloy system [15] since they contain solid-solution hardening part (although we have shown it is small).

We can now correlate the lattice friction stress as a function of lattice distortion, and it is shown in Figure 2.3. It is apparent that the lattice friction stress increases with the lattice distortion and, in fact, linearly scales with the lattice distortion. In other words, it is more difficult to move dislocations through an alloy matrix with larger lattice distortion. Similar to the

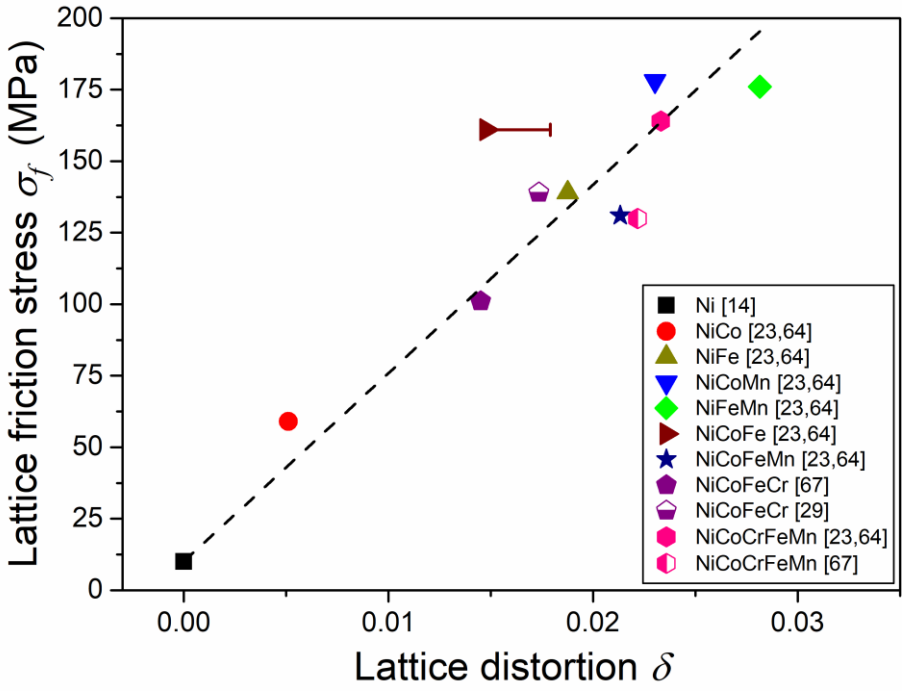

Figure 2.3 Correlation between the lattice friction stress (σ_f) and the lattice distortion (δ). The error bar of lattice distortion for NiCoFe is from Refs. [64-66].

$\Delta\sigma_y - \delta$ correlation (Figure 2.2), ternary NiCoMn and NiFeMn have the largest lattice distortion, thus the highest friction stresses in the present Ni-based equiatomic alloy systems.

According to Figure 2.3, the average value of the lattice friction stress for multicomponent (≥3) equiatomic alloys is about 130-170 MPa (~$2\times10^{-3}G$), which is about one to two orders of magnitude higher than that for the conventional fcc-metals, which is about $10^{-5}G$-$10^{-4}G$ [78]. However, it is still far less than that for the conventional bcc-metals (~$10^{-2}G$ [78]). This is consistent with the notion that yielding in the current fcc-Ni-based equiatomic alloys is more difficult than that in the traditional fcc-alloys.

The correlation between lattice friction stress and lattice distortion is rationalized in the following way. Lattice friction results from spatial perturbation in interaction between the dislocation and the lattice, which usually exhibits itself in a periodic manner and is independent

of crystalline defects. The current definition of lattice distortion parameter δ represents only the average expansion of the overall lattice. At the atomic scale, the location of each atom is actually affected by its nearest neighbors, as noted by Guo *et al* [11]. In other words, the fcc unit cell is no longer an equilateral cube, like the conventional one, but becomes irregular. The irregularity or shape of the cell is determined by the combined effect of the nearest atomic size mismatch and chemical bond. In such case, the dislocation line is not straight, but wiggled consisting of successive segments, as illustrated in Figure 2.4. Total energy of the dislocation is

$$E_d = G\sum_i b_i^2 l_i \tag{2.7}$$

where l_i is the adjacent atomic distance, G is the shear modulus, and b_i is Burgers vector. It is still unclear about the exact value of E_d because the uncertainty of l_i. However, based on the fact that δ is positive, i.e., lattice dilation, the energy of this dislocation "line" is expected to be higher than that of a perfectly straight dislocation. The energy and stress required to move such a dislocation are also expected to be higher. Quantitative evaluation of the effect of wiggled dislocation is currently not possible unless we know exactly the interatomic bonding energies between constituent atoms, which determine the bond length (or interatomic distance). Atomistic simulation may shed lights, but it would be beyond the scope of the current paper.

Another contributing factor is the possible narrowing of dislocation core. The classical theory for lattice friction stress (or Peierls stress) is described by the equation [79, 80]:

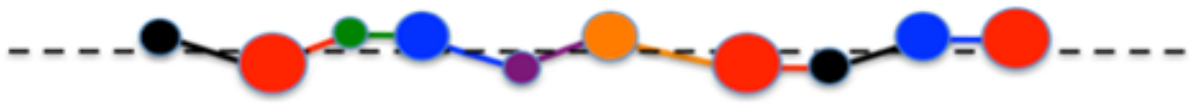

Figure 2.4 The schematic of the wiggled dislocation line in the distorted HEA lattice.

$$\tau_f = \frac{2G}{1-\nu}\exp\left[\frac{-2\pi w}{b}\right] \tag{2.8}$$

where τ_f is the lattice friction stress (shear), G the shear modulus, ν the Poisson's ratio, w the width of dislocation core, and b the Burgers vector. The dislocation core width normalized by the Burgers vector is

$$\frac{w}{b} = \frac{1}{2p}\ln\left[\frac{2MG}{s_f(1-n)}\right] \tag{2.9}$$

where $\sigma_f = M\tau_f$, and M is the Taylor factor. Insert each parameter, the values of w/b for the Ni-based equiatomic alloys are listed in Table 1 and also plotted in Figure 2.5. In comparison, pure Ni has a much higher w/b value ($w/b = 1.77$) than the Ni-based equiatomic alloys ($w/b < 1.50$), again indicating more difficult dislocation glide in the equiatomic fcc alloys. Also noted in Figure 2.5 is that, except for the binary NiCo, w/b values for the Ni-based equiatomic alloys fall within the range of 1.30-1.40 and are nearly constant ($w/b = 1.33 \pm 0.04$), indicating

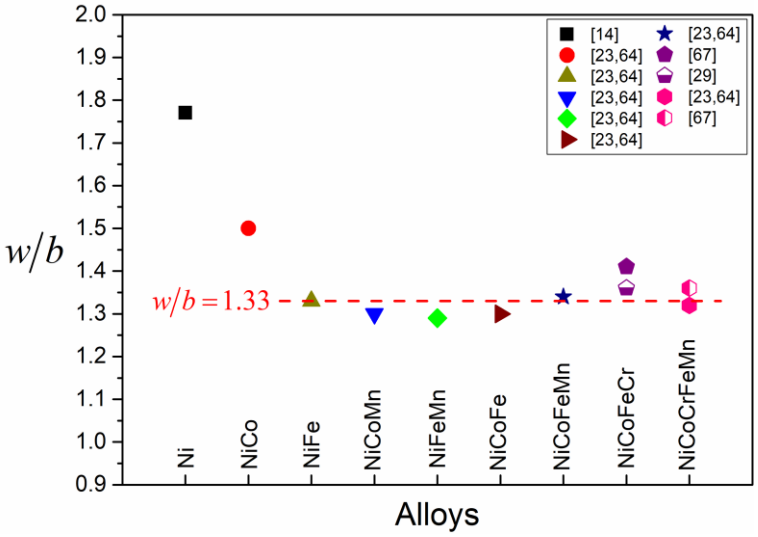

Figure 2.5 The normalized width of dislocation core (w/b) in pure nickel and Ni-based equiatomic alloys listed in Table 2.1.

that the lattice friction stress in these equiatomic alloys approximately scales linearly with $G/(1-\nu)$.

The above lattice friction-lattice distortion relationship prevails in fcc-HEAs. For HEAs with other structures, such as bcc and hexagonal close-packed (hcp), we anticipate to have a similar result. In fact, remarkable enhancement in yield strength has also been observed in these alloys [20, 28, 47, 81, 82]. However, there are insufficient data allowing for a thorough analysis at the present time.

2.3 Summary

In this chapter, I have carried out a systematic analysis of the lattice distortion in a series of Ni-based equiatomic alloys. The lattice distortion is not necessarily increased monotonically with the number of constituent elements, but also depends on the alloy chemistry. By taking into account all possible strengthening mechanisms, the lattice friction stresses in the current Ni-based alloy system were deduced and found to scale linearly with the lattice distortion. Additionally, the width of dislocation core in these Ni-based equiatomic alloys was estimated to be about 1.33*b*, where *b* is the Burgers vector, falling below the value reported for pure fcc-Ni. The higher friction stress in multicomponent equiatomic alloys may, therefore, be attributable to the wiggled dislocation line and a smaller dislocation core. The above finding suggests that the generally observed high strength in equiatomic alloys is probably not attributed to the traditional solid solution strengthening as suggested in several recent publications.

Chapter 3. A simplified model connecting lattice distortion with friction stress of Nb-based equiatomic high-entropy alloys

3.1 Model

As mentioned in Chapter 2, in the study of fcc Ni-based equiatomic alloys, we reported that lattice distortion, defined as the lattice parameter variation caused by elemental substitution, was linearly dependent on the lattice friction stress [25]. However, a physical picture for this result was not given. Here, we model the correlation as follows.

Imagine a bcc cell, for example, Nb, with a lattice constant of a_0. To build a multi-component bcc-HEA from this cell, we begin to substitute Nb atoms one-by-one with other transition elements (such as Ti, Zr, and Hf). Since the crystal structure is fixed and each newly added atom has a size and charge different from Nb, the cell will gradually distort as a result of the substitution. After finishing the substitution, the lattice constant of the cell becomes a, as schematically illustrated in Figure 3.1a. Alternatively, we can imagine the cell is mechanically strained (dilating or contracting) isotropically from the initial lattice constant a_0 to the final a. The two routes, one is chemical substitution and another mechanical straining, produce the same dilated or contracted cell. Let us assume the stored energy in the final cell is purely mechanical and all other energy forms, such as magnetic and electronic, are insignificant. In other words, from the energy viewpoint, the final cell produced via either processing route is essentially the same.

In the case of via mechanical route, we consider the elastic deformation of a cubic cell

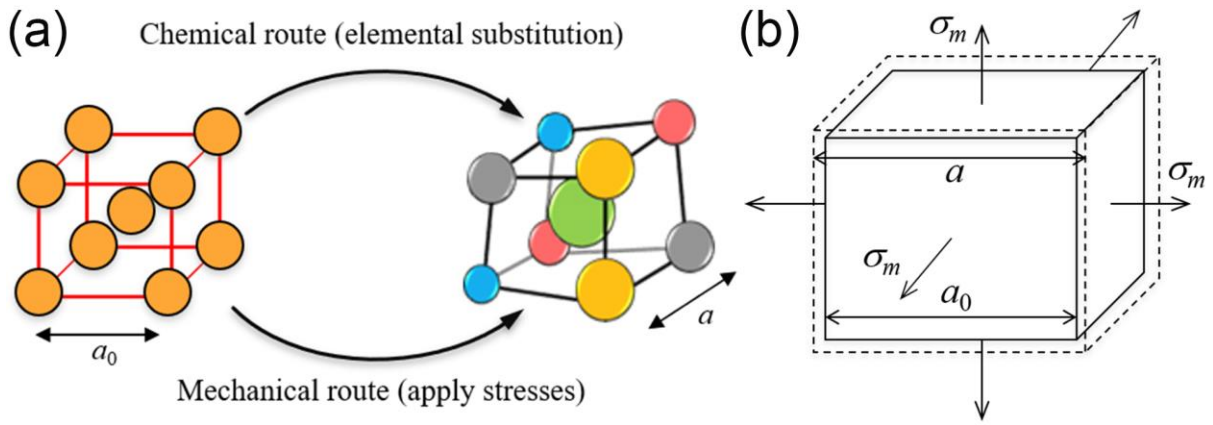

Figure 3.1 (a) Lattice distortion can be achieved either via chemical substitution or mechanical dilation/contraction. (b) Lattice constants of the initial and final (under a mean hydrostatic stress σ_m) unit cells are a_0 and a, respectively.

(Figure 3.1b). The linear (δ) and volumetric (Δ) strains are $\delta = (a - a_0)/a_0$ and $\Delta = (\Omega - \Omega_0)/\Omega_0 \approx 3\delta$, respectively, where a and a_0 are the lattice constants of the HEA and baseline Nb, and Ω and Ω_0 are cell volumes of the HEA and baseline Nb, respectively. The mean hydrostatic stress, σ_m, required to cause such deformation

$$\sigma_m = B \cdot \Delta \approx B \cdot 3\delta \tag{3.1}$$

where B is the bulk modulus of the alloy. In other words, an internal stress is stored in the final cell after elemental substitution and this stress is linearly proportional to the lattice distortion δ. In fact, we have previously reported this correlation in the study of fcc Ni-based equiatomic alloys [25]. It is particularly noted that the currently defined lattice distortion is essentially the average lattice strain, which is similar to the average $(\text{MSAD})^{1/2}$ defined by Okamoto et al [83].

In the current study, we only consider the onset of yielding and there are several pieces of evidences indicating yielding in HEAs is asymmetrical. For example, yield strength of the Cantor alloy (NiCoCrFeMn) in tension and compression are 316 MPa and 445 MPa, respectively [84], and our recent stress-strain measurements from a bcc-HEA (NbTiZrHf) also confirmed

yielding asymmetry (unpublished private data, an extension of Ref. [85]). These results led us to believe that yielding of HEAs follows a Mohr-Coulomb criterion, not von Mises. In other words, yielding of HEAs is pressure-dependent. Consequently, although hydrostatic stress created by lattice dilation/contraction cannot cause dislocations to move, it can affect the effective shear stress, thus the onset of dislocation motion.

To validate the above model, in this chapter, we carried out systematic experiments to measure the lattice friction stresses in pure Nb and a series of bcc Nb-based equiatomic alloys (from binary to quinary) and correlate them with their respective lattice distortion. For comparison, the relationship between lattice friction stress and lattice distortion in fcc Ni-based equiatomic alloys is also discussed. We will show that there exists evidently a quantitative correlation between friction stress and lattice distortion. This result offers an explanation for the unusually enhanced strength in HEAs.

3.2 Experiments

Ingots of pure Nb and Nb-containing equiatomic alloys were prepared by arc-melting mixtures of high-purity (> 99 wt.%) constituent elements in a Ti-gettered argon atmosphere. To promote chemical homogeneity, these ingots were re-melted at least eight times and, then, injected into a copper mold ($10 \times 10 \times 60$ mm^3) with water cooling. Phases microstructure of the cast alloys were examined using X-ray diffraction (Cu K_α radiation, MXP21VAHF) and scanning electron microscopy (ZEISS Supra 55) and results indicated that all samples are bcc single-phase with an average grain size of about 100 μm. Tensile tests were performed on a CMT4105 universal tensile testing machine with a nominal strain rate of 2.0×10^{-4} s^{-1} at room temperature. Flat dog-bone-shaped tensile samples were electro-discharge machined with a

gauge length of 20 mm, width of 3 mm, and thickness of 1 mm. For each alloy, at least two tensile specimens were tested. Measured values of lattice constant (a, determined by the Nelson-Riley method [86]) and 0.2% offset yield strength (σ_y) of these alloys are tabulated in Table 3.1.

3.3 Results and discussion

Before analyzing the data in Table 3.1, it is first pointed out that, in the current bcc equiatomic Nb-Ta-Ti-Zr-Hf alloy system, only Nb and Ta are bcc-metals with a nearly identical lattice constant (Nb: 0.3294 nm, Ta: 0.3303 nm [14]), while all the other constituent elements are hcp, instead. Furthermore, Nb and Ta both belong to group-VB elements in the Periodic Table, their chemical specificities (e.g., charge transfer and electronegativity) are also similar. It is, therefore, reasonable to treat these alloys as a series of Nb-based equiatomic alloys. In other words, Nb can be considered as the baseline of the equiatomic Nb-Ta-Ti-Zr-Hf alloy series and lattice distortion can subsequently be computed; δ values for these Nb-based bcc-equiatomic alloys are now included in Table 3.1.

A graphic comparison of the lattice distortion in the current Nb-based and the previous Ni-based equiatomic alloys [25] is shown in Figure 3.2. Except for binary NbTi which has a contracting lattice strain, all other bcc Nb-based and fcc Ni-based alloys show a dilating lattice strain. For the convenience of illustration, the x-axis is plotted with increasing number of constituent elements. It is evident in Figure 3.2 that lattice distortion does not simply increases with increasing number of constituent elements in either bcc Nb-based or fcc Ni-based HEAs. In actuality, ternary alloy NbZrHf has the largest lattice distortion in the Nb-based alloys.

It is also apparent that lattice distortion in the bcc Nb-based alloys is far larger than that in the fcc Ni-based alloy, especially in the ternary and quinary systems. This result is consistent

Table 3.1 Summary of lattice constant (a), lattice distortion (δ), Young's modulus (E), 0.2% offset yield strength (σ_y), the lattice friction stress (σ_f), corresponding σ_f/E, and the normalized dislocation core width (w/b) of bcc-structured, Nb-based equiatomic alloys.

Alloys	Processing[a]	a (Å)	δ	E[b] (GPa)	σ_y (MPa)	σ_f (MPa)	σ_f/E (10^{-3})	w/b	Ref.
Nb	AC	3.307	0	103	188 ± 7	130	1.3	1.25	Present work
NbTi	AC	3.292	-0.0047	92	354 ± 14	309	3.4	1.09	Present work
NbTiZr	AC	3.404	0.0292	81	749 ± 11	706	8.7	0.94	Present work
NbTiHf	AC	3.389	0.0246	94	613 ± 9	567	6.0	0.99	Present work
NbZrHf	AC	3.490	0.0551	-	-	-	-	-	[11]
NbTiZrHf	AC	3.451	0.0433	83	783 ± 17	739	8.9	0.94	Present work
NbTiZrHf	AC	3.443	0.0410	83	879	830	10.0	0.92	[87]
NbTaTiZr	AC	3.359	0.0155	112	876 ± 27	826	7.4	0.97	Present work
NbTaTiHf	AC	3.368	0.0185	110	762 ± 10	712	6.5	0.99	Present work
NbTaZrHf	AC	3.446	0.0421	103	1046 ± 15	997	9.7	0.93	Present work
NbTaTiZrHf	AC	3.421	0.0344	114	1142 ± 23	1091	9.6	0.93	Present work
NbTaTiZrHf	CR+A	3.419	0.0338	114	830	779	6.9	0.98	[88]
NbTaTiZrHf	CR+A	3.404	0.0292	114	1145	1067	9.4	0.93	[89]
NbTaTiZrHf	CR+A	3.402	0.0286	114	1114	1048	9.2	0.93	[90]
NbTaTiZrHf	CR+A	3.406	0.0298	114	940	892	7.9	0.96	[91]

[a] AC: As-Cast; A: Annealed; CR: Cold Rolled.
[b] Measured from elastic portion of tensile stress-strain curves.

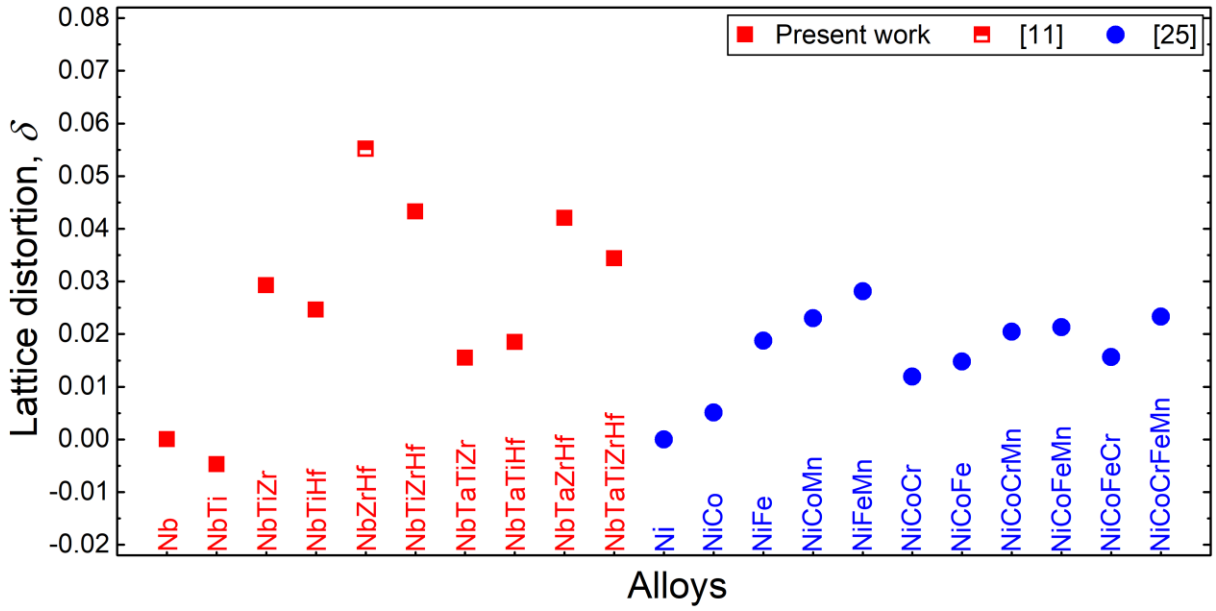

Figure 3.2 Lattice distortion (δ) in bcc Nb-based (also listed in Table 3.1) and fcc Ni-based equiatomic alloys.

with the *ab initio* calculations performed by Song *et al.* [92], who concluded that lattice distortion in bcc refractory HEAs (e.g., NbZrHf, NbTiZrHf, and NbTaTiZrHf) was significantly higher than that in fcc HEAs (e.g., NiCoFe, NiCoFeCr, and NiCoCrFeMn).

Lattice distortion in HEAs can result in a strengthening effect. To evaluate this effect, the nature of yield strengths of the current Nb-based equiatomic alloys in Table 3.1 must first be clarified. Yield strength of an alloy (σ_y) generally consists of two parts (intrinsic and extrinsic),

$$\sigma_y = \sigma_f + \Delta\sigma_s \tag{3.2}$$

or

$$\sigma_f = \sigma_y - \Delta\sigma_s \tag{3.3}$$

where σ_f is the friction stress (or intrinsic strength) and $\Delta\sigma_s$ refers to all possible strengthening contributions, including the solid-solution strengthening, dislocation strengthening, grain-boundary strengthening, and precipitation strengthening. However, it is noted that these strengthening mechanisms are all assumed absent in the model (Figure 3.1) and the internal

stress described in the model is actually the friction stress. In contrast, the experimentally measured yield strengths listed in Table 3.1 possibly contain contributions from the above mechanisms. To deduce the friction stress, it is necessary to subtract their contributions. For brevity and clarity, a summary of the calculated strengthening contributions is presented in Table 3.2.

A particular note about the precipitation strengthening in Table 3.2 is that, in the current Nb-based equiatomic alloys, precipitates are absent. As mentioned before, no second phase was discernible in these bcc-alloys, based on scanning electron microscope and X-ray diffraction analyses. Lei *et al*. [85] also confirmed that the as-cast equiatomic NbTiZrHf alloy did not contain any precipitate using neutron diffraction and scanning transmission electron microscopy. Consequently, precipitation strengthening is excluded here.

Another note is about the solid-solution strengthening. As pointed out before [25], contribution from solid-solution strengthening in equiatomic alloys can be, in principle, ignored.

Table 3.2 Strengthening effects produced by various mechanisms in the current bcc Nb-based equiatomic alloys.

Strengthening mechanisms	Solid-solution strengthening	Dislocation strengthening[a]	Grain-boundary strengthening[b]	Precipitation strengthening
Equation	NA	$\Delta\sigma_d = M\alpha Gb\rho^{1/2}$ [72]	$\Delta\sigma_{gb} = k_{HP}d^{-1/2}$ [93]	NA
Calculated value (MPa)	NA	19-27	~ 24	NA

[a] M : Taylor factor, $M = 2.75$ [73]; α : an empirical constant, $\alpha = 0.4$ [73]; G : shear modulus, $G = 0.367E$ [94]; b : Burgers vector, $b = (\sqrt{3}/2)a$; ρ : dislocation density ($\rho \sim 4\times10^{12}\,\mathrm{m}^{-2}$ from fully annealed Nb [95] was adopted).
[b] $k_{HP} = 240\ \mathrm{MPa}\cdot\mu\mathrm{m}^{1/2}$ from fully annealed NbTaTiZrHf [91] was adopted for calculations, since k_{HP} is not available for the majority of the concentrated alloys. For pure Nb, $k_{HP} = 340\ \mathrm{MPa}\cdot\mu\mathrm{m}^{1/2}$ [96]; d : average grain size.
NA: not applied.

According to the traditional solid-solution strengthening theories, when moving dislocations travel through a solvent lattice, they will encounter resistance from local lattice distortion caused by the mismatch between solvent and solute atoms. However, in equiatomic alloys, lattice distortion is quite uniform and global, as long as the constituent atoms are randomly partitioned in the lattice, and they indeed are [97, 98]. In this case, dislocations are envisioned to travel through a heavily distorted lattice, which yields a highly distorted Peierls potential landscape. Since the solute content is negligible in these alloys, contribution from solid-solution strengthening can also be excluded.

Using available data for Nb-based equiatomic alloys in Table 3.2, lattice friction stresses can now be readily deduced from Eq. 3.3 and their values are presented in Table 3.1. For easy discussion, we express friction stresses in a normalized form (σ_f/E) and present these values also in Table 3.1. It is apparent that the normalized friction stresses of bcc Nb-based equiatomic alloys are generally much higher than those of fcc Ni-based equiatomic alloys. In perspective, the normalized friction stresses (σ_f/E) of some bcc metals, fcc Ni-based and the current bcc Nb-based multicomponent (≥ 3) equiatomic alloys are listed together in Table 3.3. It is readily seen that σ_f/E of fcc Ni-based alloys are actually close to those of the traditional bcc metals, but σ_f/E of bcc Nb-based alloys are about one order of magnitude higher. This result is

Table 3.3 Normalized friction stresses (σ_f/E) of the traditional bcc metals, bcc Nb-based, and fcc Ni-based equiatomic alloys (number of components ≥ 3).

Material	Ni-based [25]	Nb	Ta [99]	Mo [99]	W [99]	Nb-based
σ_f/E (10^{-3})	0.5-1.0	1.3	0.6	0.4	0.7	6.0-10.0

consistent with the notion that dislocation motion in bcc Nb-based equiatomic alloys is more difficult than that in the conventional bcc alloys.

It is noted again that, in the current model (Figure 3.1), the internal stress is actually the stress increment with respect to the intrinsic stress of the initial "undeformed" cell, which is the pure bcc-Nb. Therefore, to validate the model, we must further subtract the measured lattice friction stresses from the friction stress of Nb, that is, $\Delta\sigma_f = \sigma_{f,HEA} - \sigma_{f,Nb}$, where $\Delta\sigma_f$ is the internal stress, and $\sigma_{f,HEA}$ and $\sigma_{f,Nb}$ are the friction stresses of HEA and Nb, respectively.

According to Eq. 3.1, this internal stress is dependent linearly upon the bulk modulus. Since bulk modulus (B) and Young's modulus (E) are also linearly proportional [100], the internal stress is finally scaled with lattice distortion as $\Delta\sigma_f \propto \sigma_m \propto E \cdot 3\delta$, or $\Delta\sigma_f / E = c\delta$, where c is the scaling constant. The functional relationship between the normalized internal stress ($\Delta\sigma_f / E$) and lattice distortion (δ) for the Nb-based alloys is plotted in Figure 3.3, in which the error bars were calculated from estimated uncertainties of dislocation densities (ρ) and the Hall-Petch coefficients (k_{HP}) in these alloys. It is particularly noted that, in the figure, we use a positive strain for NbTi since it is perceived that the interaction between dislocation and distorted lattice is similar to the solute-dislocation interaction based on solid-solution theories [19, 101]. According to these theories, when lattice strain is dominant, dilation and contraction can cause identical strengthening effect. It is evident in Figure 3.3 that, despite some data scatter, a linear relationship between the two variables is apparent, satisfactorily validating our model. As mentioned before, the linear correlation has also been observed in the fcc Ni-based equiatomic alloys [14, 23, 29, 64, 67]. For direct comparison, data from the fcc Ni-based equiatomic alloys are also included in Figure 3.3. Readily noted in the figure is the fact that bcc

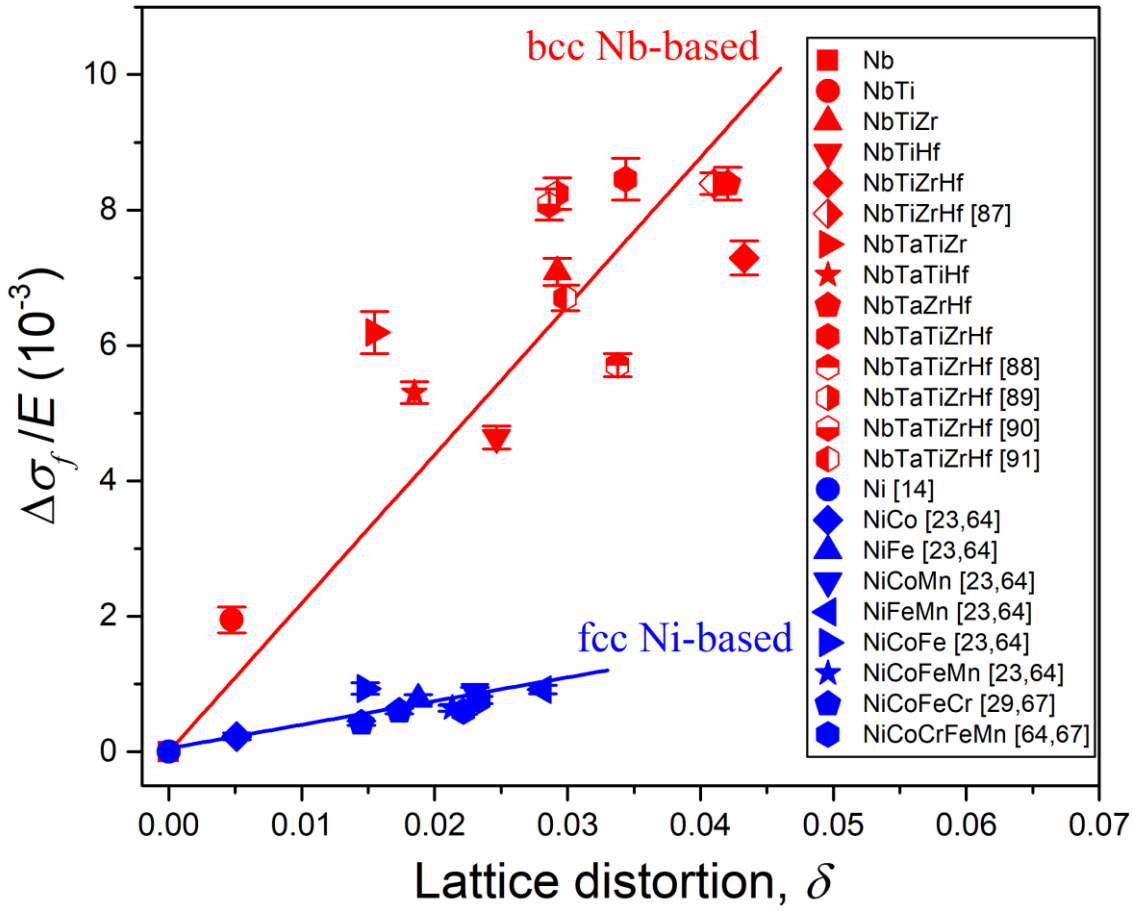

Figure 3.3 Correlation between the normalized internal stress ($\Delta\sigma_f/E$) and lattice distortion (δ) in bcc Nb-based and fcc Ni-based equiatomic alloys. The error bars are based on estimated uncertainties of dislocation densities and the Hall-Petch coefficients in these alloys.

Nb-based alloys are more sensitive to lattice distortion ($c = 0.219$) than fcc-Ni based equiatomic alloys ($c = 0.035$). Furthermore, the larger data variation in bcc Nb-based alloys may be caused by the inconsideration of magnetic and electric energies, and a non-Schmid effect in the model. For the non-Schmid effect and in the case of fcc-based HEAs, there are several reports indicating that single crystalline HEAs follow Schmid's Law [102, 103]. To our best knowledge, similar result has not yet been reported in single-crystal bcc HEAs. However, since the yielding of bcc metals often does not obey Schmid's Law [104-106], it is conceivable that dislocation slip in bcc-HEAs may also occur in a non-Schmid fashion. At the present moment, the evaluation of these non-Schmid factors in equiatomic alloy systems is challenging and obviously beyond the scope of our simplified model. Nevertheless, to improve the model's predictability it will be considered and included in the future.

Peierls stress is usually regarded as the lattice friction stress and it is given as [80]:

$$\tau_f = \frac{2G}{1-\nu}\exp\left[\frac{-2\pi w}{b}\right] \tag{3.4}$$

where τ_f is the friction shear stress, G is the shear modulus, ν is the Poisson's ratio (Note: ν is not available for the majority of the Nb-based alloys, thus we borrow it from the Poisson's ratio of Nb), w is the width of dislocation core, and b is the Burgers vector. The dislocation core width normalized by the Burgers vector (w/b) is, then,

$$\frac{w}{b} = \frac{1}{2\pi}\ln\left[\frac{2MG}{\sigma_f(1-\nu)}\right] \tag{3.5}$$

where $\sigma_f = M\tau_f$, and M is the Taylor factor. Values of w/b in Nb-based equiatomic alloys are calculated and listed in Table 3.1. A graph comparing the normalized dislocation core width of the bcc Nb-based and fcc Ni-based alloys is shown in Figure 3.4.

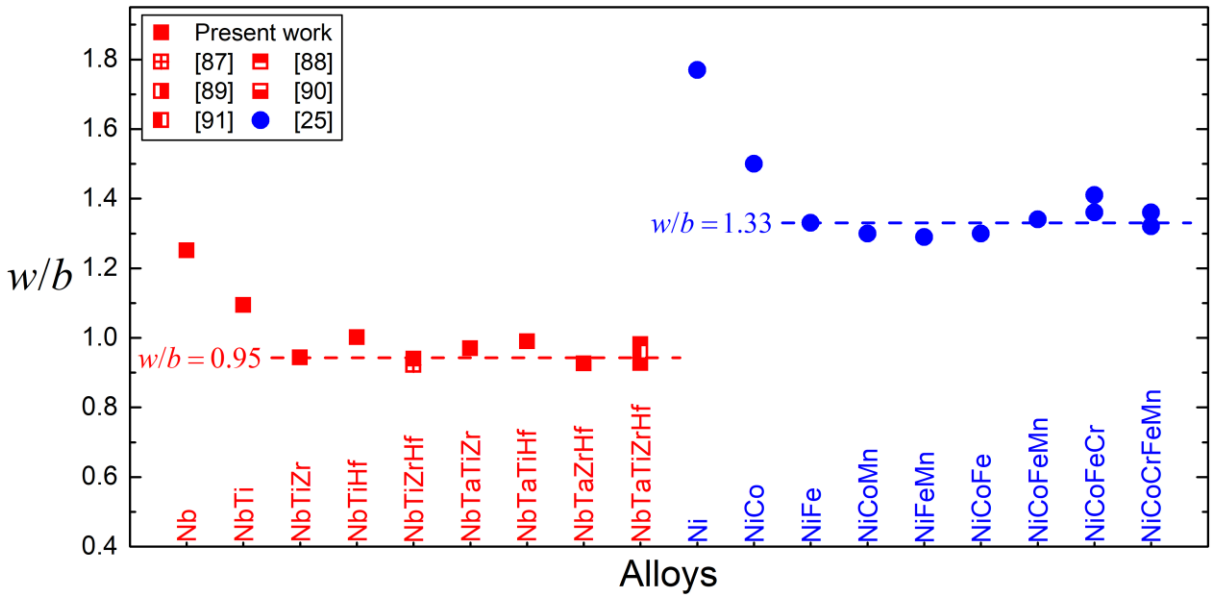

Figure 3.4 The normalized dislocation core width (w/b) in bcc Nb-based and fcc Ni-based equiatomic alloys.

It is apparent in the figure that pure Nb has a higher w/b value ($w/b = 1.25$) than the Nb-based equiatomic alloys ($w/b < 1.10$), indicating that dislocation glide is more difficult in the equiatomic alloys. Also noted is that w/b values in these Nb-based equiatomic alloys (except for the pure Nb and binary NbTi) fall within the range of 0.92-0.99 and are almost constant ($w/b = 0.95 \pm 0.03$), similar to that observed in the Ni-based equiatomic alloys, suggesting that entropy effect becomes appreciable and effective only when the number of principal elements is higher than three, that is, ternary systems (so-called medium entropy alloys). It is consistent with the notion that NiCoCr [107] and NiCoV [108] medium entropy alloys often exhibit some unusual mechanical properties, such as ultra-strength (> 1 GPa) with decent ductility (> 20%). Furthermore, the w/b values for bcc Nb-based alloys are noted to be much lower than those for fcc Ni-based equiatomic alloys ($w/b = 1.33 \pm 0.04$), which is consistent with the notion that lattice friction stress of bcc Nb-based alloys is much higher than that of fcc Ni-based equiatomic alloys.

3.4 Summary

In this chapter, I have quantitatively evaluated the lattice distortion in a series of single-phase, bcc-structured, Nb-based equiatomic alloys. The magnitude of lattice distortion in these bcc alloys does not necessarily increase with increasing number of constituent components and is larger than that in fcc Ni-based equiatomic alloys. After removing the strength contributions from all possible mechanisms, the lattice friction stress of each of the current Nb-based alloys is extracted and it is found that friction stress scales linearly with the lattice distortion in these alloys. In addition, lattice distortion in bcc Nb-based alloys can apparently produce a much stronger hardening effect than that in fcc Ni-based equiatomic alloys. The much higher friction stress of bcc-HEAs compared to that of fcc-HEAs may be attributed to a smaller dislocation core. The current results suggest that remarkable strength enhancement in HEAs is probably resulted from a high friction stress, which is, in turn, caused by lattice distortion.

Chapter 4. Thermal stability and coarsening of coherent particles in a precipitation-hardened $(NiCoFeCr)_{94}Ti_2Al_4$ high-entropy alloy

In this chapter, we examined the evolution of morphology, size and distribution of $L1_2$ precipitates in the fcc-$(NiCoFeCr)_{94}Ti_2Al_4$ alloy as a function of aging time and temperature using electron microscopes. The activation energy for precipitate coarsening is evaluated and compared with relevant data for the diffusion of constituent elements in Ni-based alloys. Finally, precipitation strengthening effect in the current HEA is estimated and validated experimentally.

4.1 Experiments

Ingots with a nominal composition of $(NiCoFeCr)_{94}Ti_2Al_4$ (all compositions in this study are in at.%) were prepared by arc-melting mixtures of the constituent elements (purity > 99 wt.%) under a Ti-gettered argon atmosphere. The resulting buttons were re-melted at least four times to promote chemical homogeneity and subsequently drop cast into a water-cooled copper mold with a dimension of $10 \times 10 \times 60$ mm^3. The as-cast ingots were homogenized at 1200 °C for 4 h and, then, cold rolled to 70% reduction in thickness. The rolled plates were subsequently annealed at 1000 °C for 4 h, followed by water quenching to obtain a stable and fully recrystallized microstructure. Samples were sliced from the annealed plates, aged at temperatures of 750, 775, 800, and 825 °C, for time durations between 0.5 and 1022 h to examine precipitate morphology and distribution.

Preliminary precipitate characterization was carried out on a Zeiss Auriga scanning

electron microscope (SEM) and an FEI Tecnai G2 F30 transmission electron microscope (TEM) operated at 300 kV. Atomic-resolution high-angle annular dark-field scanning transmission electron microscopy (HAADF-STEM) observations were performed on an FEI Titan G2 60–300 ChemiSTEM microscope equipped with a spherical aberration probe corrector and a Super-X energy dispersive X-ray spectrometry (EDS) system operated at 300 kV. Samples for SEM observations were mechanically ground, polished (using 1 μm diamond paste for the final polish), and then electrochemically polished in a mixed solution of $HClO_4$:C_2H_6O = 1:9 (volume ratio) at 30 V at room temperature. TEM/STEM specimens were initially ground to a thickness of about 50 μm, punched into disks of 3 mm in diameter, and then thinned by twin-jet electropolishing in a mixed solution of HNO_3:CH_4O = 1:4 at 28 V and a temperature of -40 °C.

The precipitate size was defined using an area-equivalent diameter (i.e., $diameter = 2\sqrt{area/\pi}$) measured from TEM or SEM micrographs. The average precipitate size, *d*, was calculated according to precipitate size distributions. The standard error (SE) in *d* was obtained using $SE = \sigma/\sqrt{N}$, where σ is the standard deviation of precipitate sizes and *N* is the number of precipitates. The precipitate volume fraction, ϕ, was estimated by $\phi = A_f$ [109], where A_f is the projected areal fraction of precipitates. The precipitate number density, n_v, was determined from $n_v = n_a/d$ [109], where n_a is the areal density of precipitates. At least 3 TEM or SEM images from 3 different grains were used in determining *d*, ϕ, and n_v. Standard errors for ϕ and n_v were calculated based on counting statistics using standard error propagation methods [110].

Nanoindentation hardness was measured on electropolished samples using a Hysitron TI 900 TriboIndenter, with a Berkovich indenter (tip radius = 280 nm) at room temperature.

Indentation tests were performed at a 10 μm interval, with a loading rate of 1600 μN s^{-1}, a peak load of 8000 μN, and a holding time of 2s. In order to minimize grain orientation effects, at least 3 randomly selected grains were measured, and 36 indentations were made on each grain. All the indentations were conducted in load control mode.

4.2 Results

4.2.1 Morphology and nature of precipitates

After aging the $(NiCoFeCr)_{94}Ti_2Al_4$ alloy at temperatures above 650 °C, nano-sized $L1_2$ particles begin to precipitate in grains [29, 39]. The morphology and distribution of these precipitated particles as a function of aging time at 800 °C are shown in dark-field TEM image (Figure 4.1a) and SEM images (Figures 4.1b-d). The electron diffraction pattern (inset of Figure 4.1a) shows the presence of $L1_2$-ordered structure well dispersed in the fcc-matrix. The average size of precipitated particles apparently increases with increasing aging time. For instance, the size of particles is only 8.9 ± 0.1 nm after aging for 0.5 h, but increases to an average value of 69.9 ± 1.9 nm after aging for 503 h. On the other hand, the precipitate number density decreases with increasing aging time. Specifically, when the aging time increases from 0.5 h to 503 h, the number density decreases from $(2.7 \pm 0.4) \times 10^{23}$ m^{-3} to $(6.4 \pm 0.2) \times 10^{20}$ m^{-3}.

It should be noted that the $L1_2$ precipitates (Figures 4.1a-d) are essentially spheroidal and uniformly distributed throughout the fcc-matrix. These particles become larger, but still remain spheroidal even after being aged for 503 h (Figure 4.1d). Similar spheroidal morphology of $L1_2$ precipitates has been reported in Ni-rich Ni-Cr-Al [111-113] alloys. However, in many Ni-based alloys [34, 114-122], cuboidal particles aligned along the ⟨100⟩ matrix direction have also been

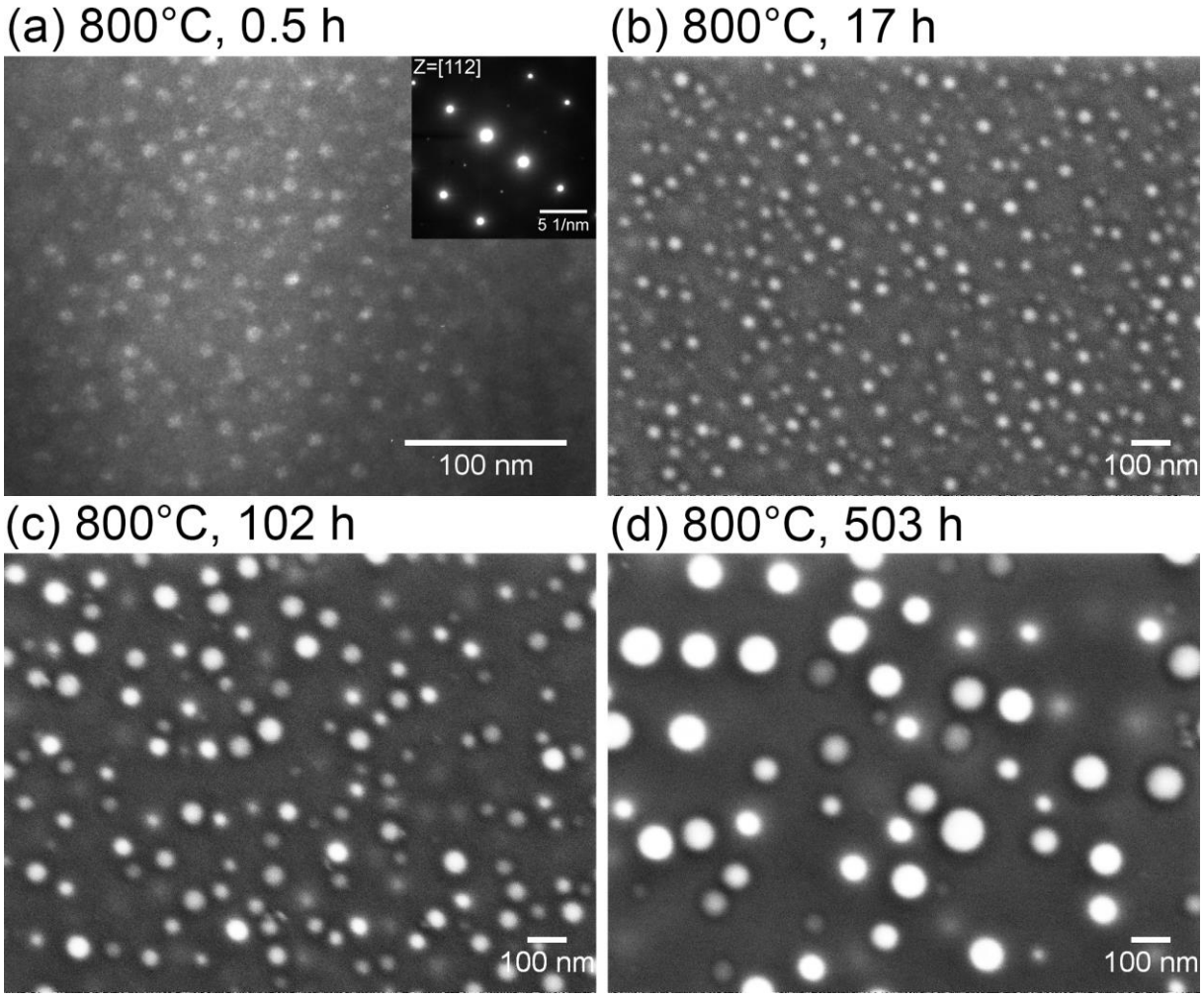

Figure 4.1 Dark-field TEM image (a) and SEM images (b-d) of $L1_2$ precipitates in the $(NiCoFeCr)_{94}Ti_2Al_4$ alloy after aging at 800 °C for: (a) 0.5 h; (b) 17 h; (c) 102 h; and (d) 503h. The inset in (a) shows the corresponding selected area electron diffraction pattern taken with the incident electron beam parallel to $[112]_{matrix}$.

observed. The difference in shape is apparently related to the size of precipitates and the precipitate/matrix interface, which will be discussed later.

To further examine the nature of these $L1_2$ precipitates, high resolution HAADF-STEM was employed, and the results are shown in Figure 4.2. After aging at 750°C for 72 h, ordered $L1_2$ particles with a diameter of ~ 25 nm were clearly revealed in the HAADF-STEM image (Figure 4.2a). Fast Fourier transform (FFT) patterns derived from the matrix (Figure 4.2b) and the precipitate (Figure 4.2c) indicate that the $L1_2$ particle exhibits a cube-on-cube orientation relationship with the fcc matrix. An enlarged image of the interface region between the precipitate and matrix (outlined by the red square frame in Figure 4.2a) is given in Figure 4.2d. It is apparent in the image that the $L1_2$ precipitate oriented along the [001] matrix direction is actually not perfectly spherical, but enclosed by facets parallel to the {100} and {110} planes. It is particularly noted in Figure 4.2d that the darker spots correspond to selectively partitioned Al atoms, since Al has the lowest atomic number among the constituent elements and the contrast of HADDF images is, in principle, scaled with the square of the atomic number [123]. From the relative contrast of the atomic image, we may conclude that the precipitate is Al-rich with Al atoms occupying the corner positions of the $L1_2$ superlattice.

Qualitative chemical analysis of the nano-sized $L1_2$ particles was also performed using STEM-EDS. Figure 4.3a is a HAADF-STEM image showing spheroidal precipitates in the $(NiCoFeCr)_{94}Ti_2Al_4$ alloy aged at 750 °C for 72 h. The corresponding STEM-EDS elemental mapping images for different constituent elements are shown in Figures 4.3b-g. These $L1_2$ particles are apparently enriched in Ni, Ti and Al, but depleted in Co, Fe and Cr, which is consistent with the previous observation [29], namely, precipitates are $L1_2$-ordered Ni_3(Al, Ti)-type particles.

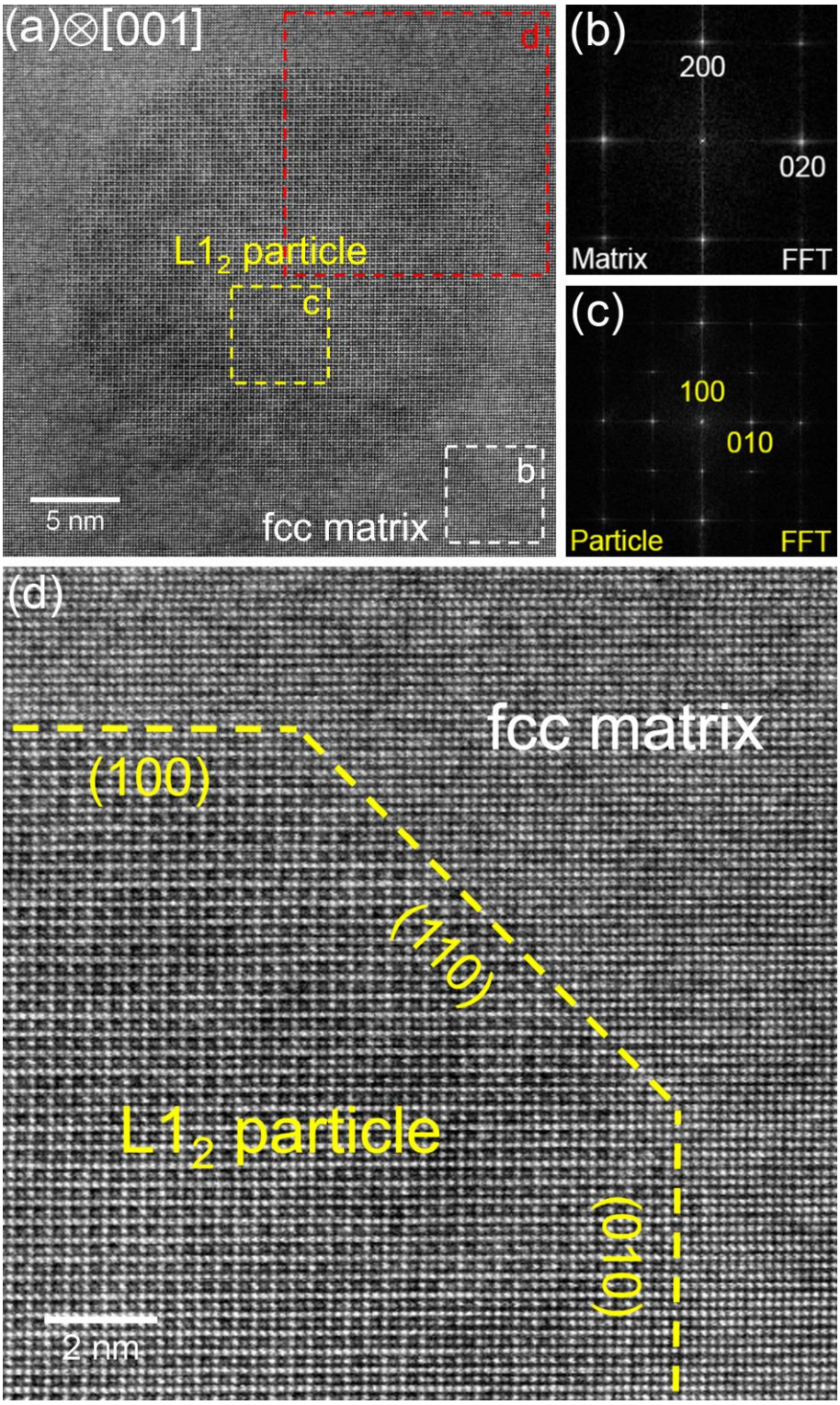

Figure 4.2 (a) HAADF-STEM image of a $L1_2$ particle after aging the $(NiCoFeCr)_{94}Ti_2Al_4$ alloy at 750°C for 72h. FFT patterns obtained from (b) the fcc matrix and (c) the $L1_2$ particle are also given. (d) Enlargement of the red frame section in (a) showing the precipitate/matrix interface region. The electron incidence direction is parallel to $[001]_{matrix}$.

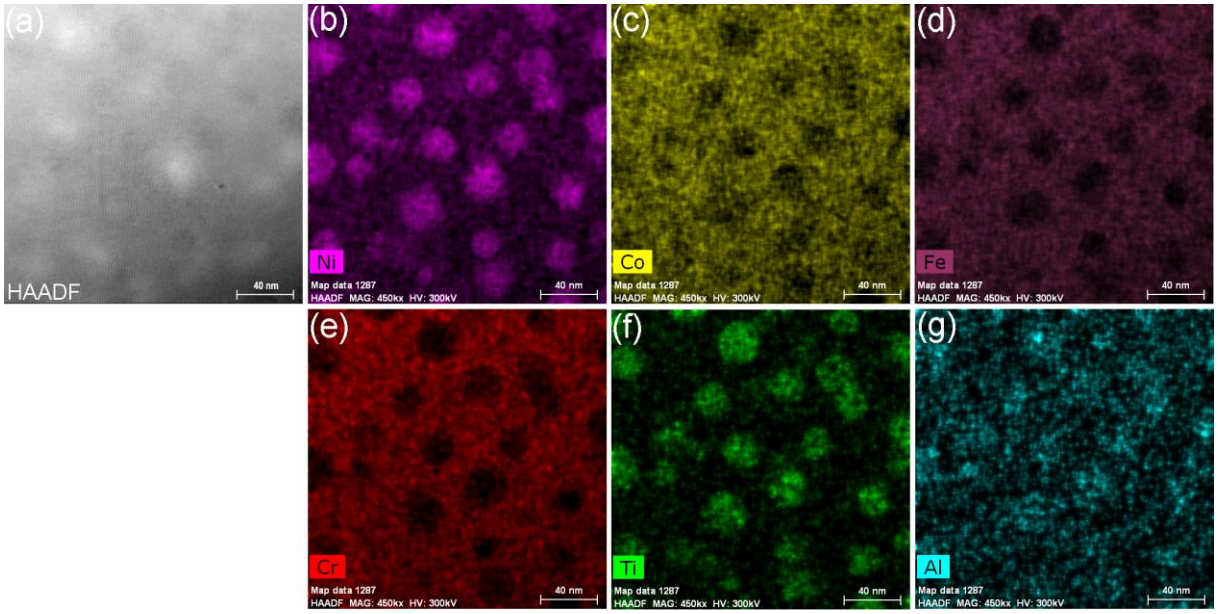

Figure 4.3 HAADF-STEM and corresponding STEM-EDS elemental mapping images of $L1_2$ precipitates in the $(NiCoFeCr)_{94}Ti_2Al_4$ alloy aged at 750 °C for 72 h. (a) Representative HAADF-STEM image of precipitates. (b-g) STEM-EDS maps for Ni, Co, Fe, Cr, Ti and Al, respectively.

4.2.2 Precipitate size and distribution

Precipitate size distribution (PSD) histograms plotted as the probability density (P) against the normalized particle size ($\rho = diameter/average\ diameter$) for the studied alloy aged at 800 °C for various periods of time are shown in Figure 4.4. It is readily seen in Figures 4.4a-d that the PSDs broaden with reduced peak height as the aging time increases, suggesting larger precipitates grow at the expense of smaller ones. Since the shape of these PSDs is not self-similar, it suggests that steady-state coarsening is probably still not yet reached [124]. For comparison, predictions of the simple LSW [41, 42] and the LSEM (precipitate volume fraction = 10%) [125] models are also superimposed over each histogram. The LSW model assuming zero volume fraction of precipitates, gives an asymmetric (left-skewed) PSD with the maximum probability occurring at ρ = 1.14 [41, 42]. In comparison, the LSEM model, which includes the effect of preexisting precipitates and possible coalescence between particles during coarsening,

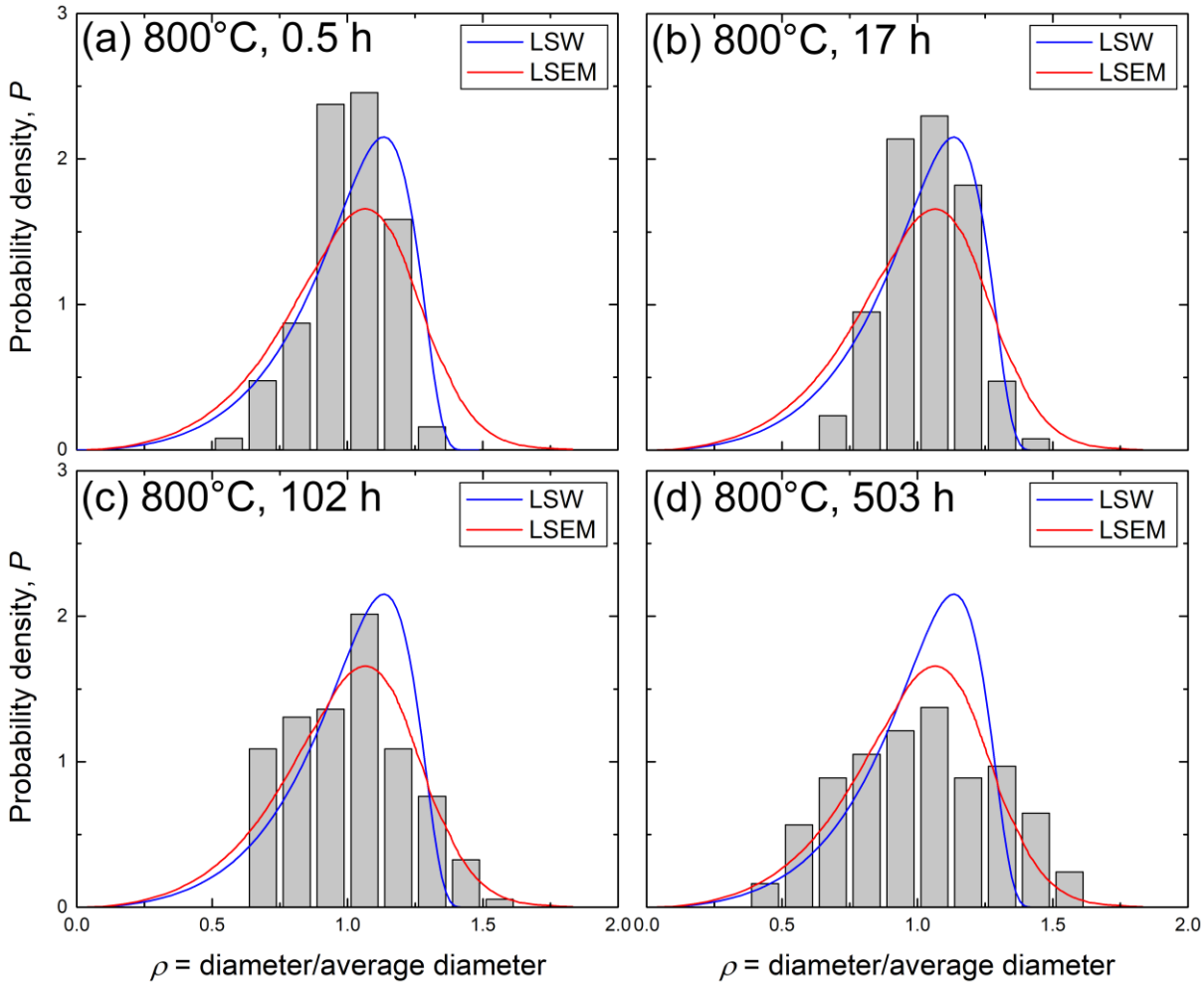

Figure 4.4 Precipitate size distributions of the $(NiCoFeCr)_{94}Ti_2Al_4$ alloy aged at 800 °C (precipitate volume fraction = 12.7%) for: (a) 0.5; (b) 17; (c) 102; and (d) 503 h. Theoretical predictions of the LSW (blue line) and LSEM (precipitate volume fraction = 10%, red line) models are superimposed for comparison.

predicts a flatter, broader and more symmetric PSD with the maximum probability occurring at ρ = 1.07 [125]. As shown in Figures 4a-4d, the peak value of the experimental PSDs is at ρ = 1.06, which agrees well with both the theoretical predictions considering the histogram bin width of 0.125. In the early stage of coarsening ($t \leq 102$ h, Figures 4.4a-c), the PSDs are asymmetric with a sharper decline on the right side of the peak, making the LSW model a better fit to the experimental results than the LSEM model. However, the PSD becomes more symmetric at a long aging time ($t \geq 503$ h, Figure 4.4d), making the LSEM model to fit better to the experimental data. This suggests that coalescence of particles might have occurred in the late stage of coarsening, which caused the discrepancy. Particle coalescence during coarsening has also been observed in a number of Ni-based alloys [114, 122, 125, 126].

4.2.3 Temporal evolution of precipitates

Time dependence of volume fraction ($\phi(t)$), number density ($n_v(t)$), and average size ($d(t)$) of $L1_2$ precipitates in the $(NiCoFeCr)_{94}Ti_2Al_4$ alloy aged at various temperatures is presented in Figure 4.5. As shown in Figure 4.5a, the value of $\phi(t)$ is virtually constant with respect to the aging times (0.5-1022 h) at each temperature. This result indicates that the precipitation process has already bypassed the nucleation and is well into the coarsening stage, thereby $\phi(t)$ approaches its equilibrium value (ϕ_{eq}). It is also noted that ϕ_{eq} decreases with increasing temperature. Specifically, when the aging temperature is raised from 750 °C to 825 °C, ϕ_{eq} decreases from 25.5% to 10.1%. The decrease of ϕ_{eq} with increasing temperature agrees with the fact that, in the nickel-rich end of the Ni-Al phase diagram, the volume fraction of $L1_2$ phase decreases with increasing temperature [114].

The precipitate number density, $n_v(t)$, as a function of the aging time is plotted in Figure

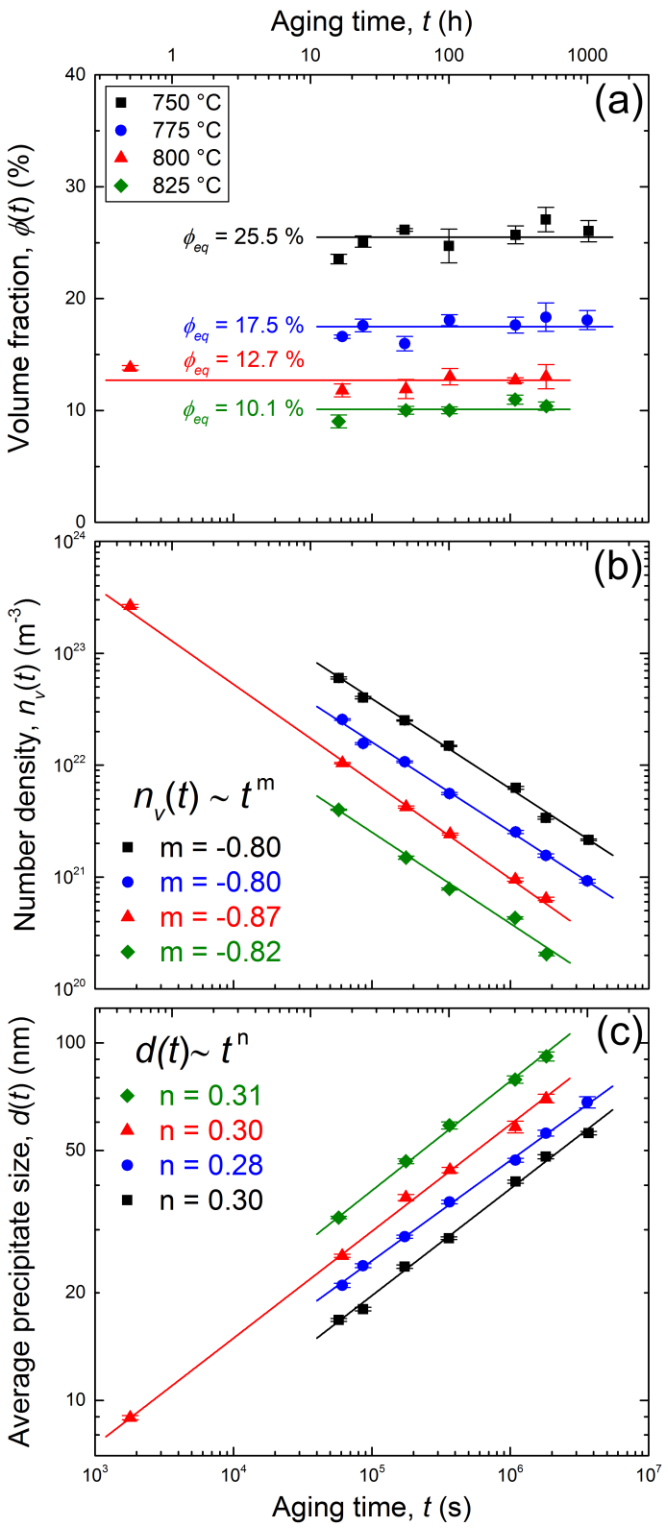

Figure 4.5 Temporal evolution of (a) volume fraction ($\phi(t)$), (b) number density ($n_v(t)$), and (c) average size ($d(t)$) of $L1_2$ precipitates in the $(NiCoFeCr)_{94}Ti_2Al_4$ alloy aged at temperatures of 750-825 °C. Solid lines in (a) and (b, c) represent the average values and linear fits of the experimental data, respectively (black line: 750 °C, blue line: 775 °C, red line: 800 °C, green line: 825 °C).

4.5b, which consistently shows a power-law relationship between the two variables at a given temperature. Specifically, the power-law exponents for $n_v(t)$, or the slopes of the linear fitted curves, are -0.80, -0.80, -0.87 and -0.82 at 750, 775, 800, and 825 °C, respectively, with an average value of -0.82 ± 0.03. Similar temporal exponents have also been reported before in some Ni-Al-based ternary alloys [113, 118, 120, 126].

As the number density depends on time, the size of precipitates also varies with time. As shown in Figure 4.5c, the average precipitate size, $d(t)$, increases with the aging time and also follows a power-law relationship. The power-law exponents are determined to be 0.30, 0.28, 0.30 and 0.31 at 750, 775, 800, and 825 °C, respectively, with an average value of 0.30 ± 0.01. Notably, a similar value of 0.29 ± 0.05 was also obtained during the coarsening of $L1_2$ precipitates in a Ni-rich Ni-Cr-Al alloy at 600 °C [112].

4.2.4 Mechanical response

To correlate mechanical strength of the $(NiCoFeCr)_{94}Ti_2Al_4$ alloy with the morphology of the $L1_2$ precipitates, we carried out nano-hardness measurements on aged samples. Aging curves of the alloy are presented in Figure 4.6. The shape of these aging curves is familiar and often observed in traditional age-hardened alloys [73], namely, hardness first increases, reaches a peak and, then, decreases with further aging. Also noted in the figure is the result that aging at a higher temperature produces an earlier and lower peak hardness. For example, at 750, 775 and 800 °C, times to reach the peak hardness are 48, 24 and 17 h, and the corresponding peak hardness values are 5.96, 5.50 and 5.30 GPa, respectively. It is particularly noted that, comparing to the binary Ni-Al [127], Ni-Ti [128] alloys and some Ni-based superalloys [129], aging time required to reach the peak aging in the current HEA (48 h at 750 °C) is much longer than that in these Ni-based alloys counterparts (less than 10 h at 750 °C). It is consistent with the notion that

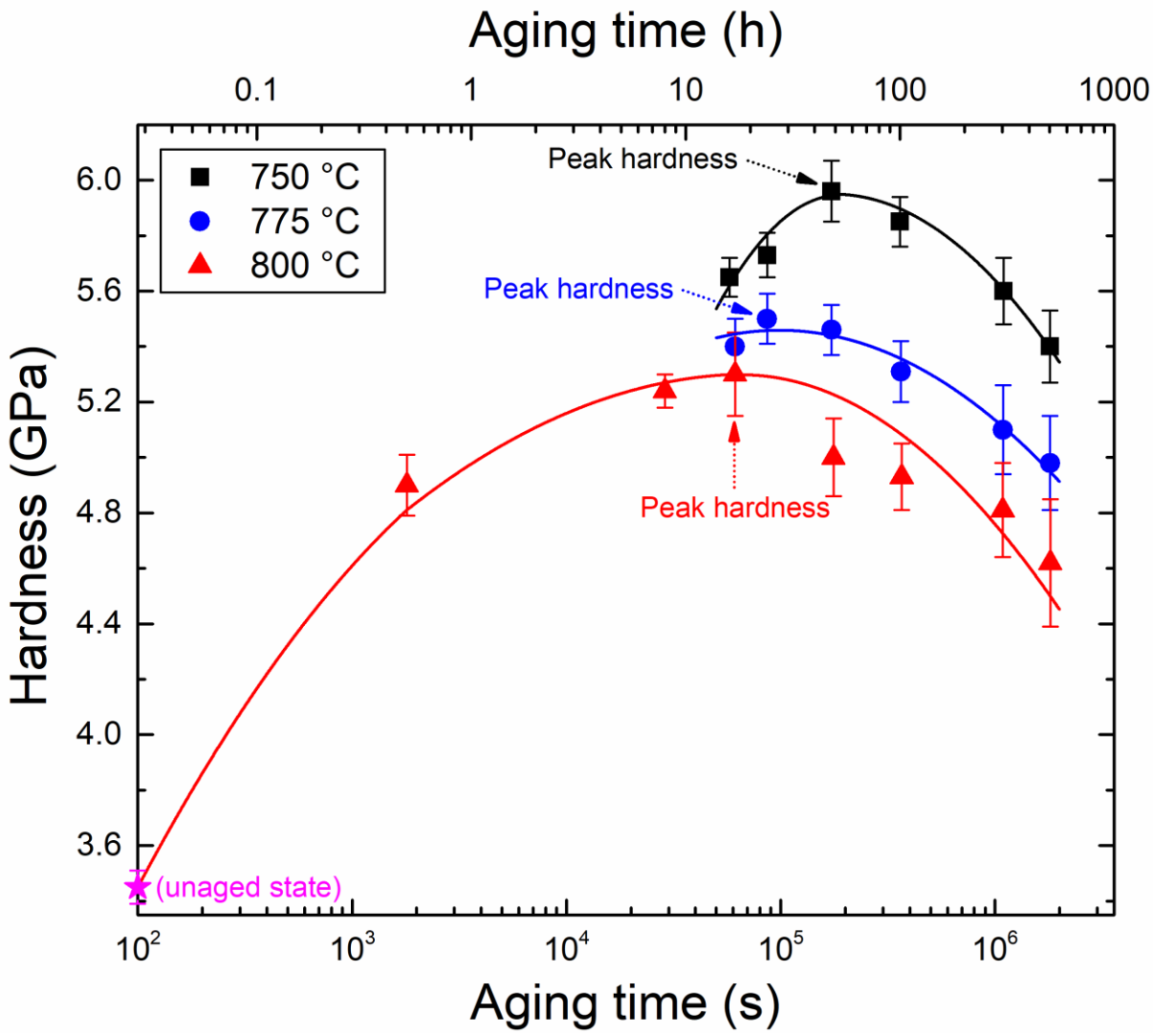

Figure 4.6 Nanoindentation hardness versus aging time for the $(NiCoFeCr)_{94}Ti_2Al_4$ alloy aged at 750 °C, 775 °C, and 800 °C, respectively. Solid lines are nonlinear fits of the experimental data (black line: 750 °C, blue line: 775 °C, red line: 800 °C).

diffusion is generally sluggish in multicomponent HEAs [8].

4.3 Discussion

4.3.1 Morphology of precipitates

The equilibrium shape of precipitated particles is controlled by minimizing the total energy, including the elastic and interfacial energies, of a system [130]. For small precipitates, elastic strain energy from lattice mismatch at the precipitate/matrix interface is small, therefore, the morphology is primarily determined by minimizing the surface area of the precipitates, which leads to spheroidal particles. As precipitates grow, the elastic energy gradually takes over and becomes dominant. In the case of Ni-based alloys, γ′ precipitates usually grow from the initial spheroid to a cuboidal shape [131]. The relative contributions of the elastic and interfacial energy to the total energy can be quantified using the *L* parameter [130] defined as:

$$L = \frac{\varepsilon^2 C_{44} r}{\sigma} \tag{4.1}$$

where ε is the lattice mismatch strain, defined as $\varepsilon = (a_p - a_m)/a_m$, where a_p and a_m are the lattice constants of the $L1_2$ precipitate and fcc-matrix, respectively, C_{44} is an elastic constant of the matrix, r is the average precipitate radius, and σ is the precipitate/matrix interfacial energy. For Ni-based alloy systems with a dilatational mismatch, it has been demonstrated that, at increasing particle size, the equilibrium shape of particles transits gradually from a sphere ($L = 0$) to spheroidal with a 4-fold symmetry, and then bifurcates to 2-fold symmetric object, like a platelet, at a higher L value ($L > 5.6$) [130].

Unlike most Ni-based alloys in which the γ′ precipitates are cuboidal and aligned along

⟨100⟩ matrix direction during the intermediate or late stage of coarsening, the shape of the $L1_2$ precipitates in the current $(NiCoFeCr)_{94}Ti_2Al_4$ alloy remains spheroidal and randomly distributed even after aging at 800 °C for 503 h (Figure 4.1d), indicating a low *L* value. In fact, we can quantitatively estimate the *L* value for $(NiCoFeCr)_{94}Ti_2Al_4$ according to Eq. 4.1. Lattice constants of the $L1_2$ precipitates and fcc-matrix are $a_p = 0.3601$ nm and $a_m = 0.3590$ nm, respectively, which gives $\varepsilon = 0.0031$. Inserting this value, together with $C_{44} = 124$ GPa [132], $\sigma = 0.091$ J/m^2 [35] (from Nimonic PE16 superalloy), and *r* = 35 nm (aged at 800 °C for 503 h) into Eq. 4.1, we have *L* = 0.45. Even at this high annealing temperature and aged for such a long time, we still only get *L* of the order of 10^{-1}, which is much less than the critical value of 5.6 for the shape transition, suggesting that the shape of precipitates is mainly controlled by the interfacial energy term under which a 4-fold symmetry is favored. It should be noted that Seidman and coworkers have previously studied Al-Sc [37] and Ni-Cr-Al alloys [133] and also demonstrated that coherent particles with 4-fold symmetry are indeed favored when $L < 5.6$. Based on the first-principles calculations, the exact equilibrium shape of the γ′ (Ni_3Al) precipitates is a Great Rhombicuboctahedron which is approximately spheroidal with 6 {100}, 12 {110} and 8 {111} facets [134]. In the current $(NiCoFeCr)_{94}Ti_2Al_4$ alloy, the morphology of precipitates shown in Figure 4.2d agrees with the [001] projection of a Great Rhombicuboctahedron [134], i.e., having a 4-fold symmetry.

4.3.2 Evolution of precipitates

The classic LSW model [41, 42] for Ostwald ripening was developed initially for ideal dilute binary systems, then extended to multicomponent systems by Philippe and Voorhees (PV) [135]. According to the PV model, the coarsening of precipitates in a multicomponent alloy also

follows a similar power-law relationship, namely, the precipitate size increases with the aging time raised to a 1/3 power, but the coarsening rate constant is more complicated [135].

To apply the PV model to the current $(NiCoFeCr)_{94}Ti_2Al_4$ alloy, let us first consider its chemical constituents. The baseline of the alloy is fcc-NiCoFeCr, which can be treated essentially as a Ni-based alloy, since Ni is the only element with an fcc structure in the alloy. In addition, the lattice constant of NiCoFeCr (0.3572 nm) is very close to that of Ni (0.3517 nm) [25]. Therefore, it seems reasonable to consider $(NiCoFeCr)_{94}Ti_2Al_4$ as a Ni-based pseudo ternary Ni-Ti-Al alloy. In such case, the PV model for steady-state coarsening in ternary alloys is readily applicable to describe the coarsening behavior of $L1_2$ precipitates in $(NiCoFeCr)_{94}Ti_2Al_4$ via the following equations [136-139]:

$$d^3(t) - d^3(t_0) = K(t - t_0) \tag{4.2}$$

$$n_v(t)^{-1} - n_v(t_0)^{-1} = 4.74\frac{K}{\phi_{eq}}(t - t_0) \tag{4.3}$$

where K is the coarsening rate constant, $d(t_0)$, $n_v(t_0)$ are the average size and number density of precipitates at time t_0, respectively, and t_0 refers to the time at the onset of coarsening.

It is evident that, in Figure 4.5, while $\phi(t)$ remains virtually constant, $n_v(t)$ decreases but $d(t)$ increases with increasing time, suggesting that the $(NiCoFeCr)_{94}Ti_2Al_4$ alloy is indeed in the coarsening stage. Using linear regression analysis, the time exponents for $n_v(t)$ and $d(t)$ are determined to be -0.82 ± 0.03 and 0.30 ± 0.01, respectively, which are close to the predicted values of -1 (Eq. 4.3) and 1/3 (Eq. 4.2) by the PV model. The slight discrepancy may be caused by the fact that, in principle, steady state cannot be reached within a limited duration of time [140-142]. For instance, Seidman *et al*. [137] estimated that the aging time required to reach steady-state coarsening in Ni-based Ni-Cr-Al alloys at 600 °C would be about 10^6 h (≈ 114 years)!

4.3.3 Activation energy and coarsening rate constant

Coarsening of $L1_2$ precipitates in the present $(NiCoFeCr)_{94}Ti_2Al_4$ alloy can be analyzed using the power-law relationship in Eq. 4.2. Graph of the average precipitate size ($d^3(t)$) as a function of the aging time (t) at various temperatures is shown in Figure 4.7, from which the coarsening rate constants (K) are determined from the slopes of the linear regression lines. It is evident that coarsening rate increases with the aging temperature, indicating a diffusion-controlled process in accordance with the PV model.

For a diffusion-controlled process, the element with the slowest diffusivity in the $(NiCoFeCr)_{94}Ti_2Al_4$ alloy, in principle, limits the coarsening kinetics. Considering p is the slowest diffusing (rate-limiting) species, the coarsening rate constant, K, is given by [135, 143]:

$$K \approx \frac{64 V_m^{\beta} \sigma D_p \overline{C}_p^{\alpha}}{9RT(\overline{C}_p^{\beta} - \overline{C}_p^{\alpha})^2} \tag{4.4}$$

where α and β denote the fcc-matrix and $L1_2$ precipitate, respectively, V_m^{β} is the molar volume of the precipitate, σ is the precipitate/matrix interfacial energy, $\overline{C}_p^{\alpha}$ and $\overline{C}_p^{\beta}$ are the equilibrium composition (in mole fraction) of the element p in the matrix and precipitates, respectively, R is the gas constant, and T is the absolute temperature. D_p in the equation is the diffusion coefficient of the element p in the matrix which can be expressed by the Arrhenius equation: $D_p = D_{p,0} \exp(-Q_p / RT)$, where $D_{p,0}$ is a pre-exponential factor and Q_p is the activation energy for diffusion. Substituting the expression of D_p into Eq. 4.4 yields

$$K \approx \frac{64 V_m^{\beta} \sigma D_{p,0} \overline{C}_p^{\alpha}}{9RT(\overline{C}_p^{\beta} - \overline{C}_p^{\alpha})^2} \exp\left(-\frac{Q_p}{RT}\right) \tag{4.5}$$

As V_m^{β}, σ, $\overline{C}_p^{\alpha}$ and $\overline{C}_p^{\beta}$ are all weakly temperature-dependent, the value of Q_p can be evaluated

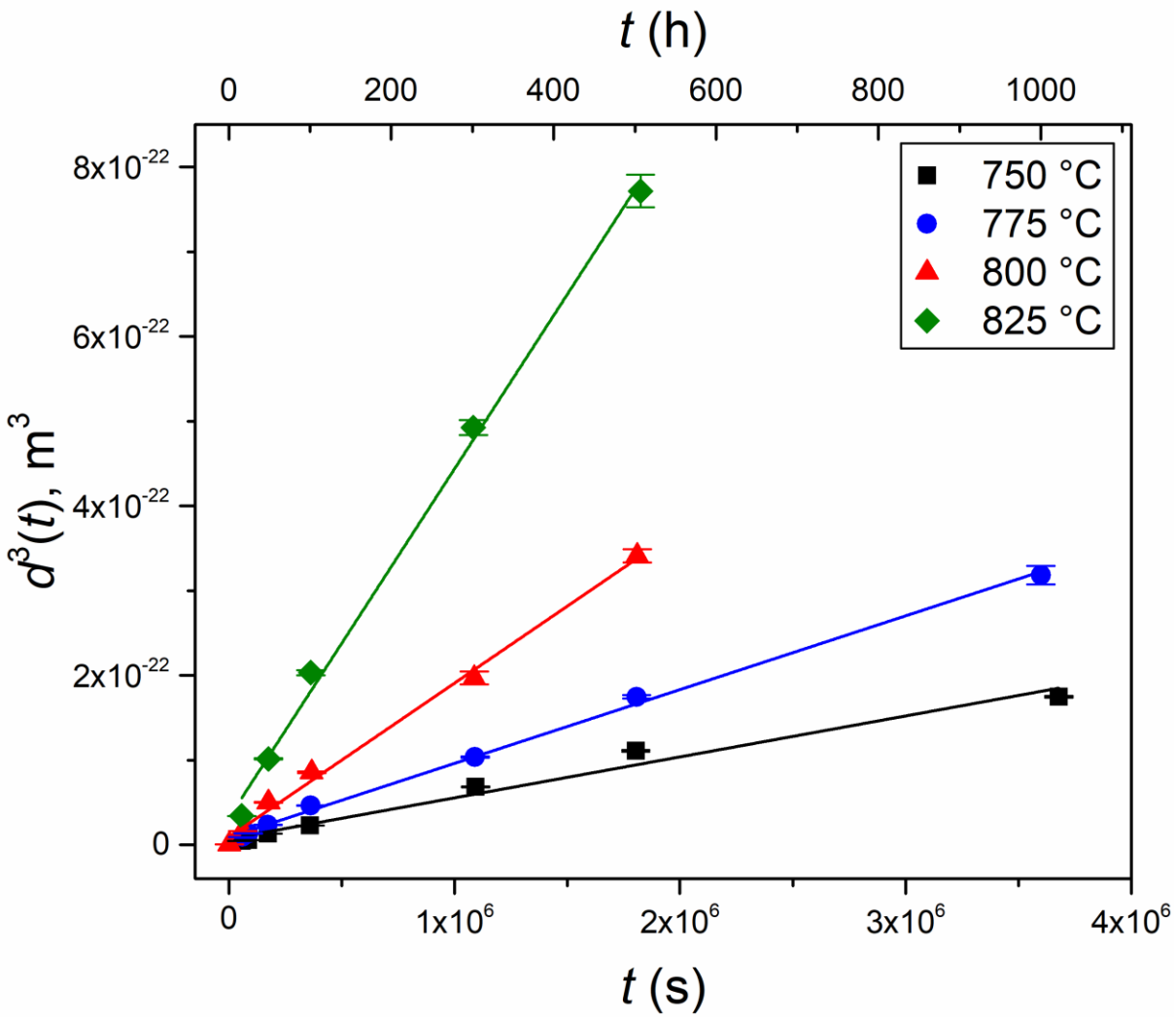

Figure 4.7 Plot of average precipitate size ($d^3(t)$) versus aging time (t) for the $(NiCoFeCr)_{94}Ti_2Al_4$ alloy aged at temperatures between 750 and 825 °C. Solid lines are linear fits of the experimental data (black line: 750 °C, blue line: 775 °C, red line: 800 °C, green line: 825 °C).

directly from the slope of an Arrhenius plot of $\ln(KT)$ versus $1/T$, as shown in Figure 4.8, from which the activation energy is calculated to be 276 kJ/mol. This value can be further compared with the activation energies reported for other Ni-based alloys; they are summarized in Table 4.1. It is readily observed in Table 4.1 that the activation energy for precipitate coarsening in the current HEA system is in good agreement with those (257-285 kJ/mol) reported in many Ni-based alloys, e.g., Ni-13.5Al [114], Ni-10.5Ti [116], Ni-14.7Cr-5.2Al [113], Ni-21.7Co-13.4Al [118], Ni-6.5Ti-4.5Al [119], and some superalloys [122, 147-151].

During the coarsening of the $L1_2$-Ni_3(Al, Ti), the controlling diffusing species can be either Ni, Al, or Ti. Since the measured activation energy is close to that for the diffusion of either Al in Ni (268 kJ/mol) or Ti in Ni (275 kJ/mol), it is inferred that Al or/and Ti can be the controlling diffusing species. Furthermore, both Al and Ti atoms are larger (r_{Al} ~ 0.143 nm, r_{Ti} ~ 0.147 nm [69]) than Ni (r_{Ni} ~ 0.124 nm [69]), from the diffusion point of view, they are more

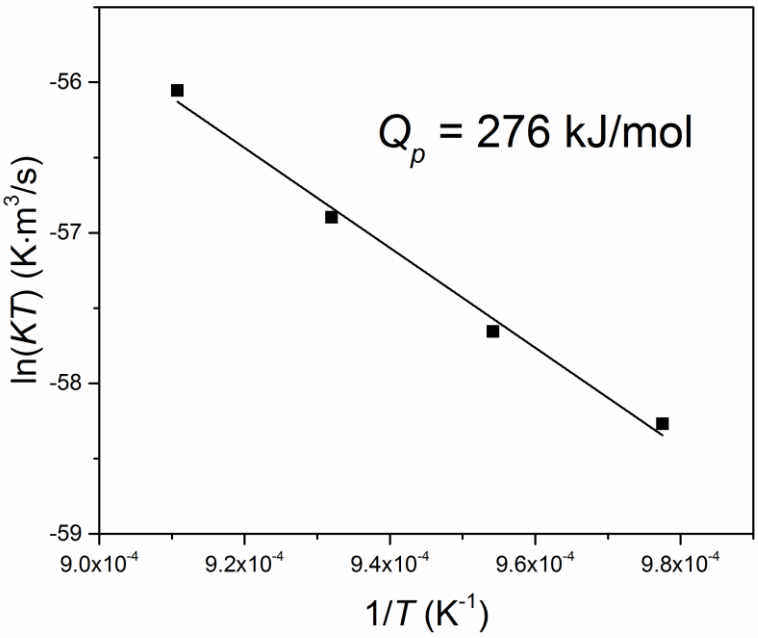

Figure 4.8 Arrhenius plot of the coarsening rate constant ($\ln(KT)$) as a function of the reciprocal aging temperature ($1/T$).

Table 4.1 Activation energies for diffusion in various Ni-based alloys.

Alloy	Method of measurements	*Q* (kJ/mol)	References
Ni in $(NiCoFeCr)_{92}Al_8$	Diffusion couple	227	[144]
Ti in Ni	Diffusion couple	275	[145]
Al in Ni	Diffusion couple	268	[146]
Ni-13.5Al	Precipitate coarsening	270	[114]
Ni-10.5Ti	Precipitate coarsening	283	[116]
Ni-14.7Cr-5.2Al	Precipitate coarsening	274	[113]
Ni-21.7Co-13.4Al	Precipitate coarsening	265	[118]
Ni-6.5Ti-4.5Al	Precipitate coarsening	285	[119]
Inconel 738	Precipitate coarsening	269	[147]
Inconel 939	Precipitate coarsening	266	[122]
CMSX-2	Precipitate coarsening	260	[148]
CMSX-4	Precipitate coarsening	272	[149]
Udimet 700	Precipitate coarsening	270	[150]
Nimonic 80A	Precipitate coarsening	274	[122]
Nimonic 90	Precipitate coarsening	257	[122]
Nimonic 105	Precipitate coarsening	264	[122]
Nimonic PE16	Precipitate coarsening	280	[151]
$(NiCoFeCr)_{94}Ti_2Al_4$	Precipitate coarsening	276	Present work

likely slower diffusion species. Therefore, it is reasonably to conclude that the coarsening of $L1_2$ precipitates in $(NiCoFeCr)_{94}Ti_2Al_4$ is controlled by the diffusion of Al or/and Ti in the alloy matrix.

For the coarsening rate constant (*K*) in Eq. 4.2, it was also deduced and compared with those reported in a number of Ni-based alloys. These data are summarized in Table 4.2 and also plotted as a function of aging temperature in Figure 4.9. It is evident in Fig. 4.9a that *K* increases with the aging temperature in all alloys. It is also noted that the HEA exhibits the lowest *K* value and it increases in a much slower fashion with the aging time than that for other Ni-based alloys. For easy discussion, Figure 4.9b is an enlargement of the rectangular area outlined in Figure 4.9a, which clearly reveals that the *K* value, in a descending magnitude, follows the order of simple Ni-based binary alloys, Ni-based ternary alloys, Ni-based superalloys, and $(NiCoFeCr)_{94}Ti_2Al_4$. It is of interest to point out that precipitate coarsening in the HEA is even slower than some of Ni-based alloys containing refractory elements (such as Mo, Ta, W and Re) which are deliberately added to retard precipitate coarsening [133]. This result clearly demonstrates the excellent thermal stability of the $L1_2$ precipitates in the current HEA.

As indicated in both Table 4.2 and Figure 4.9, precipitate coarsening rate in the HEA is one to two orders of magnitude less than that of other Ni-based alloys. According to Eq. 4.4, *K* is a function of $V_m^\beta, \sigma, D_p, \overline{C}_p^\alpha$ and $\overline{C}_p^\beta$. In view of the small difference (~ 3%) in molar volume between the simple Ni_3Al ($a = 0.3564$ nm [153]) and $Ni_3(Al, Ti)$ ($a = 0.3601$ nm) in the current HEA, and the slight variations of $\overline{C}_p^\alpha$ and $\overline{C}_p^\beta$ resulting from multi-principal alloying additions, the lower coarsening rate in the HEA is probably caused by either a lower precipitate/matrix interfacial energy or a smaller diffusion coefficient, or both. Although the interfacial energy of the HEA is not available, even a lower diffusivity of alloying elements alone can contribute to

Table 4.2 Aging temperature (T), precipitation volume fraction (ϕ), and the coarsening rate constant (K) for various Ni-based alloys.

Alloy	T (°C)	ϕ (%)	K (m^3/s)	References
Ni-13.6Al	600	-	1.00×10^{-29}	[115]
	725	-	1.13×10^{-27}	
	775	-	4.64×10^{-27}	
	800	-	9.25×10^{-27}	
	825	-	2.30×10^{-26}	
Ni-12Ti	550	-	5.93×10^{-31}	[128]
	650	-	1.47×10^{-29}	
	750	-	2.17×10^{-27}	
Ni-17.6Cr-9.7Al	750	40.0	4.92×10^{-28}	[126]
	800	35.0	3.41×10^{-27}	
	850	32.0	1.46×10^{-26}	
Ni-21.7Co-13.4Al	700	31.0	8.86×10^{-29}	[118]
	750	32.0	8.32×10^{-28}	
	800	23.0	2.12×10^{-27}	
Ni-6.5Ti-4.5Al	610	20.0	4.60×10^{-30}	[119]
	752	11.6	1.06×10^{-27}	
	860	6.6	1.72×10^{-26}	
Nimonic 105	750	-	3.33×10^{-28}	[122]
	810	-	2.67×10^{-27}	
	870	-	8.22×10^{-27}	
	930	-	3.33×10^{-26}	
Inconel 939	750	-	2.67×10^{-28}	[122]
	810	-	1.67×10^{-27}	
	870	-	4.22×10^{-27}	
	930	-	2.44×10^{-26}	
Nimonic PE16	670	12.9	3.37×10^{-30}	[152]
	750	10.8	1.38×10^{-28}	
	800	8.2	7.51×10^{-28}	
	824	6.2	1.35×10^{-27}	
	840	4.3	2.77×10^{-27}	
CMSX-4	850	-	2.15×10^{-27}	[149]
	900	-	6.86×10^{-27}	
	925	-	1.40×10^{-26}	
	950	-	2.21×10^{-26}	
$(NiCoFeCr)_{94}Ti_2Al_4$	750	25.5	4.83×10^{-29}	Present work
	775	17.5	8.71×10^{-29}	
	800	12.7	1.82×10^{-28}	
	825	10.1	4.12×10^{-28}	

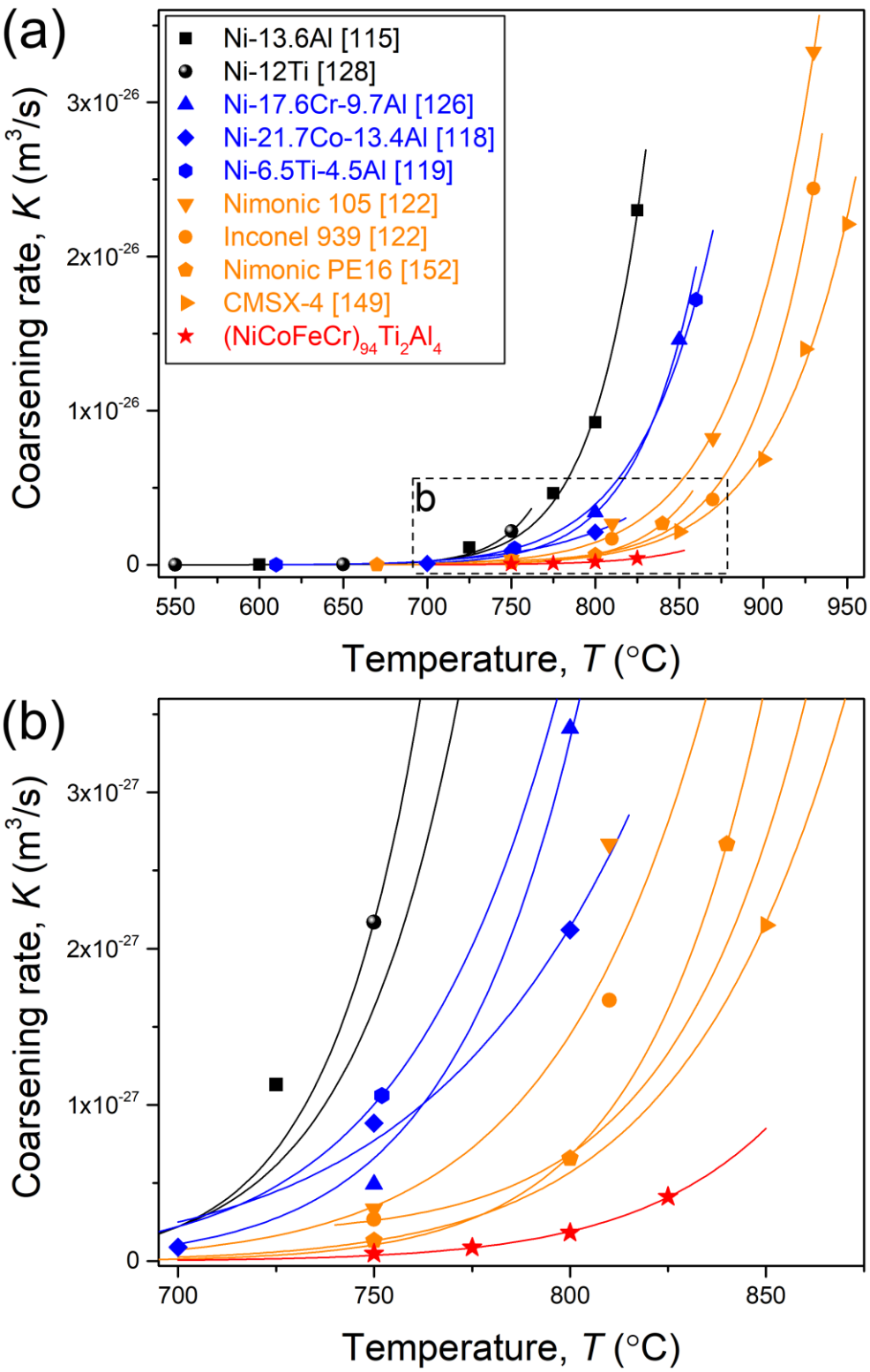

Figure 4.9 (a) Coarsening rates for the $(NiCoFeCr)_{94}Ti_2Al_4$ HEA and a number of Ni-based alloys as a function of aging temperature; (b) an enlarged view of the rectangular frame in (a). Each set of data is fitted using Eq. 4.5.

the slower coarsening in the HEA. This, again, indirectly supports the general notion that diffusion is relatively sluggish in HEAs [8].

4.3.4 Strengthening mechanism

It is shown in Figure 4.6 that aging curves exhibit remarkable hardness increments resulting from the dispersion of $L1_2$ precipitates. Precipitation strengthening, in principle, is governed by either precipitate shearing or Orowan dislocation bypass mechanism. Shearing occurs when precipitates are relatively small and coherent, while Orowan bypass of dislocations dominates when precipitates are sufficiently large. For Orowan bypass mechanism, the increase in the critical resolved shear stress, $\Delta\tau$, can be expressed as [44]:

$$\Delta\tau = \frac{0.4Gb}{\pi\sqrt{1-\nu}} \frac{\ln(\bar{d}/b)}{\lambda} \tag{4.6}$$

where G = 78.5 GPa [29] is the shear modulus of the matrix, $b = \sqrt{2}/2 \times a_m = 0.254$ nm is the Burgers vector, ν = 0.31 is the Poisson's ratio [29], $\bar{d} = \sqrt{2/3} \cdot d$ is the average precipitate diameter on the slip planes, and $\lambda = \bar{d}(\sqrt{(\pi/4\phi)} - 1)$ is the average edge-to-edge interparticle spacing. Insert relevant data into the equation, calculations show that the Orowan mechanism becomes active only at a fairly large particle size (d > 200 nm), which suggests that the mechanism is unlikely to activate in the current $(NiCoFeCr)_{94}Ti_2Al_4$ alloy. Therefore, we only pay attention to the precipitate shearing mechanism.

In Ni-based superalloys, shearing of ordered particles is controlled by anti-phase-boundary-coupled dislocation pairs, i.e., order strengthening [33]. For small particles, dislocation pairs cutting through precipitates are usually weakly coupled, and the shear stress increment required for dislocation movement is given by [44]

$$\Delta\tau = \left(\frac{\gamma_{APB}}{2b}\right)\left[\left(\frac{2\gamma_{APB}d\phi}{\pi\Gamma}\right)^{1/2} - \phi\right] \tag{4.7}$$

where $\gamma_{APB} = 0.3$ J/m^2 (taken from Ni-based superalloys [45]) is the anti-phase boundary energy of the precipitates, and Γ is the dislocation line tension which can be estimated by $\Gamma = Gb^2/2$ [44]. For large particles, on the other hand, shearing of precipitates occurs by strongly coupled dislocation pairs, and the cutting stress or shear stress increment is [154]

$$\Delta\tau = \frac{1}{2}\left(\frac{Gb}{d}\right)\phi^{1/2}0.72w\left(\frac{\pi d\gamma_{APB}}{wGb^2} - 1\right)^{1/2} \tag{4.8}$$

where w is a constant describing the elastic repulsion between the strongly coupled dislocation pairs, which is approximately equal to 1.

The increase in shear stress ($\Delta\tau$) can be readily converted to hardness increment (ΔH) via the well-known equation:

$$\Delta H = \alpha M \Delta\tau \tag{4.9}$$

where α = 3 is the Tabor factor, and M = 3.06 is the Taylor factor for polycrystalline fcc-materials [73]. Subsequently, the calculated and measured hardness increments due to precipitation as a function of the average precipitate size at different aging temperatures are plotted in Figure 4.10. It is apparent that theoretical predictions and experimental measurements agree quite well, affirming that the cutting of precipitates by weakly and strongly-coupled dislocation pairs are the dominant mechanisms in the current $(NiCoFeCr)_{94}Ti_2Al_4$ alloy. Furthermore, it is noted that the hardness initially increases, as described by the weak-coupling mechanism ($\Delta H \propto d^{1/2}$ in Eq. 4.7), reaches a peak and, then, decreases with growing precipitate size according to the strong-coupling mechanism ($\Delta H \propto d^{-1/2}$ in Eq. 4.8). Optimal strengthening takes place at the crossover of the two mechanisms, that is, at d = 22-25 nm in the current HEA

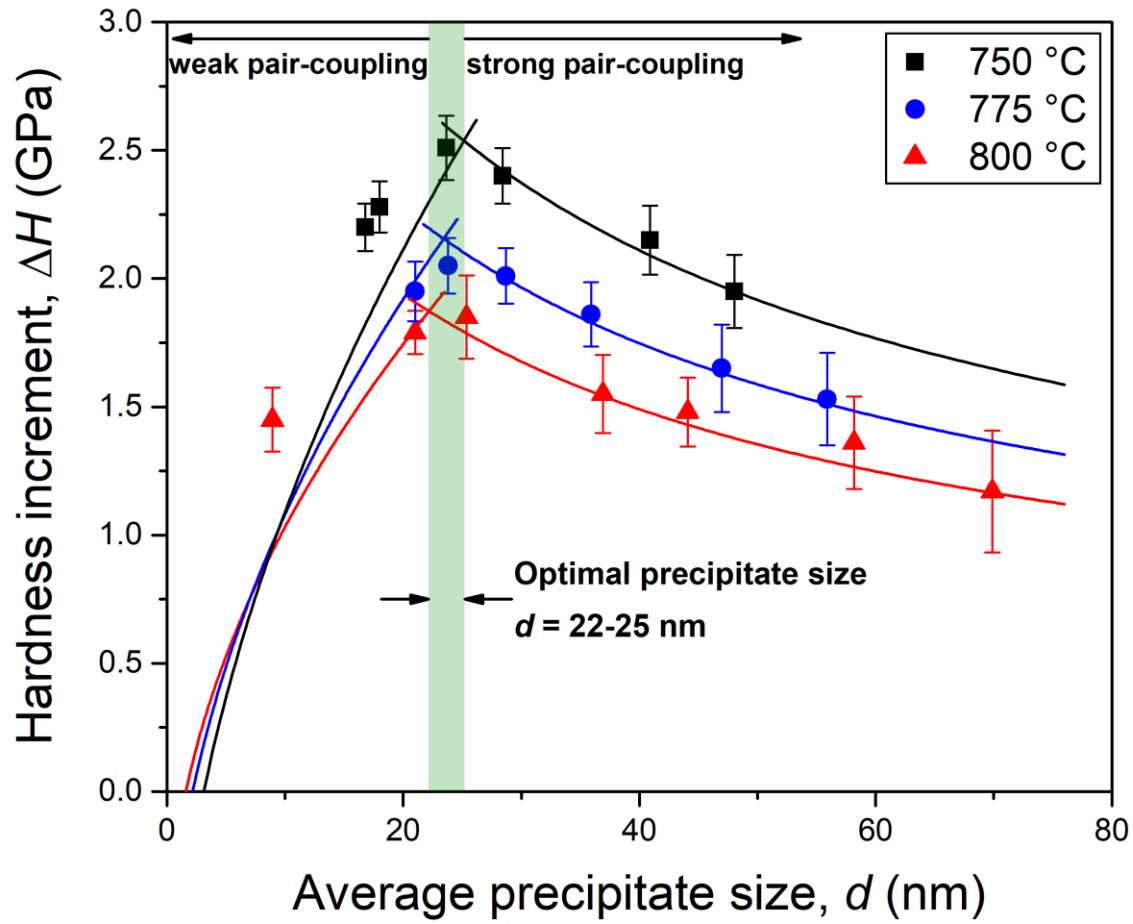

Figure 4.10 Hardness increment (ΔH) as a function of average precipitate size (d) for the $(NiCoFeCr)_{94}Ti_2Al_4$ alloy aged at temperatures between 750 and 800 °C. The experimental datum points are obtained from nanoindentation hardness measurements, and the solid lines show the theoretical calculations.

aged at 750-800 °C. This result is in good agreement with that reported before in Ref. [29].

4.4 Summary

In this chapter, I systematically examined the coarsening of coherent precipitates in an fcc-$(NiCoFeCr)_{94}Ti_2Al_4$ high-entropy alloy (HEA) between 750 and 825 °C and its resultant strengthening effect. Several key observations/conclusions are summarized as follows.

1. Coherent $L1_2$ precipitates formed in fcc-$(NiCoFeCr)_{94}Ti_2Al_4$ appear to be spheroidal and relatively uniformly distributed. These precipitates remain spheroid in shape even after aging at 800 °C for 503 h, indicating a relatively low driving force for coarsening (i.e., a low *L* parameter).

2. Precipitate size distributions are not self-similar with respect to the aging time, suggesting that coarsening does not exactly follow the simple Lifshitz-Slyozov-Wagner theory. Instead, the results appear to fit fairly well with the Lifshitz-Slyozov Encounter Modified model, especially after prolonged aging, indicating particle coalescence in the late stage of coarsening.

3. The current $(NiCoFeCr)_{94}Ti_2Al_4$ can be treated as a pseudo ternary Ni-Ti-Al alloy. By applying the precipitate coarsening model for ternary alloy systems, coarsening kinetics in the alloy has been analyzed. The temporal exponents for average size and number density of precipitates are determined to be 0.30 ± 0.01 and -0.82 ± 0.03, respectively; these values are in reasonable accord with the predictions of the PV model for particle coarsening in ternary alloys.

4. The activation energy for precipitate coarsening is estimated to be 276 kJ/mol, which compares favorably with that for the diffusion of Al or Ti in Ni-based alloys. It is higher than the activation energy for Ni diffusion in the NiCoFeCr-based HEA (227 kJ/mol), suggesting that precipitate coarsening is probably controlled by the diffusion of either Al or Ti, or both, in the

fcc-NiCoFeCr matrix.

5. Resulting from sluggish diffusion, precipitate coarsening rate in the $(NiCoFeCr)_{94}Ti_2Al_4$ alloy is one to two orders of magnitude lower than that in many traditional Ni-based alloys. The slow diffusion contributes to the good thermal stability of the $L1_2$ precipitates.

6. Strengthening observed in the current HEA can be successfully described by the mechanism of precipitate shearing by either weakly or strongly coupled partial-dislocation pairs, depending on the precipitate size, and the optimal precipitate size is about 22-25 nm.

7. The good thermal stability of the $L1_2$ precipitates implies that the current fcc-HEA may have potential for structural applications at elevated temperatures.

Chapter 5. Tribological behavior of an amorphous $Zr_{20}Ti_{20}Cu_{20}Ni_{20}Be_{20}$ high-entropy alloy studied using a nanoscratch technique

In this chapter, we conducted systematic nanoscratch study on an amorphous $Zr_{20}Ti_{20}Cu_{20}Ni_{20}Be_{20}$ alloy. The coefficient of friction (COF) and wear resistance were measured, and scratched morphology was examined using both scanning and transmission electron microscopes. Also, the friction and wear mechanisms were analyzed and discussed.

5.1 Experiments

Ingots with a nominal composition of $Zr_{20}Ti_{20}Cu_{20}Ni_{20}Be_{20}$ (all compositions in this study are in at.%) were prepared by arc-melting mixtures of the constituent elements (purity > 99.9 %) in a Ti-gettered high purity argon atmosphere. The resulting buttons were re-melted several times to ensure chemical homogeneity and subsequently suction cast into a rod form with a diameter of 3 mm and length of 50 mm.

Microstructure of the as-cast samples was examined by employing a PANalytical Empyrean X-ray diffractometer (XRD) with Cu Kα radiation operated at 45 kV and 40 mA. The scanning range and speed were 20°-100°, 2°/min, respectively. Compression tests were performed on an MTS 810 mechanical test machine at a nominal stain rate of 4×10^{-4} s^{-1}. At least 3 samples with a standard aspect ratio of 2 (6 mm in length) were sliced from the ϕ3 mm rod and tested. Vickers hardness (H_v) was measured on a polished sample using a Buehler-Micromet 2100 microhardness tester with an applied load of 300g and a dwell time of 15s. The

mean value of H_v is an average over at least 10 measurements.

Quantitative nanoindentation and nanoscratch tests were conducted at room temperature using a Hysitron TI 900 TriboIndenter equipped with a 2D transducer under a load-control mode, which simultaneously delivers force and displacement data in both the normal and lateral directions. Prior to testing, each sample was mechanically polished using 1 μm diamond paste, followed by a final polishing with 0.05 μm colloidal silica suspension. Indentation measurements were carried out using a Berkovich indenter with a tip radius of 280 nm. Elastic modulus (E) and nanohardness (H_n) were determined from at least 30 indentation measurements made with a 15 μm indented interval, at a loading rate of 1000 μN/s and a peak load of 10000 μN. Various loading rates (10^3-10^6 μN/s) were also used to investigate the rate dependence of hardness.

A 90° cono-spherical diamond indenter with a tip radius of 600 nm was used for nanoscratch tests. Based on the indenter tip geometry, the critical penetration depth for the transition from the spherical to conical shape is calculated to be 176 nm [62], in other words, when the penetration depth is shallower than this critical value, the indenter can be treated as a spherical tip. Before scratching, lateral force calibration (i.e., air-scratch) was conducted to determine the background noise caused by the machine vibration, and the results are shown in Figure 5.1. The lateral force fluctuation during scratching in air is plotted in Figure 5.1a. For clarity, Figure 5.1b, which is an enlargement of the outlined area in Figure 5.1a, reveals that the maximum background noise is approximately 9 μN. Consequently, lateral force fluctuations within 9 μN will be treated as background noise in the present work. Scratch tests were made in either ramping or constant load mode at a sliding speed of 0.5 μm/s over a scratch distance of 8 μm. Under the ramping-load condition, the applied normal load increased linearly from 0 to 4000 μN along the scratch length. For the constant-load scratching, on the other hand, constant

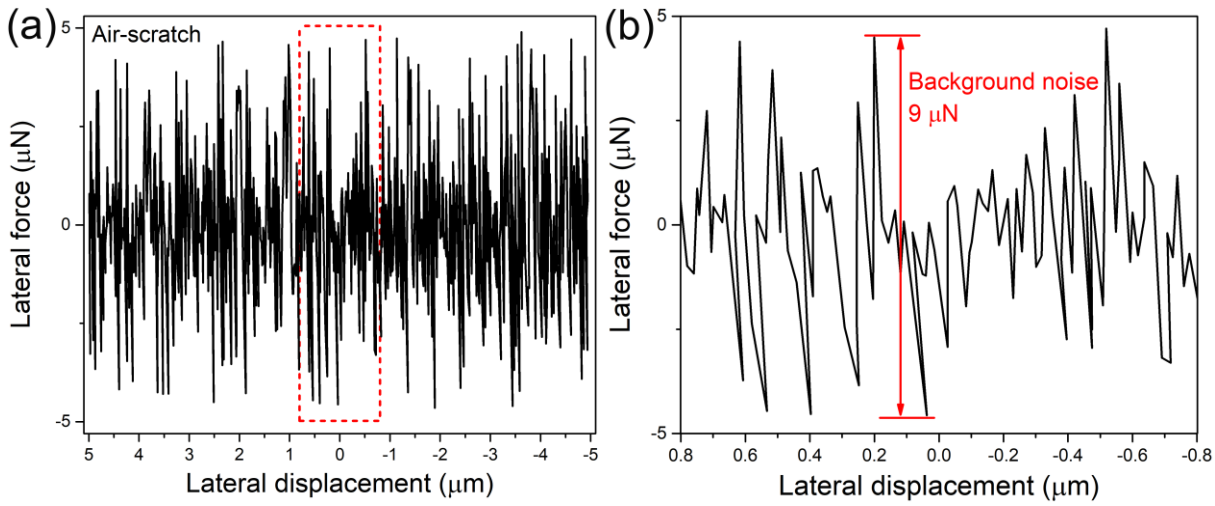

Figure 5.1 Results of lateral force calibration. (a) Lateral force fluctuation during scratching in air. (b) An enlarged view of the red frame section in (a) showing the determination of background noise.

applied normal forces of 500-4000 μN were employed. To investigate scratch rate effect, scratch tests were performed at various sliding speeds (0.01-1 μm/s). At each sliding speed, at least 3 scratches were made at a 50 μm interval.

Surface profiles before and after nanoscratching were measured using the scanning probe microscope (SPM) integrated in the Hysitron TriboIndenter system and a sharp cube corner diamond indenter with a tip radius of 80 nm was applied. Surface roughness of the polished samples was measured to be about 2 nm (rms roughness). Scratch morphologies were observed using a Zeiss Auriga scanning electron microscope (SEM). Subsurface morphology and microstructure underneath the scratched track were examined using a Zeiss Libra 200 MC transmission electron microscopy (TEM). A Zeiss Auriga crossbeam workstation was employed to prepare the TEM lamellae for examining the microstructure underneath the scratched trace produced by a constant normal force of 1500 μN.

5.2 Results

5.2.1 Microstructure and mechanical properties

X-ray diffraction pattern from the as-cast $Zr_{20}Ti_{20}Cu_{20}Ni_{20}Be_{20}$ alloy is presented in Fig. 2a, which shows only a broad diffraction spectrum without any detectable crystalline peak, indicating that the current sample is essentially amorphous without containing any long-range ordered structure.

Typical compressive stress-strain curve and nanoindentation load-displacement curve of the current amorphous alloy are shown in Figures 5.2b and 5.2c. It is readily seen in Figure 5.2b that the sample appears to deform elastically without exhibiting any plasticity prior to a sudden failure at 2360±30 MPa (defined as the yield strength σ_y). The Vickers microhardness (H_v) is measured to be 6.68±0.03 GPa, giving a hardness to strength ratio (H_v/σ_y) of 2.8, which is close to the reported value for many amorphous alloys, i.e., 2.7 [155]. This result also affirms that the current as-cast amorphous sample does not contain major flaws that can lead to premature failure. Elastic modulus (E) and nanohardness (H_n) of the samples were determined to be 135±1 GPa

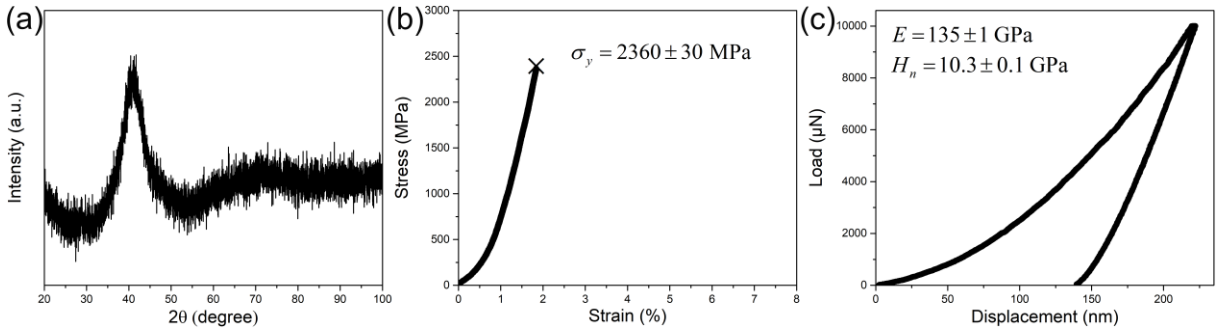

Figure 5.2 (a) XRD pattern, (b) compressive stress-strain curve and (c) load-displacement curve for the as-cast $Zr_{20}Ti_{20}Cu_{20}Ni_{20}Be_{20}$ alloy. × marks sample fracture.

and 10.3±0.1 GPa, respectively, as indicated in Figure 5.2c. The nanohardness (produced at low loads) is noted to be much higher than microhardness (produced at high loads), which has been also reported in many amorphous alloys [156] and attributed to an indentation size effect. For comparison, values of E, σ_y, and H_v obtained from the current *a*-HEA $Zr_{20}Ti_{20}Cu_{20}Ni_{20}Be_{20}$, together with those from some of the Zr-Ti-Cu-Ni-Be-based amorphous alloys, are listed in Table 5.1. It is readily seen in the table that $Zr_{20}Ti_{20}Cu_{20}Ni_{20}Be_{20}$ has a relatively higher modulus, yield strength, and hardness than other Zr-Ti-Cu-Ni-Be amorphous alloys.

5.2.2 Friction behavior

To investigate the friction behavior of the current *a*-HEA, ramping-load (from 0 to 4000 μN) scratch tests were initially carried out and the results are presented in Figure 5.3. The COF (defined as the ratio of the lateral to normal forces during scratching) against applied normal load is shown in Figure 5.3a. The COF apparently exhibits two regions, labeled as I and II in Figure 5.3a. In Region I (normal force < 320 μN), which corresponds to elastic sliding, the COF drops

Table 5.1 Summary of elastic modulus (E), compressive yield strength (σ_y), Vickers microhardness (H_v).

Alloy	E (GPa)	σ_y (GPa)	H_v (GPa)	Ref.
$Zr_{20}Ti_{20}Cu_{20}Ni_{20}Be_{20}$	135	2.36	6.7	Present work
$Zr_{41.2}Ti_{13.8}Cu_{12.5}Ni_{10}Be_{22.5}$ (Vit-1)	97	1.85	5.2	[157, 158]
$Zr_{44}Ti_{11}Cu_{9.8}Ni_{10.2}Be_{25}$ (Vit-1b)	96	1.81	5.3	[159, 160]
$Zr_{46.75}Ti_{8.25}Cu_{7.5}Ni_{10}Be_{27.5}$ (Vit-4)	100	1.83	6.1	[161]
$Ti_{32.8}Zr_{30.2}Cu_9Ni_{5.3}Be_{22.7}$	98	1.83	5.0	[162]
$Ti_{40}Zr_{25}Cu_{12}Ni_3Be_{20}$	93	1.76	4.9	[163]
$Ti_{40}Zr_{25}Cu_9Ni_8Be_{18}$	95	1.72	5.2	[164, 165]
$Ti_{60}Zr_5Cu_9Ni_8Be_{18}$	106	2.12	-	[166]

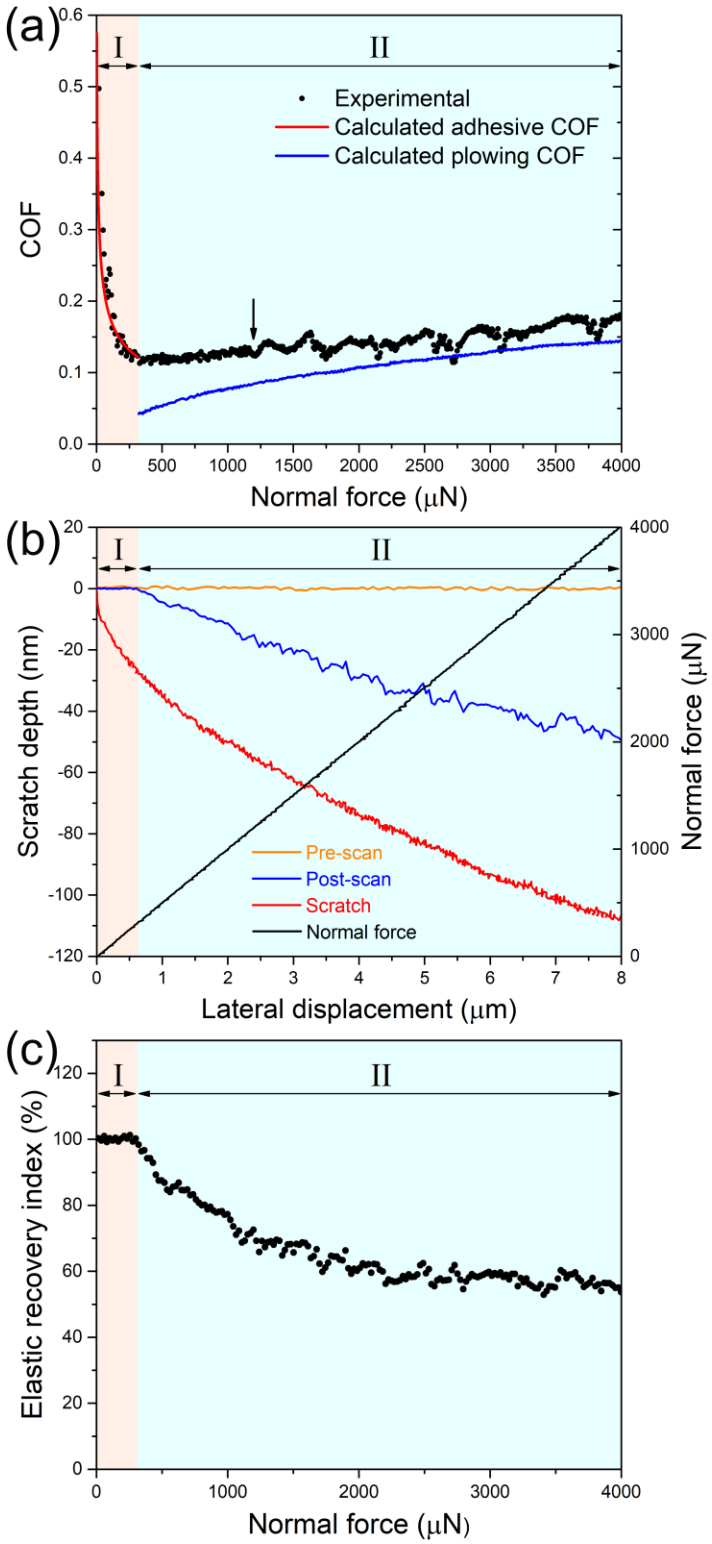

Figure 5.3 (a) The coefficient of friction (COF), (b) surface profile and (c) elastic recovery index during the ramping-load (0-4000 μN) scratch tests. Stage I and II denote elastic and plastic deformation, respectively.

rapidly from ~ 1 to 0.11. In Region II (normal force from 320 to 4000 μN), plastic deformation becomes dominant and the COF gradually increases from 0.11 to 0.18 with increasing normal load. Noted that serration of the curve begins at a normal force of ~ 1200 μN (black arrow in Figure 5.3a), which may be attributed to the formation and propagation of microcracks [60, 167]. We will discuss this later.

To study the surface response of tested sample upon nanoscratch, scratch depth is plotted as a function of lateral displacement in Figure 5.3b, which includes surface profiles before (pre-scan: orange line), during (scratch: red line), and after (post-scan: blue line) scratching. Both the pre-scan and post-scan were conducted with an extremely low normal force along the scratch length in order to provide the scratch depth with high fidelity. For easy discussion, the ramping normal force is also depicted in the figure (black line) for comparison. The small fluctuation of the pre-scan curve indicates a relatively smooth surface prior to scratching. During scratching, the depth monotonically increases with increasing normal force and eventually reaches a maximum value of ~ 110 nm at the final imposed normal force of 4000 μN. Noted that the scratch depth profile is approximately parabolic, despite the linearly applied ramping normal load. The depth difference between the pre-scan and post-scan represents the permanent damage made by the scratch, however, the difference between the scratch and post-scan profiles is a result of elastic recovery. It is particularly noted that, according to the post-scan profile, the initial part (i.e., normal force less than 320 μN) of the scratch path is fully recovered, indicating a purely elastic deformation; this is also revealed in the COF curve shown in Figure 5.3a.

The ability of the *a*-HEA to recover elastically after being scratched can be evaluated by the elastic recovery index, η, defined as $\eta = (h - h_r)/h$, where h is the penetration depth during the scratch and h_r is the residual depth after the scratch. The elastic recovery index as a function

of the applied normal force is plotted in Figure 5.3c. As expected, the elastic recovery index can also be divided into two regions, similar to the results in Figures 5.3a and 5.3b. Obviously, it is 100% in Region I, confirming the elastic deformation. Once the normal force exceeds the critical value (320 μN), η begins to decrease gradually and, then, levels off at around 50%. Similar trend for η was also observed before in some amorphous alloys [60, 168] and HEAs [62].

5.2.3 Scratch morphology

SEM images revealing scratched morphology under the ramping load are presented in Figure 5.4. For comparison, surface scratched under a constant normal load of 1000 μN is also shown in parallel (Figure 5.4a), which indicates a trace essentially unchanged in depth and width throughout the entire scratch process. On the other hand, at the ramping load mode, the scratched groove progressively becomes deeper and wider as the normal force linearly increases from 0 to 4000 μN. Scratch trace was not detectible until the normal force reached ~ 400 μN, suggesting elastic deformation during the initial portion of the scratch and fully agrees with the results in Figure 5.3. As the normal force exceeds the elastic limit, the scratched groove begins to roughen (Figure 5.4b), indicating that brittle fracture rather than ductile plowing dominates in the plastic region. Nonetheless, no significant crack formation is observed around the edges of the groove at the early stage of plastic deformation (Figure 5.4b). At increasing normal force, radial cracks (yellow arrows in Figure 5.4c) begin to form along the banks of the scratched groove. The first radial crack (red arrow in Figure 5.4a) appears at the normal force of ~ 1200 μN, corresponding exactly to the onset of serrations in the COF curve (Figure 5.3a). Further increase of the normal force leads to the presence of several larger radial cracks (yellow arrows in Figure 5.4d) along the groove edges and scale-like cracks (black arrows in Figure 5.4d) on the bottom of the groove.

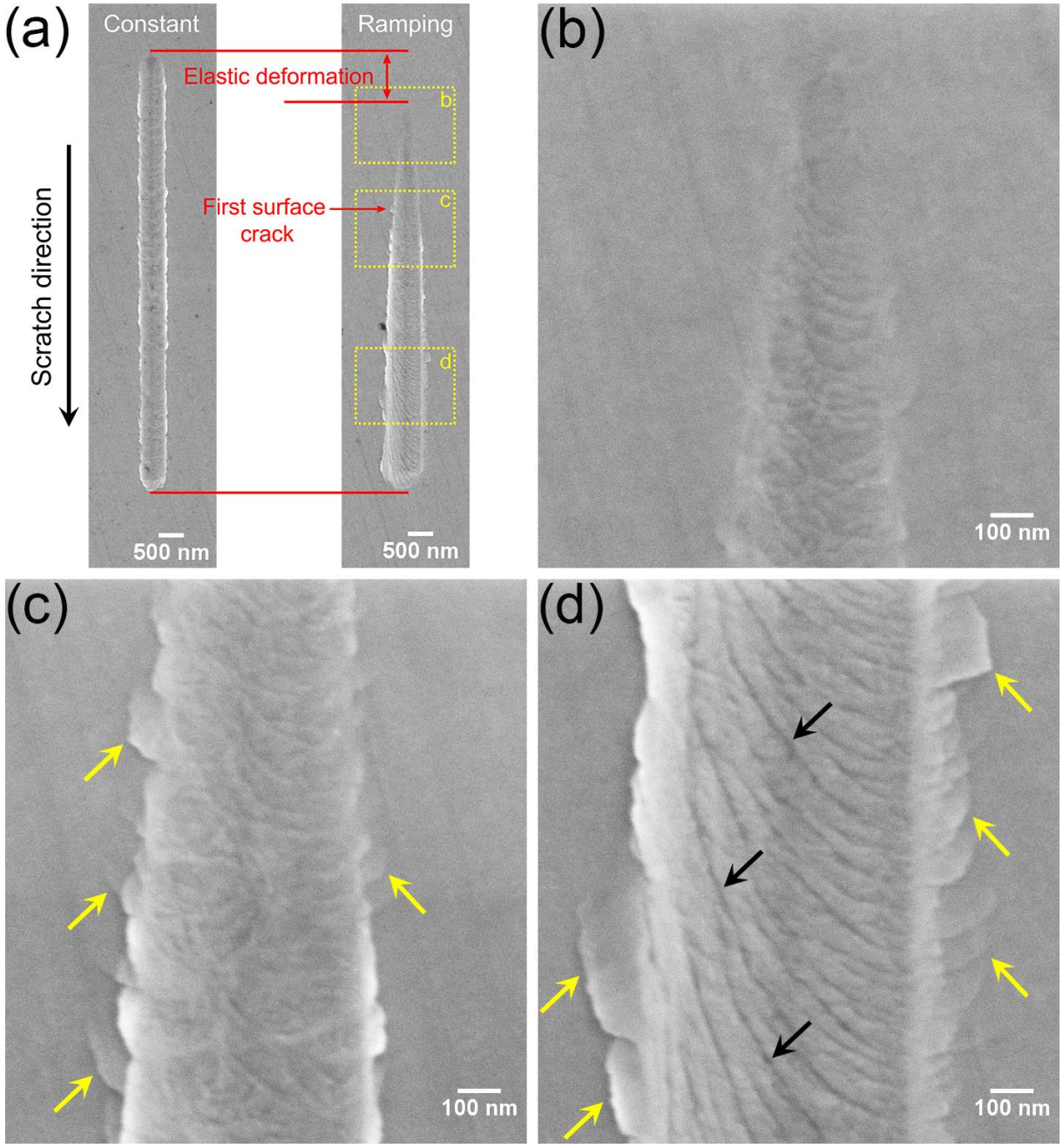

Figure 5.4 (a) SEM micrographs of scratched surface under the ramping load from 0 to 4000 μN. A scratched groove resulting from a constant normal load of 1000 μN is also included for comparison. (b), (c) and (d) are enlargements of areas outlined in (a).

To further examine the nature of the scratch morphology, scratch tests under constant normal loads of 500 μN, 1500 μN, and 4000 μN were conducted, and the resulting scratched grooves, together with their corresponding variations of lateral force during scratching are shown in Figure 5.5. For easy discussion, enlarged views of the outlined regions in Figures 5.5a, 5.5c and 5.5e are presented in Figures 5.5b, 5.5d and 5.5f, respectively. It is readily seen in Figure 5.5b that a constant normal force of 500 μN produces a ~ 270 nm-wide groove with a rugged bottom, reaffirming the brittleness of the *a*-HEA. The amplitude of lateral force fluctuation was measured to be approximately 11 μN, close to the background noise (~ 9 μN), indicating no significant crack formation during scratching. At a normal force of 1500 μN, the groove width and undulation amplitude of lateral force are estimated to be ~ 530 nm and 20-30 μN, respectively, as illustrated in Figure 5.5c. Further detailed examination (Figure 5.5d) shows radial cracks along the banks of the scratched groove, and these cracks lead to the drops in the lateral force. The spacing between the cracks was about 200-300 nm. With normal force increased to 4000 μN (Figure 5.5e), the groove becomes ~ 620 nm wide, and the amplitude of lateral force fluctuation is as large as 100-150 μN. An enlarged view (Figure 5.5f) shows scale-like cracks (black arrows in Figure 5.5f) on the bottom of the groove and radial cracks along the groove edges. It is noted that radial cracks formed along the two sides of the scratched trace is asymmetrical - smaller cracks with narrower spacing (~ 100 nm) on one side, but larger cracks on the other side. The larger radial cracks correspond to the larger drops in the lateral force curve, as indicated by red arrows in Figure 5.5e. This asymmetrical morphology might be attributed to a slight misalignment between the indenter and the sample surface.

To investigate possible phase change as a result of scratching, subsurface morphology and microstructure of the scratched track produced by a constant normal force of 1500 μN were

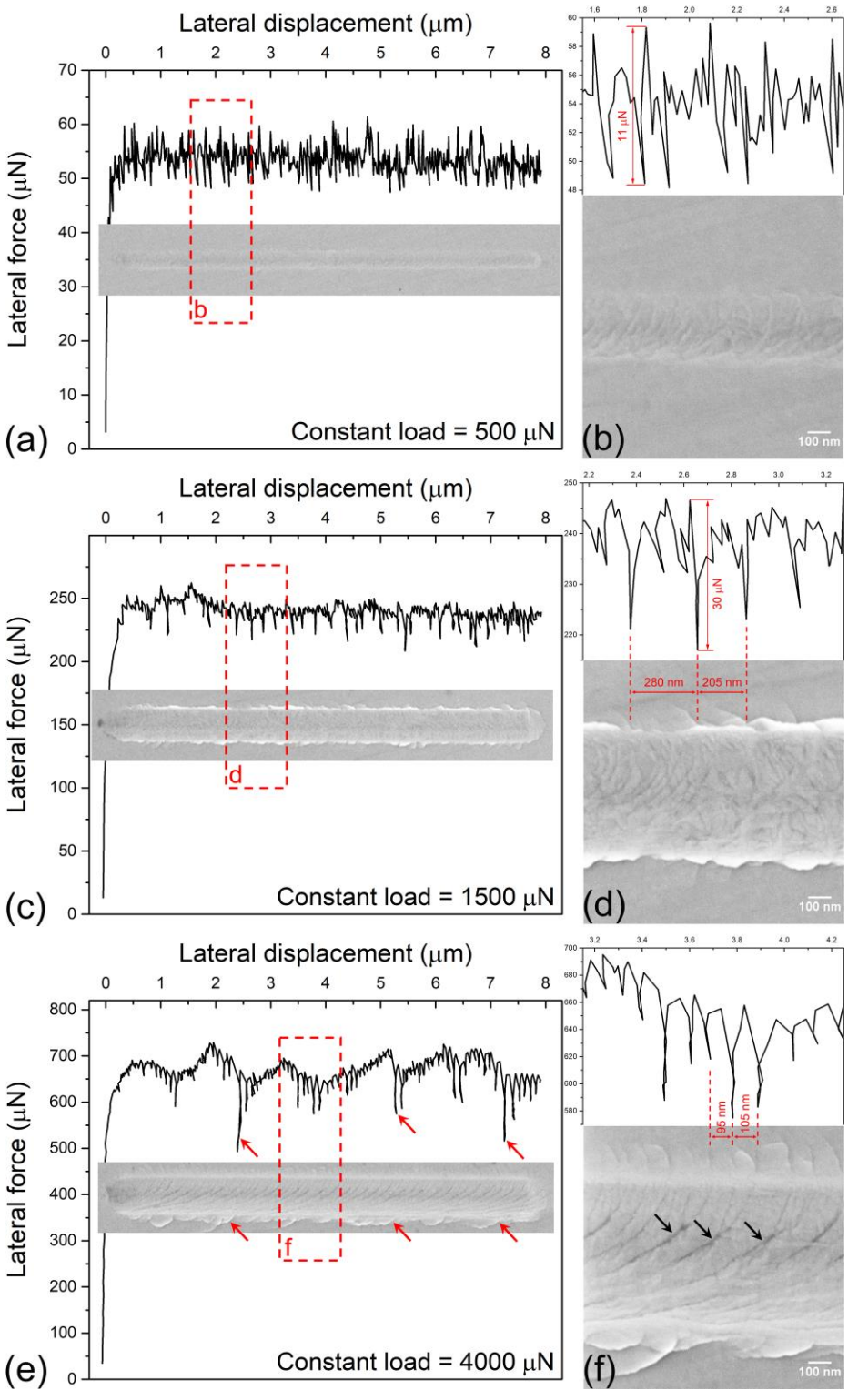

Figure 5.5 SEM micrographs of scratched surface under constant loads of (a) 500 μN, (b) 1500 μN, and (c) 4000 μN, together with the corresponding plots of lateral force as a function of lateral displacement. (b), (d) and (f) are enlargements of the rectangular frames in (a), (c) and (e), respectively.

examined using TEM, and a TEM image is presented in Figure 5.6. An arc-shaped cross-section, as outlined by the dashed lines in Figure 5.6a, is examined. The height of the arc, corresponding to the residual scratch depth, was measured to be ~ 21 nm, agrees well with scratched surface profile shown in Figure 5.3b. The selected area electron diffraction pattern (upper-right inset in Figure 5.6a) taken from the area immediately beneath the scratch surface shows only diffused halo rings without any detectable diffraction spots, suggesting no phase transformation or crystallization has taken place and the sample is still in a fully amorphous state. An enlarged image of the bottom region (outlined by the red rectangular frame in Figure 5.6a) is given in Figure 5.6b. The image shows a rugged surface with many irregular grooves or cracks (red arrows in Figure 5.6b) on the scale of 10 nm or less, confirming brittle fracture during scratching.

5.2.4 Abrasive wear

Abrasive wear is generally viewed as the contact of a single rigid asperity with a soft and

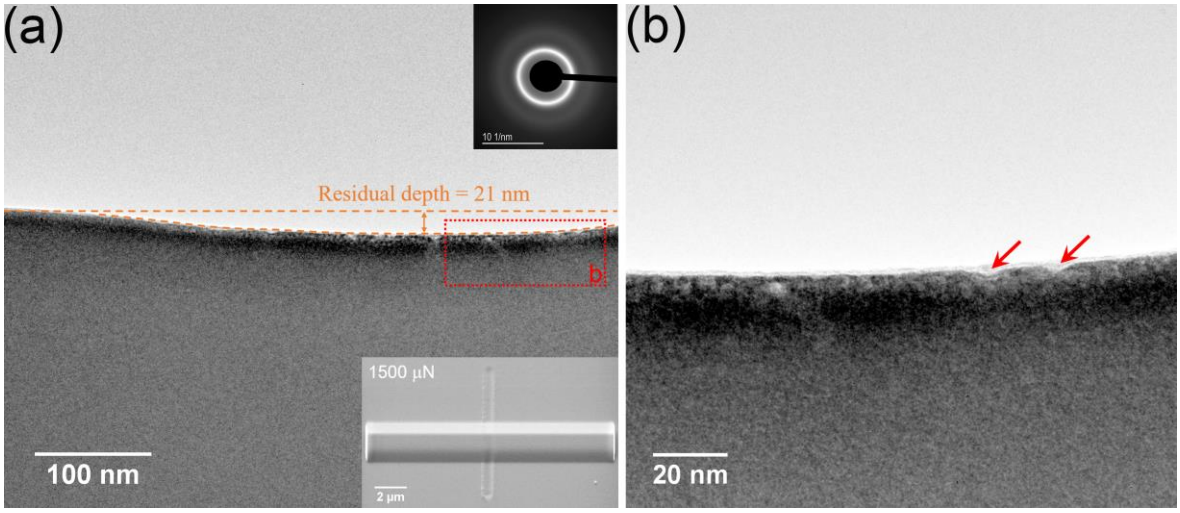

Figure 5.6 (a) Cross-sectional TEM image of the scratched groove resulted from a constant normal force of 1500 μN. The inset at the lower right in (a) illustrates the location of the lift-out TEM lamella, and the upper right inset in (a) shows selected area electron diffraction pattern from the area beneath the scratched surface. (b) An enlarged view of the rectangular frame in (a).

smooth surface, and the wear resistance is quantitatively evaluated by measuring the volume of removed material during scratching. In order to obtain the volume of removal, surface topographies of scratched tracks under constant loads of 500 μN, 1500 μN and 4000 μN were examined and presented in Figure 5.7a, where the dark and bright areas are the scratched groove and pile-ups of materials along the banks of scratch. Cross-sectional profiles of these grooves are presented in Figure 5.7b, in which a schematic illustration (inset) showing pile-ups and groove is also included for easy discussion. It is readily observed in the profiles that the scratched groove becomes wider and deeper with increasing normal force. Under the current condition of constant normal force (F_n), the amount of materials removed (V) is given by the Archard equation [169]:

$$V = K\frac{F_n}{H}x \tag{5.1}$$

where K is a wear constant, H is the hardness, and x is the sliding distance. According to Eq. 5.1, the wear rate (W, defined as $dV/\mathrm{d}x$) can be expressed as:

$$W = \frac{dV}{dx} = \frac{K}{H}F_n \tag{5.2}$$

Thus, the wear rate is expected to linearly increase with the applied normal force. It should be noted that $W = dV/\mathrm{d}x = A_p$, where A_p is the projected area of the tip in the direction of scratching, which can be directly measured from the cross-sectional profiles of scratched tracks (Figure 5.7b). Accordingly, a plot of the wear rate as a function of the normal force is shown in Figure 5.7c. The wear resistance coefficient, defined as $R_W = H/K$, can be evaluated readily from the inverse of the slope of the plot, from which the value of R_W is calculated to be $3.06\times10^{11}\,\mathrm{Pa}$. This value is further compared with the wear resistance measured also by the nanoscratch technique for HEAs [62, 170] and amorphous alloys [61]; these data are plotted as a

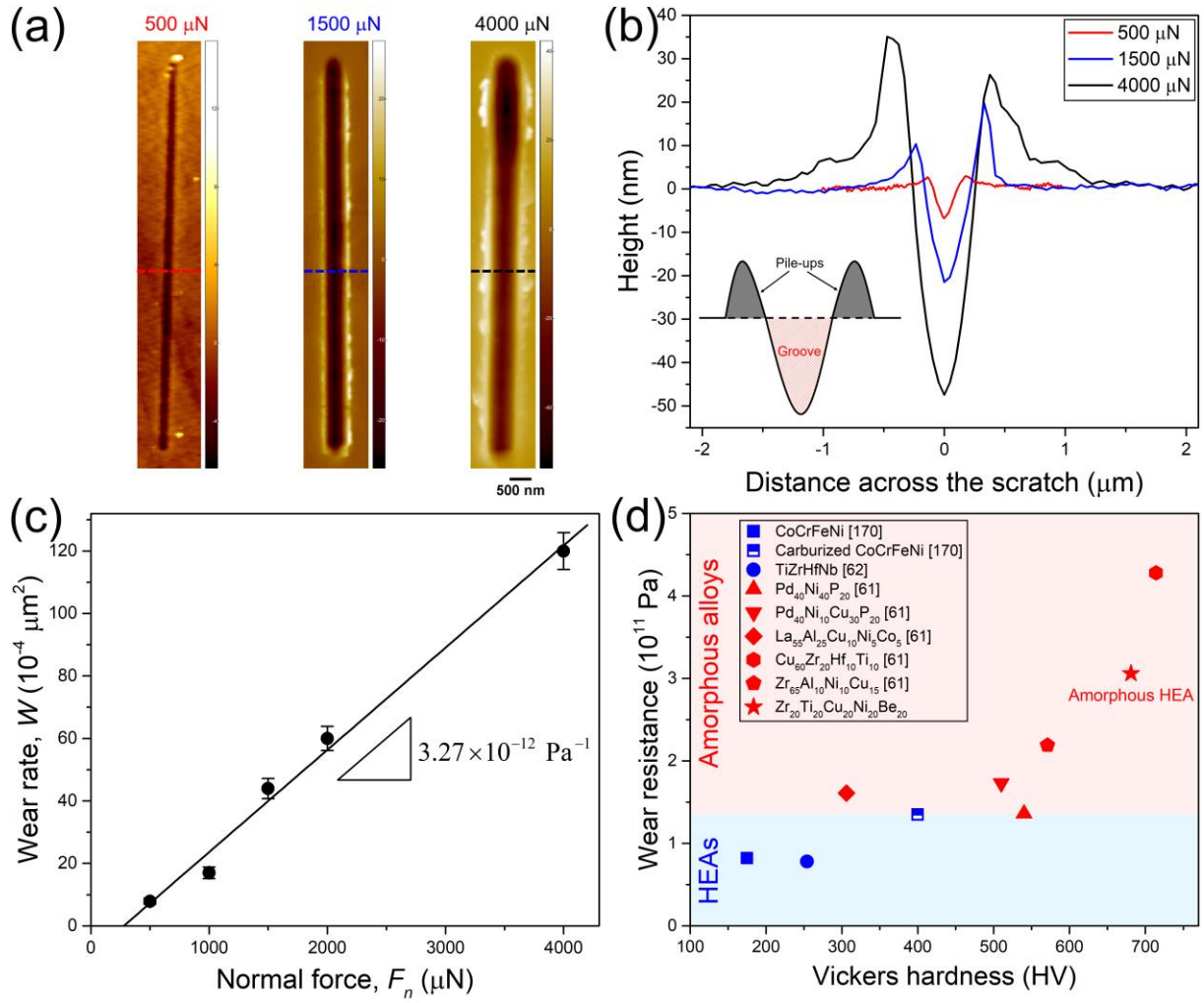

Figure 5.7 (a) Representative SPM images of the scratched surface under constant loads of 500 μN, 1500 μN and 4000 μN, and (b) the corresponding cross-sectional profiles indicated by dashed lines (red: 500 μN; blue: 1500 μN; black: 4000 μN) in (a). The inset in (b) illustrates a sketch of a cross-section during scratching. (c) Wear rate of the amorphous HEA as a function of normal force. (d) Correlation of wear resistance measured by the nanoscratch method with Vickers hardness for HEAs [62, 170], amorphous alloys [61] and the amorphous HEA.

function of Vickers hardness in Figure 5.7d. There is an evident trend that wear resistance generally increases with increasing hardness, consistent with the Archard's relation [169]. It is also noted in Figure 5.7d that the wear resistance of the current *a*-HEA falls in the upper range for most amorphous alloys and is about 3 times higher than that of HEAs. Furthermore, the nanoscratch employed here is actually dry wear which leads to significantly more severe wear compared to real tribological contacts often with lubrication (wear rate ~ 10 nm per hour).

5.2.5 Scratch rate effect

Atoms in amorphous alloys (or metallic glasses) are not only able to flow (an athermal process) but also relax (a thermal process). To examine the effects of scratch rate on the wear behavior of the current *a*-HEA, ramping-load (0-4000 μN) tests at sliding speeds of 0.01 μm/s, 0.1 μm/s and 1 μm/s were performed, and the resulting depth profiles are given in Figure 5.8a. It is readily seen that the scratch depth is insensitive to the sliding speed, implying that the wear resistance is independent of sliding speed, at least within the range of 0.01-1 μm/s. The insignificant rate dependence of wear resistance has also been reported in several other

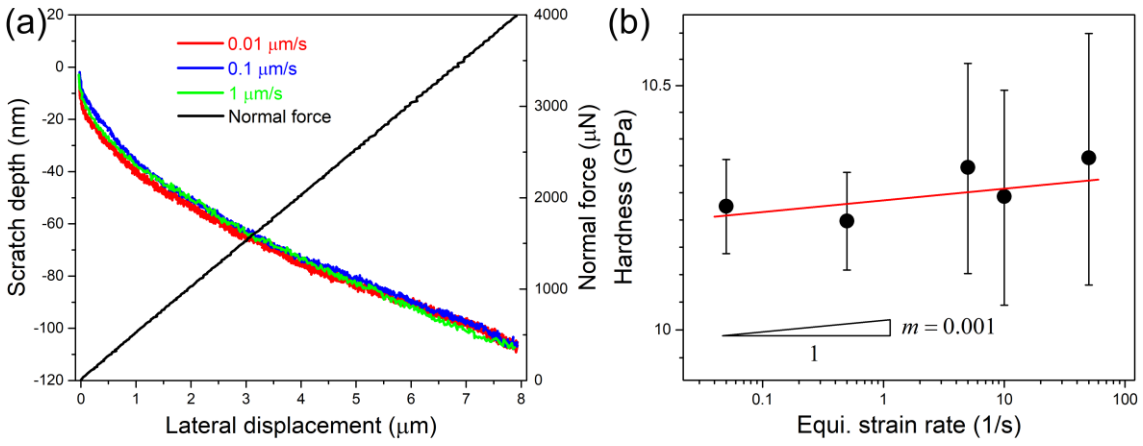

Figure 5.8 (a) Scratch depth profiles at various sliding speed during the ramping-load (0-4000 μN) tests. (b) Determination of strain rate sensitivity of hardness of the studied *a*-HEA.

amorphous alloys [61, 171], which is associated with the fact that these amorphous alloys have a T_g (glass transition temperature) which is far from the room temperature, thus deform heterogeneously and insensitive to strain rate [172]. The measured *m*-value (Figure 5.8b) is only 0.001, indicating a weak strain rate dependence of the present *a*-HEA.

Special efforts were also made to estimate the possible surface temperature increase caused by frictional heating during scratching. For frictional contact between two solid bodies, temperature arise is related to the Peclet number, which describes the ratio of heat source speed to the propagation velocity of heat conduction. The Peclet number is defined as $Pe = va/2D$ [173], where v is the sliding speed, a the contact radius, $D = k/\rho C$ the thermal diffusivity, k the thermal conductivity, ρ the density and C the specific heat. Since the values of k, ρ and C are not available for the present *a*-HEA, the rule-of-mixture method was used in the estimations. Inserting $v = 1$ μm/s (maximum sliding speed), $a = 344$ nm (at the maximum value of $F_n = 4000$ μN), $k = 148$ W/m·K, $\rho = 6138$ Kg/m^3, and $C = 703$ J/Kg·K into the equation, we have $Pe = 5\times10^{-9}$. This extremely low value of the Peclet number, mainly due to the current slow sliding speed (1 μm/s), suggests that the heat source can be treated as quasi-stationary, and the frictional heat has sufficient time to diffuse to its surrounding. In fact, the maximum flash temperature ($\Delta T_{\max}$) rise is [169]

$$\Delta T_{\max} = 0.25\frac{\alpha\pi p_m}{\rho C}\frac{F_n^{1/2}v}{2D(\pi p_m)^{1/2}} \tag{5.3}$$

where α is the COF ($\alpha = 0.18$ at $F_n = 4000$ μN), and $p_m = F_n/(\pi a^2)$ is the mean contact pressure. The value of $\Delta T_{\max}$ is calculated to be only 1.8×10^{-6} K, which is obviously negligible, consistent with the TEM results (Figure 5.6) that no crystallization was observed beneath the

scratched groove.

5.3 Discussion

Friction and wear are two key features in the understanding of tribological behavior of materials. A material with low coefficient of friction and high resistance to wear is usually considered desirable in designing a wear structural component. The fact that the current amorphous $Zr_{20}Ti_{20}Cu_{20}Ni_{20}Be_{20}$ HEA has a low COF and high wear resistance suggests that the alloy may be possibly a good anti-wear material. The good wear resistance is evidently resulted from the high hardness of the alloy, according to the Archard's relation [169]. However, the relatively low COF appears to be intriguing and needs additional attention. Its analysis and discussion are presented in the following.

In Region I, the COF dramatically decreases from ~ 1 to 0.11, as shown in Figure 5.3a. In this region (Figure 5.4), there is only elastic deformation (shearing) and plastic plowing is absent, thus a non-adhesive (assuming that adhesion due to short-range chemical force is negligible) single-asperity (Hertz) model is expected to apply, that is [174],

$$F_f = \tau_s \cdot A_c \tag{5.4}$$

where F_f is the friction force, τ_s is the interfacial shear strength, and A_c is the contact area between the indenter and the sample. Insert $A_c = \pi a^2$ and $a = (3F_n R/4E_r)^{1/3}$ into Eq. 5.4, we have

$$F_f = \tau_s \cdot \pi \cdot (3R/4E_r)^{2/3} \cdot F_n^{\,2/3} \tag{5.5}$$

where R is the tip radius, and E_r is the reduced modulus. Therefore, shearing COF (μ_{sh}) can be straightforwardly deduced from Eq. 5.5 as

$$\mu_{sh} = F_f / F_n = \tau_s \cdot \pi \cdot (3R/4E_r)^{2/3} \cdot F_n^{\,-1/3} \tag{5.6}$$

This equation indicates that COF in Region I follows a power-law relationship and specifically COF decreases with the applied normal force raised to the $-1/3$ power, which is consistent with the experimental measurement shown in Figure 5.3a. It should be pointed out that since the value of τ_s is not available for the current *a*-HEA, τ_s is considered as a fitting parameter. In fact, by letting $\tau_s = 1.2$ GPa , the COF variation as a function of normal force in Region I (elastic regime) can be well fitted by Eq. 5.6, as plotted in Figure 5.3a (red line).

On the other hand, when the normal force exceeds the elastic range (i.e., $F_n > 320$ μN , in Region II), the COF gradually increases from 0.11 to 0.18, as shown in Figure 5.3a. In this region, plastic deformation (plowing) takes over and is dominant, as illustrated in Figure 5.4. The plowing COF is defined as $\mu_{pl} = A_l / A_n$ [175], where A_l and A_n are the projections of the contact area in the lateral and normal directions, respectively. Considering the spherical tip geometry in this case, the plowing COF can, then, be written as [175]

$$\mu_{pl} = (2/\pi a^2) \cdot [R^2 \sin^{-1}(a/R) - a\sqrt{R^2 - a^2}] \tag{5.7}$$

where $a = \sqrt{2hR - h^2}$ is the contact radius during plastic deformation. Since the elastic recovery of the current *a*-HEA can be as high as ~ 50% in Region II, elastic recovery of the sample at the rear of the indenter during scratching is also expected to be appreciable. In fact, it has been reported [176-178] that the elastic recovery of a worn material might contribute to the plowing COF in a significant way. Lafaye *et al*. [176, 177] have included the elastic recovery part into the calculation of μ_{pl} and derived the following equation:

$$\mu_{pl} = \frac{2}{a^2} \cdot \frac{\beta^2 \sin^{-1}(\frac{a\cos\omega}{\beta}) - a\cos\omega\sqrt{R^2 - a^2}}{\pi + 2\omega + \sin 2\omega} \tag{5.8}$$

where $\omega = \sin^{-1}\sqrt{2H(R-h)/(aE_r)}$ is the rear angle, H is the hardness, and $\beta = \sqrt{R^2 - a^2\sin^2\omega}$

is considered as a fictive radius of the indenter. Since the hardness (H), tip radius (R), reduced modulus (E_r) are all constants for the current indenter-sample system, the scratch depth (h) is the only variable in Eq. 5.8. Noted that the scratch depth depends on the applied normal force, which can be directly measured from the scratching tests. Then, by inserting related values into Eq. 5.8, we have the calculated plowing COF, as shown in Figure 5.3a (blue line). It is readily seen in Figure 5.3a that the plowing COF increases with increasing normal force, and the difference between the experimental COF and the calculated plowing COF shrinks as the normal force increases, further confirming that plastic deformation (or plowing mechanism) is dominant in Region II.

To place this in perspective, we further compare the calculated plowing COF with that reported for a crystalline bcc-TiZrHfNb HEA [62] and the data are plotted in Figure 5.9a. It is apparent in the figure that both μ_{pl} monotonically increases with increasing normal force but the *a*-HEA has a lower μ_{pl} at any given normal force. The lower μ_{pl} may be attributed to the fact that a shallower scratch depth (Figure 5.9b) produces a lower μ_{pl} according to Eq. 5.8. As the a-HEA has a higher hardness, thus a shallower depth under the same load, a lower μ_{pl} is obtained. Furthermore, a larger rear angle/elastic recovery is expected to give a lower μ_{pl}, as shown in Figure 5.9c. Since the current *a*-HEA has a much larger elastic recovery than that of the crystalline HEA at any given normal force (Figure 5.9d), it is conducive to a lower μ_{pl}. In summary, high hardness value combined with large elastic recovery leads to a lower μ_{pl} in the *a*-HEA.

From the morphological observations (Figures 5.4 and 5.5), we can also make special attempt to estimate the surface energy of the present *a*-HEA. According to the Griffith criterion

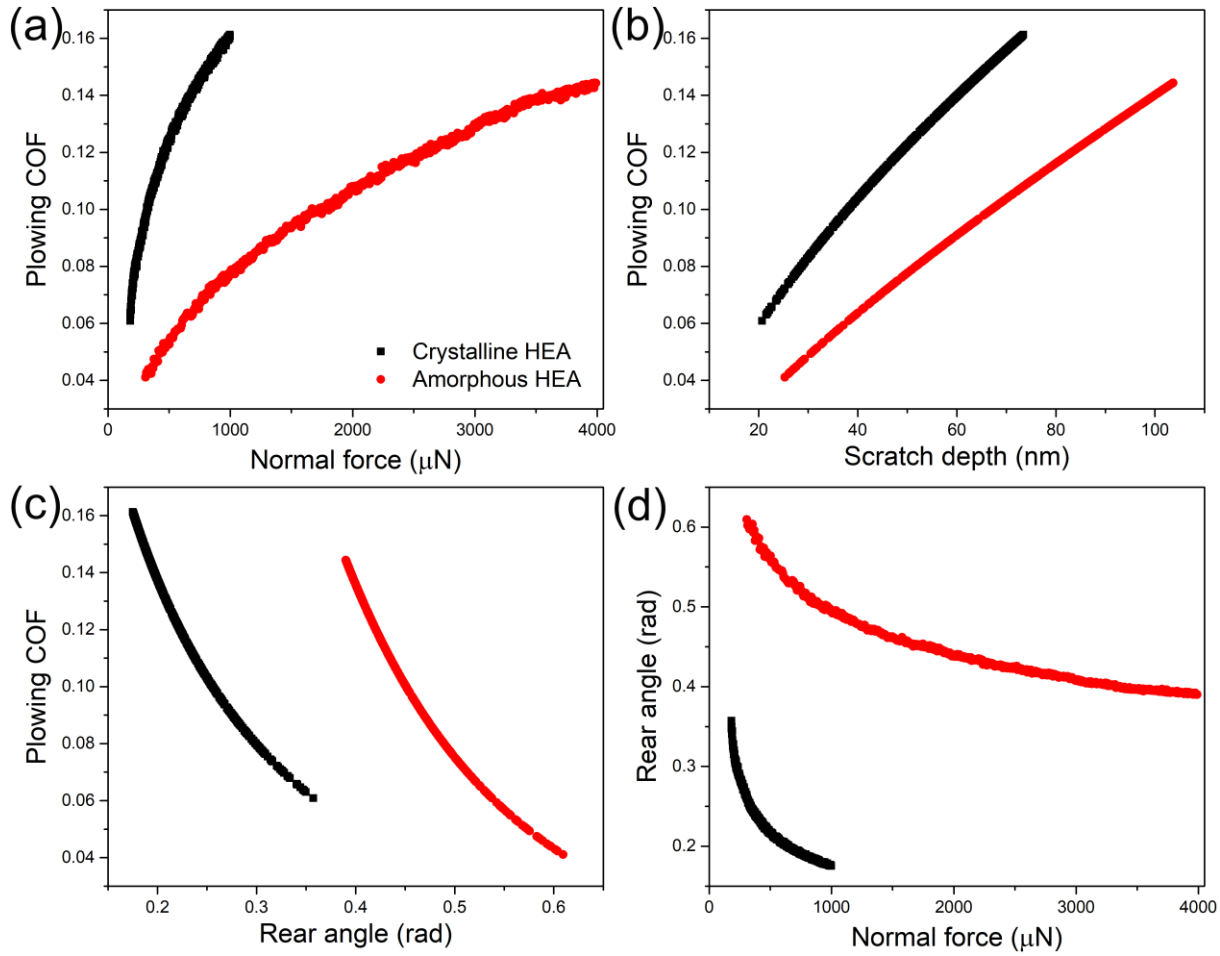

Figure 5.9 Calculated plowing COF against (a) normal force, (b) scratch depth, and (c) rear angle for the amorphous HEA and a bcc-TiZrHfNb HEA [62]. (d) Rear angle plotted against normal force for the amorphous HEA and crystalline HEA.

[179], a brittle crack extends when strain energy is sufficient to create two new crack surfaces, i.e., $G = 2\gamma$, where G is the strain energy dissipation and γ is the surface energy of the material. Under the plane-strain condition [180],

$$G = (1-\nu^2)K^2/E \tag{5.9}$$

where ν is the Poisson's ratio, and K is the stress intensity. In the case when a spherical indenter slides across the sample surface, the maximum radial tension (σ_t) takes place at the trailing edge of the indenter, which is given by [181]

$$\sigma_t = \left(\frac{1-2\nu}{2}\right)(1+Af)\,p_0 \tag{5.10}$$

where $A = [3\pi(4+\nu)]/[8(1-2\nu)]$, f is the COF. Also, $p_0 = P/(\pi a^2)$ is the mean pressure, where P is the normal force, $a = \sqrt{2hR-h^2}$ is the contact radius, where h is the scratch depth, and R is the indenter tip radius. When $h << R$, the radial stress decreases with increasing depth. In other words, a stress gradient is developed below the trailing edge of the indenter. To a good approximation, the stress intensity for an edge crack under a graded stress field is [182]

$$K = 1.12\sigma_t\sqrt{\pi c} \tag{5.11}$$

where c is the crack length. By incorporating Eqs. 5.10 and 5.11 into Eq. 5.9, we can readily deduce the fracture toughness (K), strain energy release rate (G), and surface energy (γ). For the current brittle *a*-HEA ($\nu = 0.35$, adopted from the conventional Zr-Ti-Cu-Ni-Be amorphous alloys [157]), the critical load for extending the radial cracks ($c \approx 100$ nm from Figure 5.4c) at scratch banks is $P = 1200$ μN (corresponding to $f = 0.13$ and $h = 55$ nm from Figures 5.3a and 5.3b), resulting in $K = 1.84$ MPam$^{1/2}$, $G = 22$ J/m^2, and $\gamma = 11$ J/m^2. This γ value is much lower than that of ductile crystalline HEAs (10^5 J/m^2 [183, 184]), but falls in the low range for those

reported in a number of amorphous alloys (10^1-10^5 J/m^2 [185, 186]), affirming the brittle nature of the *a*-HEA during scratching. Apparently, a high entropy does not enhance the surface energy, thus fracture resistance, of the current the *a*-HEA. It should be noted that the current estimation of surface energy is oversimplified. To get an accurate calculation, identification of the crack initiation site and calculation of the exact profile of the stress field will be considered and included in the future.

5.4 Summary

In this chapter, I conducted a series of nanoscratch tests on an amorphous $Zr_{20}Ti_{20}Cu_{20}Ni_{20}Be_{20}$ HEA (*a*-HEA) to investigate its tribological behavior. Friction of the *a*-HEA can generally be divided into two regions: elastic and plastic. In the elastic region, the COF decreases sharply with increasing normal force from ~ 1 to 0.11 and follows a power-law with the power index of $-1/3$. By contrast, in the plastic region, the COF monotonically increases from 0.11 to 0.18. Brittle fracture dominates in the plastic region, as manifested by many large load serrations in the COF curve, as well as the morphology of scratched surface. Radial cracks were observed along the banks of scratched groove, and the crack spacing decreases with increasing normal force. No crystallization was observed underneath the scratched surface. The current *a*-HEA exhibits good wear resistance, which is simply attributable to a high strength or hardness. However, it behaves more like brittle amorphous alloys rather than ductile HEAs. The amorphous alloy also has a relatively low COF, mainly is a result of low plowing COF, which is, in turn, resulted from high hardness and large elastic recovery. The good wear resistance coupled with a low COF suggests that *a*-HEAs are probably good candidate materials for tribological applications.

Chapter 6. Research summary and suggested future directions

6.1 Conclusions

In this dissertation, the intrinsic strength (or lattice friction stress) of fcc Ni-based and bcc Nb-based equiatomic alloys, thermal stability and coarsening of coherent particles in a precipitation-hardened fcc-$(NiCoFeCr)_{94}Ti_2Al_4$ high-entropy alloy (HEA), and tribological behavior of an amorphous $Zr_{20}Ti_{20}Cu_{20}Ni_{20}Be_{20}$ HEA have been systematically investigated.

In the study of lattice friction stress in fcc Ni-based and bcc Nb-based equiatomic alloys, yield strength of each material was measured. The lattice distortion in these equiatomic alloys were quantitatively evaluated. The magnitude of lattice distortion in these alloys does not necessarily increase with increasing number of constituent components, and lattice distortion in bcc Nb-based alloys is larger than that in fcc Ni-based equiatomic alloys. After subtracting the strength contributions from all possible mechanisms, the lattice friction stress of each of the current alloys is extracted and we find that it scales linearly with the lattice distortion in these alloys. In addition, lattice distortion in bcc Nb-based alloys can apparently produce a much higher hardening effect than that in fcc Ni-based equiatomic alloys. The much higher friction stress of bcc-HEAs compared to that of fcc-HEAs may be attributed to a smaller dislocation core. The current results suggest that remarkable strength enhancement in HEAs is probably resulted from a high friction stress, which is, in turn, caused by lattice distortion.

For the study on the coarsening of coherent precipitates in the fcc-$(NiCoFeCr)_{94}Ti_2Al_4$ HEA, we found that coherent $L1_2$ precipitates formed in the HEA appear to be spheroidal and relatively uniformly distributed. These precipitates remain spheroid in shape even after aging at

800 °C for 503 h, indicating a relatively low driving force for coarsening. The current $(NiCoFeCr)_{94}Ti_2Al_4$ can be treated as a pseudo ternary Ni-Ti-Al alloy. By applying the precipitate coarsening model for ternary alloy systems, coarsening kinetics in the alloy has been analyzed. The activation energy for precipitate coarsening is estimated to be 276 kJ/mol, which compares favorably with that for the diffusion of Al or Ti in Ni-based alloys. It is higher than the activation energy for Ni diffusion in the NiCoFeCr-based HEA (227 kJ/mol), suggesting that precipitate coarsening is probably controlled by the diffusion of either Al or Ti, or both, in the fcc-NiCoFeCr matrix. Resulting from sluggish diffusion, precipitate coarsening rate in the $(NiCoFeCr)_{94}Ti_2Al_4$ alloy is one to two orders of magnitude lower than that in many traditional Ni-based alloys. The slow diffusion contributes to the good thermal stability of the $L1_2$ precipitates. Strengthening observed in the current HEA was successfully described by the mechanism of precipitate shearing by either weakly or strongly coupled partial-dislocation pairs, depending on the precipitate size, and the optimal precipitate size is about 22-25 nm. The good thermal stability of the $L1_2$ precipitates implies that the current fcc-HEA may have potential for structural applications at elevated temperatures.

In the work to investigate tribological behavior of an amorphous $Zr_{20}Ti_{20}Cu_{20}Ni_{20}Be_{20}$ HEA (a-HEA), we found that friction behavior of the a-HEA can be divided into two stages: elastic and plastic. In the elastic region, the COF decreases sharply with increasing normal force from ~ 1 to 0.11 and follows a power-law with the power index of $-1/3$. By contrast, in the plastic region, the COF monotonically increases from 0.11 to 0.18. Brittle fracture dominates in the plastic region, as manifested by many large load serrations in the COF curve, as well as the morphology of scratched surface. Radial cracks were observed along the banks of scratched groove, and the crack spacing decreases with increasing normal force. No crystallization was

observed underneath the scratched surface. The current *a*-HEA exhibits good wear resistance, which is simply attributable to a high strength or hardness. However, it behaves more like brittle amorphous alloys rather than ductile HEAs. The amorphous alloy also has a relatively low COF, mainly is a result of low plowing COF, which is, in turn, resulted from high hardness and large elastic recovery. The good wear resistance coupled with a low COF suggests that *a*-HEAs are probably good candidate materials for tribological applications.

In summary, extensive efforts have been made to accomplish these research work. My dissertation work is expected to provide the scientific community with better understandings of intrinsic strength, precipitation hardening and tribological behavior of high-entropy alloys.

6.2 Recommended future directions

Inspired by our findings, future research directions are recommended.

First, our model used for measuring lattice distortion is imperfect. Local lattice distortion and interatomic chemical bonding should be considered. Thus, simulation methods should be employed to quantitatively describe lattice distortion in HEAs. In fact, Okamoto *et al* [83] used the first-principles to calculate the interatomic bond length and the average root-mean-square atomic displacements ($(MSAD)^{1/2}$) of the constituent atoms in the Cantor alloy and found an empirical correlation between $(MSAD)^{1/2}$ and the yield strength of HEAs. However, a physical-base quantitative connection between the atomic-scale lattice distortion and macroscopic mechanical properties, for example, lattice friction stress, is still missing.

Second, as the coarsening of $L1_2$ precipitates in the $(NiCoFeCr)_{94}Ti_2Al_4$ HEA was much slower than that in the conventional Ni-based alloys, it will be of great interest to study high-temperature creep behavior of the HEA. Considering the mixing microstructure of heterogeneous

precipitation at grain boundaries and homogeneous precipitation inside grains, its effect on the subsequent creep properties is uncertain. It is noted that high-temperature nanoindentation technique can be employed to investigate the local creep behavior. For example, Oliver *et al.* [187] has recently performed indentation creep experiments on commercial purity aluminum alloy at temperatures up to 550 °C, and they found that power-law type creep constitutive behavior calculated from the indentation experiments is in good agreement with the conventional uniaxial results. In fact, some preliminary studies have been recently carried out on some Cantor alloy-based HEAs [188]. Therefore, we can apply this technique to study the high-temperature deformation mechanism of HEAs, in general.

Third, design a-HEAs with high strength/hardness and improved ductility for tribological applications. As mentioned in Chapter 5, we found that the $Zr_{20}Ti_{20}Cu_{20}Ni_{20}Be_{20}$ a-HEA has good wear resistance and low COF, making the materials have potential for wear applications. However, brittle fracture dominates the plastic deformation during scratching, which apparently should be avoided. Therefore, it is necessary to design new a-HEAs with improved ductility in order to avoid fracture failure during tribological contact.

References

[1] B. Cantor, I.T.H. Chang, P. Knight, A.J.B. Vincent, Microstructural development in equiatomic multicomponent alloys, Mater. Sci. Eng. A 375 (2004) 213-218.

[2] J.W. Yeh, S.K. Chen, S.J. Lin, J.Y. Gan, T.S. Chin, T.T. Shun, C.H. Tsau, S.Y. Chang, Nanostructured high-entropy alloys with multiple principal elements: novel alloy design concepts and outcomes, Adv. Eng. Mater. 6 (2004) 299-303.

[3] J.W. Yeh, Recent progress in high entropy alloys, Ann. Chim. Sci. Mat. 31 (2006) 633-648.

[4] Y. Zhang, T.T. Zuo, Z. Tang, M.C. Gao, K.A. Dahmen, P.K. Liaw, Z.P. Lu, Microstructures and properties of high-entropy alloys, Prog. Mater. Sci. 61 (2014) 1-93.

[5] D.B. Miracle, O.N. Senkov, A critical review of high entropy alloys and related concepts, Acta Mater. 122 (2017) 448-511.

[6] Y. Shi, B. Yang, P. Liaw, Corrosion-resistant high-entropy alloys: A review, Metals 7 (2017) 43.

[7] C. Huang, Y. Zhang, J. Shen, R. Vilar, Thermal stability and oxidation resistance of laser clad TiVCrAlSi high entropy alloy coatings on Ti-6Al-4V alloy, Surf. Coat. Technol. 206 (2011) 1389-1395.

[8] K.Y. Tsai, M.H. Tsai, J.W. Yeh, Sluggish diffusion in Co-Cr-Fe-Mn-Ni high-entropy alloys, Acta Mater. 61 (2013) 4887-4897.

[9] Y. Zou, H. Ma, R. Spolenak, Ultrastrong ductile and stable high-entropy alloys at small scales, Nat. Commun. 6 (2015) 7748.

[10] J.W. Yeh, S.Y. Chang, Y.D. Hong, S.K. Chen, S.J. Lin, Anomalous decrease in X-ray diffraction intensities of Cu-Ni-Al-Co-Cr-Fe-Si alloy systems with multi-principal elements, Mater. Chem. Phys. 103 (2007) 41-46.

[11] W. Guo, W. Dmowski, J.Y. Noh, P. Rack, P.K. Liaw, T. Egami, Local atomic structure of a high-entropy alloy: an X-ray and neutron scattering study, Metall. Mater. Trans. A 44 (2013) 1994-1997.

[12] S. Wang, Atomic structure modeling of multi-principal-element alloys by the principle of maximum entropy, Entropy 15 (2013) 5536-5548.

[13] Y. Zou, S. Maiti, W. Steurer, R. Spolenak, Size-dependent plasticity in an $Nb_{25}Mo_{25}Ta_{25}W_{25}$ refractory high-entropy alloy, Acta Mater. 65 (2014) 85-97.

[14] ASM Handbook Vol. 2, Properties and Selection: Nonferrous Alloys and Special-Purpose Materials, ASM International, Materials Park, OH, 1990.

[15] J.Y. He, W.H. Liu, H. Wang, Y. Wu, X.J. Liu, T.G. Nieh, Z.P. Lu, Effects of Al addition on

structural evolution and tensile properties of the FeCoNiCrMn high-entropy alloy system, Acta Mater. 62 (2014) 105-113.

[16] Y. Wu, W.H. Liu, X.L. Wang, D. Ma, A.D. Stoica, T.G. Nieh, Z.B. He, Z.P. Lu, In-situ neutron diffraction study of deformation behavior of a multi-component high-entropy alloy, Appl. Phys. Lett. 104 (2014) 051910.

[17] A. Gali, E.P. George, Tensile properties of high-and medium-entropy alloys, Intermetallics 39 (2013) 74-78.

[18] F. Otto, A. Dlouhý, C. Somsen, H. Bei, G. Eggeler, E.P. George, The influences of temperature and microstructure on the tensile properties of a CoCrFeMnNi high-entropy alloy, Acta Mater. 61 (2013) 5743-5755.

[19] R.L. Fleischer, Substitutional solution hardening, Acta Metall. 11 (1963) 203-209.

[20] O.N. Senkov, J.M. Scott, S.V. Senkova, D.B. Miracle, C.F. Woodward, Microstructure and room temperature properties of a high-entropy TaNbHfZrTi alloy, J. Alloys Compd. 509 (2011) 6043-6048.

[21] I. Toda-Caraballo, P.E. Rivera-Díaz-del-Castillo, Modelling solid solution hardening in high entropy alloys, Acta Mater. 85 (2015) 14-23.

[22] C. Varvenne, G.P.M. Leyson, M. Ghazisaeidi, W.A. Curtin, Solute strengthening in random alloys, Acta Mater. 124 (2017) 660-683.

[23] Z. Wu, H. Bei, G.M. Pharr, E.P. George, Temperature dependence of the mechanical properties of equiatomic solid solution alloys with face-centered cubic crystal structures, Acta Mater. 81 (2014) 428-441.

[24] Z. Wu, Y. Gao, H. Bei, Thermal activation mechanisms and Labusch-type strengthening analysis for a family of high-entropy and equiatomic solid-solution alloys, Acta Mater. 120 (2016) 108-119.

[25] Y.Y. Zhao, T.G. Nieh, Correlation between lattice distortion and friction stress in Ni-based equiatomic alloys, Intermetallics 86 (2017) 45-50.

[26] Y.Y. Zhao, Z.F. Lei, Z.P. Lu, J.C. Huang, T.G. Nieh, A simplified model connecting lattice distortion with friction stress of Nb-based equiatomic high-entropy alloys, Mater. Res. Lett. 7 (2019) 340-346.

[27] M.H. Tsai, J.W. Yeh, J.Y. Gan, Diffusion barrier properties of AlMoNbSiTaTiVZr high-entropy alloy layer between copper and silicon, Thin Solid Films 516 (2008) 5527-5530.

[28] O.N. Senkov, G.B. Wilks, J.M. Scott, D.B. Miracle, Mechanical properties of $Nb_{25}Mo_{25}Ta_{25}W_{25}$ and $V_{20}Nb_{20}Mo_{20}Ta_{20}W_{20}$ refractory high entropy alloys, Intermetallics 19 (2011) 698-

706.

[29] J.Y. He, H. Wang, H.L. Huang, X.D. Xu, M.W. Chen, Y. Wu, X.J. Liu, T.G. Nieh, K. An, Z.P. Lu, A precipitation-hardened high-entropy alloy with outstanding tensile properties, Acta Mater. 102 (2016) 187-196.

[30] Q. Wang, Y. Ma, B. Jiang, X. Li, Y. Shi, C. Dong, P.K. Liaw, A cuboidal B2 nanoprecipitation-enhanced body-centered-cubic alloy $Al_{0.7}CoCrFe_2Ni$ with prominent tensile properties, Scr. Mater. 120 (2016) 85-89.

[31] Y.L. Zhao, T. Yang, Y. Tong, J. Wang, J.H. Luan, Z.B. Jiao, D. Chen, Y. Yang, A. Hu, C.T. Liu, Heterogeneous precipitation behavior and stacking-fault-mediated deformation in a CoCrNi-based medium-entropy alloy, Acta Mater. 138 (2017) 72-82.

[32] B. Gwalani, D. Choudhuri, V. Soni, Y. Ren, M. Styles, J. Hwang, S. Nam, H. Ryu, S. Hong, R. Banerjee, Cu assisted stabilization and nucleation of L1 2 precipitates in $Al_{0.3}CuFeCrNi_2$ fcc-based high entropy alloy, Acta Mater. 129 (2017) 170-182.

[33] R.C. Reed, The Superalloys: Fundamentals and Applications, Cambridge University Press, UK, 2008.

[34] A.J. Ardell, R.B. Nicholson, The coarsening of γ' in Ni-Al alloys, J. Phys. Chem. Solid. 27 (1966) 1793-1794.

[35] X. Li, N. Saunders, A.P. Miodownik, The coarsening kinetics of γ′ particles in nickel-based alloys, Metall. Mater. Trans. A 33 (2002) 3367-3373.

[36] V.A. Vorontsov, J.S. Barnard, K.M. Rahman, H.Y. Yan, P.A. Midgley, D. Dye, Coarsening behaviour and interfacial structure of γ′ precipitates in Co-Al-W based superalloys, Acta Mater. 120 (2016) 14-23.

[37] E.A. Marquis, D.N. Seidman, Nanoscale structural evolution of Al_3Sc precipitates in Al (Sc) alloys, Acta Mater. 49 (2001) 1909-1919.

[38] K. Mahalingam, B.P. Gu, G.L. Liedl, T.H. Sanders, coarsening of δ′(Al_3Li) precipitates in binary Al-Li alloys, Acta Metall. 35 (1987) 483-498.

[39] J.Y. He, H. Wang, Y. Wu, X.J. Liu, H.H. Mao, T.G. Nieh, Z.P. Lu, Precipitation behavior and its effects on tensile properties of FeCoNiCr high-entropy alloys, Intermetallics 79 (2016) 41-52.

[40] Y.Y. Zhao, H.W. Chen, Z.P. Lu, T.G. Nieh, Thermal stability and coarsening of coherent particles in a precipitation-hardened $(NiCoFeCr)_{94}Ti_2Al_4$ high-entropy alloy, Acta Mater. 147 (2018) 184-194.

[41] I.M. Lifshitz, V.V. Slyozov, The kinetics of precipitation from supersaturated solid

solutions, J. Phys. Chem. Solid 19 (1961) 35-50.

[42] C. Wagner, Theorie der alterung von niederschlägen durch umlösen (Ostwald-reifung), Z. Elektrochem. 65 (1961) 581-591.

[43] A.J. Ardell, Precipitation hardening, Metall. Trans. A 16 (1985) 2131-2165.

[44] A. Kelly, Strengthening methods in crystals, John Wiley and Sons, New York, NY, 1971.

[45] D. Raynor, J.M. Silcock, Strengthening mechanisms in γ′ precipitating alloys, Met. Sci. J. 4 (1970) 121-130.

[46] D.M. Collins, H.J. Stone, A modelling approach to yield strength optimisation in a nickel-base superalloy, Int. J. Plast. 54 (2014) 96-112.

[47] K.M. Youssef, A.J. Zaddach, C. Niu, D.L. Irving, C.C. Koch, A novel low-density, high-hardness, high-entropy alloy with close-packed single-phase nanocrystalline structures, Mater. Res. Lett. 3 (2015) 95-99.

[48] B. Schuh, F. Mendez-Martin, B. Völker, E.P. George, H. Clemens, R. Pippan, A. Hohenwarter, Mechanical properties, microstructure and thermal stability of a nanocrystalline CoCrFeMnNi high-entropy alloy after severe plastic deformation, Acta Mater. 96 (2015) 258-268.

[49] S. Varalakshmi, M. Kamaraj, B. Murty, Synthesis and characterization of nanocrystalline AlFeTiCrZnCu high entropy solid solution by mechanical alloying, J. Alloys Compd. 460 (2008) 253-257.

[50] L. Ma, L. Wang, T. Zhang, A. Inoue, Bulk glass formation of Ti-Zr-Hf-Cu-M (M= Fe, Co, Ni) alloys, Mater. Trans. 43 (2002) 277-280.

[51] K. Zhao, X. Xia, H. Bai, D. Zhao, W. Wang, Room temperature homogeneous flow in a bulk metallic glass with low glass transition temperature, Appl. Phys. Lett. 98 (2011) 141913.

[52] H. Ding, K. Yao, High entropy $Ti_{20}Zr_{20}Cu_{20}Ni_{20}Be_{20}$ bulk metallic glass, J. Non-Cryst. Solids 364 (2013) 9-12.

[53] J. Kim, H.S. Oh, J. Kim, C.W. Ryu, G.W. Lee, H.J. Chang, E.S. Park, Utilization of high entropy alloy characteristics in Er-Gd-Y-Al-Co high entropy bulk metallic glass, Acta Mater. 155 (2018) 350-361.

[54] F. Wang, A. Inoue, F. Kong, S. Zhu, E. Shalaan, F. Al-Marzouki, W. Botta, C. Kiminami, Y.P. Ivanov, A. Greer, Formation, stability and ultrahigh strength of novel nanostructured alloys by partial crystallization of high-entropy $(Fe_{0.25}Co_{0.25}Ni_{0.25}Cr_{0.125}Mo_{0.125})_{86–89}B_{11–14}$ amorphous phase, Acta Mater. 170 (2019) 50-61.

[55] A. Takeuchi, N. Chen, T. Wada, Y. Yokoyama, H. Kato, A. Inoue, J. Yeh, $Pd_{20}Pt_{20}Cu_{20}Ni_{20}P_{20}$ high-entropy alloy as a bulk metallic glass in the centimeter, Intermetallics 19 (2011) 1546-1554.

[56] M. Yang, X.J. Liu, Y. Wu, H. Wang, X.Z. Wang, Z.P. Lu, Unusual relation between glass-forming ability and thermal stability of high-entropy bulk metallic glasses, Mater. Res. Lett. 6 (2018) 495-500.

[57] M. Yang, X.J. Liu, H.H. Ruan, Y. Wu, H. Wang, Z.P. Lu, High thermal stability and sluggish crystallization kinetics of high-entropy bulk metallic glasses, J. Appl. Phys. 119 (2016) 245112.

[58] T. Qi, Y. Li, A. Takeuchi, G. Xie, H. Miao, W. Zhang, Soft magnetic $Fe_{25}Co_{25}Ni_{25}(B, Si)_{25}$ high entropy bulk metallic glasses, Intermetallics 66 (2015) 8-12.

[59] Y.Y. Zhao, Y.X. Ye, C.Z. Liu, R. Feng, K.F. Yao, T.G. Nieh, Tribological behavior of an amorphous $Zr_{20}Ti_{20}Cu_{20}Ni_{20}Be_{20}$ high-entropy alloy studied using a nanoscratch technique, Intermetallics 113 (2019) 106561.

[60] J.G. Wang, B.W. Choi, T.G. Nieh, C.T. Liu, Nano-scratch behavior of a bulk Zr–10Al–5Ti–17.9 Cu–14.6 Ni amorphous alloy, J. Mater. Res. 15 (2000) 913-922.

[61] A.M. Hodge, T.G. Nieh, Evaluating abrasive wear of amorphous alloys using nanoscratch technique, Intermetallics 12 (2004) 741-748.

[62] Y.X. Ye, C.Z. Liu, H. Wang, T.G. Nieh, Friction and wear behavior of a single-phase equiatomic TiZrHfNb high-entropy alloy studied using a nanoscratch technique, Acta Mater. 147 (2018) 78-89.

[63] T. Egami, M. Ojha, O. Khorgolkhuu, D.M. Nicholson, G.M. Stocks, Local Electronic Effects and Irradiation Resistance in High-Entropy Alloys, JOM 67 (2015) 2345-2349.

[64] Z. Wu, Temperature and Alloying Effects on the Mechanical Properties of Equiatomic FCC Solid Solution Alloys, PhD diss., University of Tennessee, 2014.

[65] S. Guo, C. Ng, Z. Wang, C.T. Liu, Solid solutioning in equiatomic alloys: limit set by topological instability, J. Alloys Compd. 583 (2014) 410-413.

[66] X. Wang, H. Xie, L. Jia, Z.L. Lu, Effect of Ti, Al and Cu addition on structural evolution and phase constitution of FeCoNi system equimolar alloys, Mater. Sci. Forum 724 (2012) 335-338.

[67] G.A. Salishchev, M.A. Tikhonovsky, D.G. Shaysultanov, N.D. Stepanov, A.V. Kuznetsov, I.V. Kolodiy, A.S. Tortika, O.N. Senkov, Effect of Mn and V on structure and mechanical properties of high-entropy alloys based on CoCrFeNi system, J. Alloys Compd. 591 (2014) 11-21.

[68] W.H. Liu, J.Y. He, H.L. Huang, H. Wang, Z.P. Lu, C.T. Liu, Effects of Nb additions on the microstructure and mechanical property of CoCrFeNi high-entropy alloys, Intermetallics 60 (2015) 1-8.

[69] N.N. Greenwood, A. Earnshaw, Chemistry of the Elements, Pergamon Press, Oxford, UK, 1984.

[70] D. Wu, J. Zhang, J.C. Huang, H. Bei, T.G. Nieh, Grain-boundary strengthening in nanocrystalline chromium and the Hall–Petch coefficient of body-centered cubic metals, Scr. Mater. 68 (2013) 118-121.

[71] Z. Wu, H. Bei, F. Otto, G.M. Pharr, E.P. George, Recovery, recrystallization, grain growth and phase stability of a family of FCC-structured multi-component equiatomic solid solution alloys, Intermetallics 46 (2014) 131-140.

[72] J.E. Bailey, P.B. Hirsch, The dislocation distribution, flow stress, and stored energy in cold-worked polycrystalline silver, Philos. Mag. 5 (1960) 485-497.

[73] T.H. Courtney, Mechanical Behavior of Materials, Waveland Press, Long Grove, IL, 2000.

[74] T. Narutani, J. Takamura, Grain-size strengthening in terms of dislocation density measured by resistivity, Acta Metall. Mater. 39 (1991) 2037-2049.

[75] G.K. Williamson, R.E. Smallman, III. Dislocation densities in some annealed and cold-worked metals from measurements on the X-ray debye-scherrer spectrum, Philos. Mag. 1 (1956) 34-46.

[76] W.H. Liu, Y. Wu, J.Y. He, T.G. Nieh, Z.P. Lu, Grain growth and the Hall–Petch relationship in a high-entropy FeCrNiCoMn alloy, Scr. Mater. 68 (2013) 526-529.

[77] A.A. Thompson, Yielding in nickel as a function of grain or cell size, Acta Metall. 23 (1975) 1337-1342.

[78] Y. Kamimura, K. Edagawa, S. Takeuchi, Experimental evaluation of the Peierls stresses in a variety of crystals and their relation to the crystal structure, Acta Mater. 61 (2013) 294-309.

[79] R. Peierls, The size of a dislocation, Proc. Phys. Soc. 52 (1940) 34-37.

[80] F.R.N. Nabarro, Dislocations in a simple cubic lattice, Proc. Phys. Soc. 59 (1947) 256-272.

[81] O.N. Senkov, G.B. Wilks, D.B. Miracle, C.P. Chuang, P.K. Liaw, Refractory high-entropy alloys, Intermetallics 18 (2010) 1758-1765.

[82] F. Czerwinski, P.T. Jochym, L. Litynska-Dobrzynska, Microstructure and mechanical properties of the novel $Hf_{25}Sc_{25}Ti_{25}Zr_{25}$ equiatomic alloy with hexagonal solid solutions, Mater. Des. 92 (2016) 8-17.

[83] N.L. Okamoto, K. Yuge, K. Tanaka, H. Inui, E.P. George, Atomic displacement in the CrMnFeCoNi high-entropy alloy-A scaling factor to predict solid solution strengthening, AIP Adv. 6 (2016) 125008.

[84] J.Y. He, Q. Wang, H. Zhang, L. Dai, T. Mukai, Y. Wu, X. Liu, H. Wang, T.G. Nieh, Z.P. Lu, Dynamic deformation behavior of a face-centered cubic FeCoNiCrMn high-entropy alloy, Sci. Bull. 63 (2018) 362-368.

[85] Z.F. Lei, X.J. Liu, Y. Wu, H. Wang, S.H. Jiang, S.D. Wang, X.D. Hui, Y.D. Wu, B. Gault, P. Kontis, D. Raabe, L. Gu, Q.H. Zhang, H.W. Chen, H.T. Wang, J.B. Liu, K. An, Q.S. Zeng, T.G. Nieh, Z.P. Lu, Enhanced strength and ductility in a high-entropy alloy via ordered oxygen complexes, Nature 563 (2018) 546-550.

[86] J.B. Nelson, D.P. Riley, An experimental investigation of extrapolation methods in the derivation of accurate unit-cell dimensions of crystals, Proc. Phys. Soc. 57 (1945) 160-177.

[87] Y.D. Wu, Y.H. Cai, T. Wang, J.J. Si, J. Zhu, Y.D. Wang, X.D. Hui, A refractory $Hf_{25}Nb_{25}Ti_{25}Zr_{25}$ high-entropy alloy with excellent structural stability and tensile properties, Mater. Lett. 130 (2014) 277-280.

[88] B. Schuh, B. Völker, J. Todt, N. Schell, L. Perrière, J. Li, J.P. Couzinié, A. Hohenwarter, Thermodynamic instability of a nanocrystalline, single-phase TiZrNbHfTa alloy and its impact on the mechanical properties, Acta Mater. 142 (2018) 201-212.

[89] O.N. Senkov, S.L. Semiatin, Microstructure and properties of a refractory high-entropy alloy after cold working, J. Alloys Compd. 649 (2015) 1110-1123.

[90] O.N. Senkov, A.L. Pilchak, S.L. Semiatin, Effect of Cold Deformation and Annealing on the Microstructure and Tensile Properties of a HfNbTaTiZr Refractory High Entropy Alloy, Metall. Mater. Trans. A 49 (2018) 2876-2892.

[91] C.C. Juan, M.H. Tsai, C.W. Tsai, W.L. Hsu, C.M. Lin, S.K. Chen, S.J. Lin, J.W. Yeh, Simultaneously increasing the strength and ductility of a refractory high-entropy alloy via grain refining, Mater. Lett. 184 (2016) 200-203.

[92] H. Song, F. Tian, Q.M. Hu, L. Vitos, Y. Wang, J. Shen, N. Chen, Local lattice distortion in high-entropy alloys, Phy. Rev. Mater. 1 (2017) 023404.

[93] E.O. Hall, The deformation and ageing of mild steel: III discussion of results, Proc. Phys. Soc. Sect. B 64 (1951) 747-753.

[94] H.M. Ledbetter, Ratio of the shear and Young's moduli for polycrystalline metallic elements, Mater. Sci. Eng. 27 (1977) 133-135.

[95] H. Conrad, S. Feuerstein, L. Rice, Effects of grain size on the dislocation density and flow stress of niobium, Mater. Sci. Eng. 2 (1967) 157-168.

[96] Z.C. Cordero, B.E. Knight, C.A. Schuh, Six decades of the Hall–Petch effect–a survey of grain-size strengthening studies on pure metals, Int. Mater. Rev. 61 (2016) 495-512.

[97] M. Laurent-Brocq, A. Akhatova, L. Perrière, S. Chebini, X. Sauvage, E. Leroy, Y. Champion, Insights into the phase diagram of the CrMnFeCoNi high entropy alloy, Acta Mater. 88 (2015) 355-365.

[98] C. Lee, G. Song, M.C. Gao, R. Feng, P. Chen, J. Brechtl, Y. Chen, K. An, W. Guo, J.D. Poplawsky, S. Li, A.T. Samaei, W. Chen, A. Hu, H. Choo, P.K. Liaw, Lattice distortion in a strong and ductile refractory high-entropy alloy, Acta Mater. 160 (2018) 158-172.

[99] J.R. Greer, J.T.M. De Hosson, Plasticity in small-sized metallic systems: Intrinsic versus extrinsic size effect, Prog. Mater. Sci. 56 (2011) 654-724.

[100] G.E. Dieter, Mechanical Metallurgy, McGraw-Hill, New York, 1961.

[101] C. Varvenne, A. Luque, W.A. Curtin, Theory of strengthening in fcc high entropy alloys, Acta Mater. 118 (2016) 164-176.

[102] Z. Wu, Y. Gao, H. Bei, Single crystal plastic behavior of a single-phase, face-center-cubic-structured, equiatomic FeNiCrCo alloy, Scr. Mater. 109 (2015) 108-112.

[103] L. Patriarca, A. Ojha, H. Sehitoglu, Y. Chumlyakov, Slip nucleation in single crystal FeNiCoCrMn high entropy alloy, Scr. Mater. 112 (2016) 54-57.

[104] M. Dao, R.J. Asaro, Localized deformation modes and non-Schmid effects in crystalline solids. Part I. Critical conditions of localization, Mech. Mater. 23 (1996) 71-102.

[105] A. Patra, T. Zhu, D.L. McDowell, Constitutive equations for modeling non-Schmid effects in single crystal bcc-Fe at low and ambient temperatures, Int. J. Plast. 59 (2014) 1-14.

[106] R. Gröger, V. Racherla, J. Bassani, V. Vitek, Multiscale modeling of plastic deformation of molybdenum and tungsten: II. Yield criterion for single crystals based on atomistic studies of glide of 1/2< 111> screw dislocations, Acta Mater. 56 (2008) 5412-5425.

[107] M. Yang, D. Yan, F. Yuan, P. Jiang, E. Ma, X. Wu, Dynamically reinforced heterogeneous grain structure prolongs ductility in a medium-entropy alloy with gigapascal yield strength, PNAS 115 (2018) 7224-7229.

[108] S.S. Sohn, A. Kwiatkowski da Silva, Y. Ikeda, F. Körmann, W. Lu, W.S. Choi, B. Gault, D. Ponge, J. Neugebauer, D. Raabe, Ultrastrong medium-entropy single-phase alloys designed via severe lattice distortion, Adv. Mater. 31 (2019) 1807142.

[109] E.E. Underwood, The mathematical foundations of quantitative stereology, in: G. Pellissier, S. Purdy (Eds.), Stereology and Quantitative Metallography, ASTM International, West Conshohocken, PA, 1972, pp. 3-38.

[110] L.G. Parratt, Probability and Experimental Errors in Science: An Elementary Survey, John Wiley and Sons, New York, NY, 1961.

[111] T. Miyazaki, M. Doi, Shape bifurcations in the coarsening of precipitates in elastically constrained systems, Mater. Sci. Eng. A 110 (1989) 175-185.

[112] C.K. Sudbrack, K.E. Yoon, R.D. Noebe, D.N. Seidman, Temporal evolution of the nanostructure and phase compositions in a model Ni-Al-Cr alloy, Acta Mater. 54 (2006) 3199-3210.

[113] C. Schmuck, P. Caron, A. Hauet, D. Blavette, Ordering and precipitation of γ′ phase in low supersaturated Ni-Cr-Al model alloy: an atomic scale investigation, Philo. Mag. A 76 (1997) 527-542.

[114] A. Ardell, R.B. Nicholson, On the modulated structure of aged Ni-Al alloys, Acta Metall. 14 (1966) 1295-1309.

[115] A.M. Irisarri, J.J. Urcola, M. Fuentes, Kinetics of growth of γ′-precipitates in Ni-6.75AI alloy, Mater. Sci. Technol. 1 (1985) 516-519.

[116] A.J. Ardell, The growth of gamma prime precipitates in aged Ni-Ti alloys, Metall. Mater. Trans. B 1 (1970) 525-534.

[117] A.J. Ardell, D. Kim, V. Ozolins, Ripening of $L1_2$ Ni_3Ti precipitates in the framework of the trans-interface diffusion-controlled theory of particle coarsening, Z. Metallkd. 97 (2006) 295-302.

[118] C.K.L. Davies, P. Nash, R.N. Stevens, Precipitation in Ni-Co-Al alloys, J. Mater. Sci. 15 (1980) 1521-1532.

[119] N. Njah, O. Dimitrov, Microstructural evolution of nickel-rich Ni-Al-Ti alloys during aging treatments: The effect of composition, Acta Metall. 37 (1989) 2559-2566.

[120] W. Hein, Nucleation, growth and coarsening of γ′-precipitates in Ni-5.0at.% Al-5.8at.% Ti, Acta Metall. 37 (1989) 2145-2152.

[121] T. Maebashi, M. Doi, Coarsening behaviours of coherent γ′ and γ precipitates in elastically constrained Ni-Al-Ti alloys, Mater. Sci. Eng. A 373 (2004) 72-79.

[122] P.K. Footner, B.P. Richards, Long-term growth of superalloy γ′ particles, J. Mater. Sci. 17 (1982) 2141-2153.

[123] S.J. Pennycook, D.E. Jesson, High-resolution Z-contrast imaging of crystals, Ultramicroscopy 37 (1991) 14-38.

[124] M. Hillert, On the theory of normal and abnormal grain growth, Acta Metall. 13 (1965)

227-238.

[125] C.K.L. Davies, P. Nash, R.N. Stevens, The effect of volume fraction of precipitate on Ostwald ripening, Acta Metall. 28 (1980) 179-189.

[126] C.S. Jayanth, P. Nash, Experimental evaluation of particle coarsening theories, Mater. Sci. Tech. 6 (1990) 405-414.

[127] V.A. Phillips, A metallographic study of precipitation in a Ni-12.7at.% Al alloy, Acta Metall. 14 (1966) 1533-1547.

[128] C.G. Garay-Reyes, F. Hernández-Santiago, N. Cayetano-Castro, V.M. Lopez-Hirata, J. García-Rocha, J.L. Hernández-Rivera, H.J. Dorantes-Rosales, J.J. Cruz-Rivera, Study of phase decomposition and coarsening of γ′ precipitates in Ni-12at.% Ti alloy, Mater. Char. 83 (2013) 35-42.

[129] M.C. Chaturvedi, Y.F. Han, Strengthening mechanisms in Inconel 718 superalloy, Met. Sci. 17 (1983) 145-149.

[130] M.E. Thompson, C.S. Su, P.W. Voorhees, The equilibrium shape of a misfitting precipitate, Acta Metall. Mater. 42 (1994) 2107-2122.

[131] M. Doi, T. Miyazaki, T. Wakatsuki, The effect of elastic interaction energy on the morphology of γ′ precipitates in nickel-based alloys, Mater. Sci. Eng. 67 (1984) 247-253.

[132] H. Pottebohm, G. Neite, E. Nembach, Elastic properties (the stiffness constants, the shear modulus and the dislocation line energy and tension) of Ni-Al solid solutions and of the Nimonic alloy PE16, Mater. Sci. Eng. 60 (1983) 189-194.

[133] C.K. Sudbrack, T.D. Ziebell, R.D. Noebe, D.N. Seidman, Effects of a tungsten addition on the morphological evolution, spatial correlations and temporal evolution of a model Ni-Al-Cr superalloy, Acta Mater. 56 (2008) 448-463.

[134] Z. Mao, C. Booth-Morrison, E. Plotnikov, D.N. Seidman, Effects of temperature and ferromagnetism on the γ-Ni/γ′-Ni3Al interfacial free energy from first principles calculations, J. Mater. Sci. 47 (2012) 7653-7659.

[135] T. Philippe, P.W. Voorhees, Ostwald ripening in multicomponent alloys, Acta Mater. 61 (2013) 4237-4244.

[136] C.J. Kuehmann, P.W. Voorhees, Ostwald ripening in ternary alloys, Metall. Mater. Trans. A 27 (1996) 937-943.

[137] C. Booth-Morrison, J. Weninger, C.K. Sudbrack, Z. Mao, R.D. Noebe, D.N. Seidman, Effects of solute concentrations on kinetic pathways in Ni-Al-Cr alloys, Acta Mater. 56 (2008) 3422-3438.

[138] R.A. Karnesky, D.C. Dunand, D.N. Seidman, Evolution of nanoscale precipitates in Al microalloyed with Sc and Er, Acta Mater. 57 (2009) 4022-4031.

[139] M.E. van Dalen, T. Gyger, D.C. Dunand, D.N. Seidman, Effects of Yb and Zr microalloying additions on the microstructure and mechanical properties of dilute Al-Sc alloys, Acta Mater. 59 (2011) 7615-7626.

[140] P.W. Voorhees, The theory of Ostwald ripening, J. Stat. Phys. 38 (1985) 231-252.

[141] V.A. Snyder, J. Alkemper, P.W. Voorhees, Transient Ostwald ripening and the disagreement between steady-state coarsening theory and experiment, Acta Mater. 49 (2001) 699-709.

[142] M.K. Chen, P.W. Voorhees, The dynamics of transient Ostwald ripening, Modell. Simul. Mater. Sci. Eng. 1 (1993) 591.

[143] Z. Sun, G. Song, J. Ilavsky, G. Ghosh, P.K. Liaw, Nano-sized precipitate stability and its controlling factors in a NiAl-strengthened ferritic alloy, Sci. Rep. 5 (2015) 16081.

[144] J. Dąbrowa, W. Kucza, G. Cieślak, T. Kulik, M. Danielewski, J.W. Yeh, Interdiffusion in the FCC-structured Al-Co-Cr-Fe-Ni high entropy alloys: experimental studies and numerical simulations, J. Alloys Compd. 674 (2016) 455-462.

[145] S.B. Jung, T. Yamane, Y. Minamino, K. Hirao, H. Araki, S. Saji, Interdiffusion and its size effect in nickel solid solutions of Ni-Co, Ni-Cr and Ni-Ti systems, J. Mater. Sci. Lett. 11 (1992) 1333-1337.

[146] R.A. Swalin, A. Martin, Solute diffusion in nickel-base substitutional solid solutions, Trans. AIME 206 (1956) 567-572.

[147] R.A. Stevens, P.E.J. Flewitt, The effects of γ′ precipitate coarsening during isothermal aging and creep of the nickel-base superalloy IN-738, Mater. Sci. Eng. 37 (1979) 237-247.

[148] A.M. Ges, O. Fornaro, H.A. Palacio, Coarsening behaviour of a Ni-base superalloy under different heat treatment conditions, Mater. Sci. Eng. A 458 (2007) 96-100.

[149] J. Lapin, M. Gebura, T. Pelachová, M. Nazmy, Coarsening kinetics of cuboidal γ' precipitates in single crystal nickel base superalloy CMSX-4, Kovove Mater. 46 (2008) 313-322.

[150] E.H. Van Der Molen, J.M. Oblak, O.H. Kriege, Control of γ′ particle size and volume fraction in the high temperature superalloy Udimet 700, Metall. Mater. Trans. B 2 (1971) 1627-1633.

[151] K.B.S. Rao, V. Seetharaman, S.L. Mannan, P. Rodriguez, Effect of long-term exposure at elevated temperatures on the structure and properties of a nimonic PE 16 superalloy, Mater. Sci. Eng. 58 (1983) 93-106.

[152] B. Reppich, W. Kühlein, G. Meyer, D. Puppel, M. Schulz, G. Schumann, Duplex γ′ particle hardening of the superalloy Nimonic PE 16, Mater. Sci. Eng. 83 (1986) 45-63.

[153] A.B. Kamara, A.J. Ardell, C.N.J. Wagner, Lattice misfits in four binary Ni-Base γ/γ′ alloys at ambient and elevated temperatures, Metall. Mater. Trans. A 27 (1996) 2888-2896.

[154] W. Huther, B. Reppich, Interaction of dislocations with coherent, stree-free ordered particles, Z. Metallkd. 69 (1978) 628-634.

[155] C.A. Schuh, T.G. Nieh, A survey of instrumented indentation studies on metallic glasses, J. Mater. Res. 19 (2004) 46-57.

[156] J.I. Jang, B.G. Yoo, Y.J. Kim, J.H. Oh, I.C. Choi, H.B. Bei, Indentation size effect in bulk metallic glass, Scr. Mater. 64 (2011) 753-756.

[157] W.L. Johnson, K. Samwer, A universal criterion for plastic yielding of metallic glasses with a $(T/Tg)^{2/3}$ temperature dependence, Phys. Rev. Lett. 95 (2005) 195501.

[158] J. Lu, G. Ravichandran, W.L. Johnson, Deformation behavior of the $Zr_{41.2}Ti_{13.8}Cu_{12.5}Ni_{10}Be_{22.5}$ bulk metallic glass over a wide range of strain-rates and temperatures, Acta Mater. 51 (2003) 3429-3443.

[159] M. Lee, J. Das, K. Lee, U. Kühn, J. Eckert, Effect of prestraining on the deformation and fracture behavior of $Zr_{44}Ti_{11}Cu_{9.8}Ni_{10.2}Be_{25}$, Intermetallics 18 (2010) 1902-1907.

[160] K.S. Lee, H.J. Jun, D.W. Kim, J. Eckert, Y.W. Chang, Structural relaxation and crystallization of a $Zr_{44}Ti_{11}Cu_{9.8}Ni_{10.2}Be_{25}$ bulk metallic glass, Mater. Trans. 48 (2007) 1722-1728.

[161] W.H. Wang, Correlations between elastic moduli and properties in bulk metallic glasses, J. Appl. Phys. 99 (2006) 093506.

[162] M.Q. Tang, H.F. Zhang, Z.W. Zhu, H.M. Fu, A.M. Wang, H. Li, Z.Q. Hu, TiZr-base bulk metallic glass with over 50 mm in diameter, J. Mater. Sci. Technol. 26 (2010) 481-486.

[163] X.J. Gu, S.J. Poon, G.J. Shiflet, J.J. Lewandowski, Compressive plasticity and toughness of a Ti-based bulk metallic glass, Acta Mater. 58 (2010) 1708-1720.

[164] J. Fornell, A. Concustell, S. Suriñach, W. Li, N. Cuadrado, A. Gebert, M. Baró, J. Sort, Yielding and intrinsic plasticity of Ti-Zr-Ni-Cu-Be bulk metallic glass, Int. J. Plast. 25 (2009) 1540-1559.

[165] J. Mei, Titanium-Based Bulk Metallic Glasses: Glass Forming Ability and Mechanical Behavior, PhD diss., Joseph Fourier University, Grenoble, France, 2009.

[166] J.M. Park, G. Wang, S. Pauly, N. Mattern, D.H. Kim, J. Eckert, Ductile Ti-based bulk

metallic glasses with high specific strength, Metall. Mater. Trans. A 42 (2011) 1456-1462.

[167] D. Lahiri, J. Karp, A.K. Keshri, C. Zhang, G.S. Dulikravich, L.J. Kecskes, A. Agarwal, Scratch induced deformation behavior of hafnium based bulk metallic glass at multiple load scales, J. Non-Cryst. Solids 410 (2015) 118-126.

[168] C.A. Schuh, T.G. Nieh, A nanoindentation study of serrated flow in bulk metallic glasses, Acta Mater. 51 (2003) 87-99.

[169] J. Archard, Contact and rubbing of flat surfaces, J. Appl. Phys. 24 (1953) 981-988.

[170] L.J. Zhang, Z.K. Jiang, M.D. Zhang, J.T. Fan, D.J. Liu, P.F. Yu, G. Li, R.P. Liu, Effect of solid carburization on the surface microstructure and mechanical properties of the equiatomic CoCrFeNi high-entropy alloy, J. Alloys Compd. 769 (2018) 27-36.

[171] Y. Huang, Y.L. Chiu, J. Shen, Y. Sun, J.J. Chen, Mechanical performance of metallic glasses during nanoscratch tests, Intermetallics 18 (2010) 1056-1061.

[172] D. Pan, A. Inoue, T. Sakurai, M. Chen, Experimental characterization of shear transformation zones for plastic flow of bulk metallic glasses, PNAS 105 (2008) 14769-14772.

[173] J.F. Archard, The temperature of rubbing surfaces, Wear 2 (1959) 438-455.

[174] H. Hertz, On the contact of elastic solids, Z. Reine Angew. Math. 92 (1881) 156-171.

[175] J. Goddard, H. Wilman, A theory of friction and wear during the abrasion of metals, Wear 5 (1962) 114-135.

[176] S. Lafaye, M. Troyon, On the friction behaviour in nanoscratch testing, Wear 261 (2006) 905-913.

[177] S. Lafaye, C. Gauthier, R. Schirrer, The ploughing friction: analytical model with elastic recovery for a conical tip with a blunted spherical extremity, Tribol. Lett. 21 (2006) 95-99.

[178] M. Mishra, I. Szlufarska, Analytical model for plowing friction at nanoscale, Tribol. Lett. 45 (2012) 417-426.

[179] A.A. Griffith, The phenomena of rupture and flow in solids, Philos. Trans. R. Soc. London Ser. A 221 (1920) 163-198.

[180] G.R. Irwin, Analysis of stresses and strains near the end of a crack traversing a plate, J. Appl. Mech. 24 (1957) 361-364.

[181] L. Goodman, G. Hamilton, The stress field created by a circular sliding contact, J. Appl. Mech. 33 (1966) 371-376.

[182] J.P. Benthem, W.T. Koiter, Asymptotic approximations to crack problems, in: G.C. Sih (Ed.), Methods of Analysis and Solutions of Crack Problems, Springer, 1973, pp. 131-178.

[183] B. Gludovatz, A. Hohenwarter, D. Catoor, E.H. Chang, E.P. George, R.O. Ritchie, A fracture-resistant high-entropy alloy for cryogenic applications, Science 345 (2014) 1153-1158.

[184] B. Gludovatz, A. Hohenwarter, K.V. Thurston, H. Bei, Z. Wu, E.P. George, R.O. Ritchie, Exceptional damage-tolerance of a medium-entropy alloy CrCoNi at cryogenic temperatures, Nat. Commun. 7 (2016) 10602.

[185] J.J. Lewandowski, W.H. Wang, A.L. Greer, Intrinsic plasticity or brittleness of metallic glasses, Philos. Mag. Lett. 85 (2005) 77-87.

[186] J.J. Lewandowski, M. Shazly, A.S. Nouri, Intrinsic and extrinsic toughening of metallic glasses, Scr. Mater. 54 (2006) 337-341.

[187] P.S. Phani, W.C. Oliver, A direct comparison of high temperature nanoindentation creep and uniaxial creep measurements for commercial purity aluminum, Acta Mater. 111 (2016) 31-38.

[188] M.T. Tsai, J.C. Huang, P.H. Lin, T.Y. Liu, Y.C. Liao, J.S. Jang, S.X. Song, T.G. Nieh, Creep of face-centered-cubic {111} and {100} grains in FeCoNiCrMn and FeCoNiCrMnAl alloys: Orientation and solid solution effects, Intermetallics 103 (2018) 88-96.

Vita

Yangyang Zhao was born in a small village in Anhui, China. He attended the Department of Materials Science and Engineering at Huazhong University of Science and Technology in 2007 and received his bachelor's degree in 2011. After that, he was enrolled in the master program at Shanghai Jiao Tong University, where he got the master's degree in 2015. In the same year, he came to the University of Tennessee, and started his doctorate in Materials Science and Engineering under the guidance of Dr. T. G. Nieh.